

https://dspace.org/

# Application of reflection seismics to the assessment of cool-mining-related subsidence in the Karoo Basin and neotectonic activity in the offshore orange basin

**Isiaka, Ibrahim Ahmed**

**2018**

https://hdl.handle.net/10539/27137

Isiaka, Ahmed Ibrahim, (2018) Application of reflection seismics to the assessment of coal-mining-related subsidence in the Karoo Basin and neotectonic activity in the offshore Orange Basin, University of the Witwatersrand, Johannesburgm, https://hdl.handle.net/10539/27137.

Downloaded from a DSpace repository. https://dspace.org/

# APPLICATION OF REFLECTION SEISMICS TO THE ASSESSMENT OF COAL-MINING-RELATED SUBSIDENCE IN THE KAROO BASIN AND NEOTECTONIC ACTIVITY IN THE OFFSHORE ORANGE BASIN

Isiaka Ibrahim Ahmed

A thesis submitted to the Faculty of Science, University of the Witwatersrand, in partial fulfillment of the requirements for the degree of Doctor of Philosophy in Geophysics.

Johannesburg, 2018

# Declaration

I declare that this thesis is my own, unaided work. It is being submitted for the Degree of Doctor of Philosophy in the University of the Witwatersrand, Johannesburg, South Africa. It has not been submitted before for any degree or examination in any other University.

_____

Isiaka Ibrahim Ahmed

_____ day of _____ 2018.

# Abstract

The general aim of this thesis was to use the high-resolution seismic reflection method to investigate coal-mining related subsidence in the Karoo Basin and to assess hydrocarbon leakage and neotectonic activity in the offshore Orange Basin. This research work is divided into three independent parts. The first part is a shallow sub-surface investigation conducted at old coal mines located in the Benoni area and the Springlake Colliery mine, where room and pillar method was used for coal-mining. At the Benoni study area, the high-resolution seismic reflection investigation was used to detect near-surface voids related to coal-mining, as well as the dissolution cavities within the underlying dolomite that are responsible for the subsidence- and sinkholes-related features commonly observed in the area. Similarly, the technique was used to delineate subsidence zone in the Springlake mine, where subsidence is caused by the collapse of the overlying strata into subsurface voids due to the removal of coal.

In the second part of the thesis, a major half-graben bounded fault within the Ibhubesi gas field of the Orange Basin was investigated. The objective was to assess the vertical migration of hydrocarbon and the recent tectonic activities along the fault. It was found that the vertical migration of hydrocarbon along the fault occurred through fault-parallel extensional fractures within the fault zones, as well as in the relay zones within the fault segment boundaries. The results also provide evidence that the fault is tectonically active, and therefore it is recommended that a seismic hazard assessment is conducted around the vicinity of the fault.

The third part of the thesis is focused on the investigation of an enigmatic circular geological structure in the Orange Basin. Volume rendering of high-resolution 3D reflection seismic data revealed the detailed morphology of the circular structure. The morphological characteristics exhibited by the circular structure resemble a complex impact crater. However, the confirmation that this enigmatic feature is an impact structure is subject to the analysis of core samples from boreholes within the vicinity of the structure.

## Dedication

*This project is dedicated to my wife, Amina, and my children, Ibrahim, Zainab and Aisha.*

# Acknowledgements

I thank the management of Ahmadu Bello University Zaria, Nigeria, the Tertiary Education Trust Fund (TETFUND) and the Julian Baring Scholarship Fund for the funding provided for this PhD research. Without your financial assistance, this project would not have been possible.

I am most grateful to my supervisors, Professor Raymond Durrheim and Dr. Musa Manzi, for having faith in my ability to conduct a PhD research project under their supervision. Your invaluable advice, technical guidance and moral support throughout the period of this project are highly appreciated. The technical assistance received from Dr. Marco Andreoli and Professor Kim Ncube-Hein in structural geology and geodynamics is also well appreciated. I thank the Petroleum Agency of South Africa (PASA) for providing the 3D seismic data, the Council for Science and Industrial Research (CSIR) for granting access to the ReflexW seismic processing software, and IHS Kingdom and DUG INSIGHT for donating the seismic interpretation software used for the seismic analysis. I also thank Mr. Tony A. Bear of Bear Geoconsultants for providing the geotechnical data and Mr. Trevor of Ripple Creek for access to the site.

I am grateful to the head of the Department of Geology, Ahmadu Bello University Zaria Nigeria, Professor Halidu Hamza, for his fatherly support throughout the period of this project, and the entire geophysics research team of the School of Geosciences, University of the Witwatersrand for their technical and moral support.

Finally, I am grateful to all the staff and students of the School of Geosciences, University of the Witwatersrand, South Africa, for making my stay throughout the period of this project a smooth and memorable one.

# Contents

Declaration ..... ii
Abstract ..... iii
Dedication ..... v
Acknowledgements ..... vi
Contents ..... vii
List of Figures ..... x
List of Tables ..... xiii
Chapter 1 ..... 1
General Introduction ..... 1
1.1 Thesis overview ..... 1
1.2 Coal exploration and mining in the Karoo Basin of South Africa ..... 3
1.3 History of hydrocarbon exploration in South Africa ..... 6
1.4 Research motivation ..... 7
1.4.1 Coal-mining-related subsidence ..... 7
1.4.2 Hydrocarbon leakage and offshore neotectonics ..... 8
References ..... 10
Chapter 2 ..... 14
Seismic Wave ..... 14
2.1 Introduction ..... 14
2.2 Seismic wave theory ..... 15
2.2.1 Seismic wave equation ..... 15
2.2.2 Types of seismic waves ..... 17
2.2.3 Seismic wave velocities ..... 20
2.2.4 Seismic energy decay ..... 23
2.2.5 Seismic resolution ..... 25
2.3 Methodology ..... 28
2.3.1 Seismic reflection method ..... 28
2.3.2 Reflection seismic application to near-surface investigation ..... 31
2.3.3 Sources of noise in near-surface reflection seismic data ..... 33
2.3.4 Seismic attributes ..... 34
References ..... 35
Chapter 3 ..... 39

High-resolution Seismic Reflection Investigation of Subsidence and Sinkholes at Abandoned Coal Mine Sites in South Africa ..... 39

Summary ..... 39

3.1 Introduction ..... 40
3.2 Location and geology ..... 43
3.2.1 Case study 1 (Benoni Area) ..... 43
3.2.2 Case study 2 (Springlake Colliery mine) ..... 47
3.3 Seismic data acquisition ..... 47
3.4 Seismic data processing ..... 52
3.5 Numerical modeling ..... 63
3.6 Results and interpretation ..... 64
3.7 Conclusions and recommendations ..... 74

References ..... 76

Chapter 4 ..... 80

3D Seismic Analysis of the AK Fault, Orange Basin, South Africa: Implications for Hydrocarbon Leakage and Offshore Neotectonics ..... 80

Summary ..... 80

4.1 Introduction ..... 81
4.2 Tectonic setting and petroleum system of the Orange Basin ..... 83
4.3 Data and methods ..... 88
4.3.1 3D seismic reflection data acquisition ..... 88
4.3.2 3D seismic reflection data processing ..... 88
4.3.3 3D seismic data resolution ..... 92
4.4 Methodology ..... 92
4.5 Results and discussion ..... 93
4.5.1 AK Fault geometry ..... 93
4.5.2 Geometry of the relay zones ..... 98
4.5.3 The segmented origin of the AK Fault ..... 100
4.5.4 Implications for hydrocarbon leakage assessment ..... 104
4.5.6 Implications for offshore neotectonics ..... 112
4.6 Conclusions ..... 114

References ..... 115

Chapter 5 ..... 126

Volume Rendering of 3D Seismic Reflection Data Reveals a Possible Impact Structure in the Orange Basin, Offshore South Africa. ..... 126

Summary ..... 126

5.1 Introduction ..... 127

5.2 Geological setting of the Orange Basin ..... 128
5.3 3D Seismic data and methodology ..... 129
5.3.1 Seismic data acquisition and processing ..... 129
5.3.2 Methodology ..... 131
5.4 Results and discussion ..... 132
5.5 Conclusions ..... 138

References ..... 139

Chapter 6 ..... 143

General Conclusions and Recommendations ..... 143

6.1 High-resolution Seismic Reflection Investigation of Subsidence and Sinkholes at Abandoned Coal Mine Sites in South Africa (Chapter 3) ..... 143
6.1.1 Summary ..... 143
6.1.2 Recommendations for future investigations ..... 144
6.2 3D Seismic Analysis of the AK Fault, Orange Basin: Implications for Hydrocarbon Leakage Assessment and Offshore Neotectonics (Chapter 4) ..... 145
6.2.1 Summary ..... 145
6.2.2 Recommendations for future investigations ..... 146
6.3 Volume Rendering of 3D Seismic Reflection Data Reveals a Possible Impact Structure in the Orange Basin, Offshore South Africa (Chapter 5) ..... 146
6.3.1 Summary ..... 146
6.3.2 Recommendations for future investigations ..... 147

Reference ..... 148

APPENDIX ..... 149

# List of Figures

Figure 1.1: The geological map of Karoo Basin. ..... 4

Figure 2.1: Elastic deformations and ground particle motions ..... 19

Figure 2.2: Elastic deformations and ground particle motions ..... 19

Figure 2.3: Energy losses due to spherical divergence ..... 24

Figure 2.4: An illustration of the principle of reflection seismic method. ..... 29

Figure 2.5: Reflected and transmitted rays ..... 30

Figure 3.1: Location and regional geological map of Benoni. ..... 44

Figure 3.2: Surface evidence of recent subsidence-related events at Benoni area. ..... 45

Figure 3.3: (a) Satellite image of Benoni study area showing the location of the boreholes and the seismic lines acquired in the area. (b) The stratigraphical correlation of the geology encountered in the boreholes. ..... 48

Figure 3.4: (a) Underground mine plan of the Springlake mine showing the seismic profile acquired across the suspected mined-out zone. (b) Boreholes from the Springlake mine showing the subsurface stratigraphy. ..... 49

Figure 3.5: A seismic line acquired adjacent to the abandoned leaning structure. ..... 51

Figure 3.6: Trace editing. ..... 54

Figure 3.7: Frequency spectrum of the whole dataset ..... 55

Figure 3.8: Selected traces and the corresponding amplitude spectra ..... 56

Figure 3.9: Pre-stack shot gathers. ..... 57

Figure 3.10: Pre-stack shot gathers before (a) and after surgical muting (b). ..... 58

Figure 3.11: Illustration of the CVS analysis. ..... 61

Figure 3.12: An example of a filtered stacked section ..... 63

Figure 3.12: The depth sections with corresponding 2D synthetic seismograms. ..... 66

Figure 3.13: Pre-stack and the corresponding stacked sections ..... 67

Figure 3.14: TWT migrated section ..... 68

Figure 3.15: (a) Pre-stack shot gathers along LN2 showing visible reflection events after applying a bandpass Butterworth filter. Trace normalized gain is applied for display, (b) Stack and the corresponding time migrated section along LN2 with AGC applied, and (C) Time migrated (with AGC applied) and the corresponding depth section along LN2. The arrow indicates the top of the dolerite layer ..... 69

Figure 3.16: (a) Pre-stack shot gathers along LN3 with visible reflections after applying a bandpass Butterworth filter, with trace normalized gain applied for display (b) Stacked and the corresponding migrated section obtained along LN3. Note the alternating chaotic reflection zones (circled region) in the stacked section and the enhanced resolution in the migrated section, (c) Interpreted time and depth migrated section.. ..... 71

Figure 3.17**:** (a) Pre-stack shot gathers along the Springlake profile showing visible reflection events after applying a bandpass Butterworth filter, and (b) Stacked and migrated section (with AGC applied). ..... 73

Figure 3.18: (a) The interpreted time migrated and depth section along the Springlake profile showing a disruptive zone probably due to collapsed pillar or void (circled region) (b) The 2D pseudosection from the ERT survey showing voids that probably extend to greater depth.. ..... 74

Figure 4.1: (a) Isopach map of the post-rift sedimentary succession in the offshore Orange Basin (modified from Jungslager, 1999). The outline of the AK Fault in the study area is shown along with the other two faults, "V" and "D" previously investigated by Viola et al., (2005) and De Beer (2012) respectively. The overlaid seismological data downloaded from the International Seismological Centre (2017) covers the region around southern Namibia and the Northern Cape, and shows the evidence of seismic activity within the vicinity of the AK Fault. (b) Geological cross-section across the central Orange Basin showing the AK Fault and other half-graben bounded faults ..... 84

Figure 4.2: Seismic section across the northern segment of the AK Fault. ..... 94

Figure 4.3: Geometry of the AK Fault in semblance slice ..... 95

Figure 4.4: Interpreted perpendicular sections along the strike of the AK Fault. ..... 97

Figure 4.5: Variation in the geometry and map-view dimension ..... 99

Figure 4.6: Interpreted perpendicular and parallel section ..... 101

Figure 4.7: A detailed geometry of the fault zone ..... 102

Figure 4.8: Vertical sections investigated for possible fluid leakage features.. ..... 108

Figure 4.9: Edge attributes analysis ..... 109

Figure 4.10: (a) A conically-shaped mud diapir at incipient stage along the AK Fault zone, with a base that is aligned parallel to the strike of the fault. (b) Structural deformation above the mud diapir is characterized by up-doming and faulting of the overlying strata. ..... 111

Figure 4.11: A horizon below the seabed. ..... 112

Figure 5.1: Map of the offshore southern Africa ..... 130

Figure 5.2: A time-slice at 550 ms showing the buried crater in the circled region . 134
Figure 5.3: Cross-section across the crater with possible deformational features .... 135
Figure 5.4: Volume rendering at 60-80% opacity..... 136
Figure 5.5: Volume rendering at 60-80% opacity..... 137

**List of Tables**

Table 3.1: Seismic data acquisition parameters ..... 52
Table 3.2: Refraction static analysis along LN1 (100 Hz geophone) ..... 58
Table 3.3: Refraction static analysis along LN1 (48 Hz geophone) ..... 59
Table 3.4: Refraction static analysis along LN2 ..... 59
Table 3.5: Refraction static analysis along LN3 ..... 59
Table 3.6: Refraction static analysis along the Springlake profile..... 60
Table 3.7: Seismic data processing sequence ..... 62
Table 3.8: Model parameters for borehole BH003 ..... 64
Table 3.9: Model parameters for borehole BH004 ..... 64
Table 4.1: Seismic data acquisition parameters ..... 90
Table 4.2: Processing sequence for the seismic data ..... 91

# Chapter 1

# General Introduction

## 1.1 Thesis overview

This thesis describes the research conducted using the high-resolution reflection seismic method to investigate near-surface subsidence at two old coal mines within the Karoo Basin, and to assess the hydrocarbon leakage and neotectonic activity in the offshore Orange Basin. The research was achieved through three independent investigation and comprises six chapters, including this introductory chapter (Chapter 1) that describes the thesis contents. The chapter also contains brief description of the research motivation, a short introduction to coal mining in Karoo Basin, the history of hydrocarbon exploration in South Africa, as well as a review of hydrocarbon leakage and neotectonic activities along the south-west coast of South Africa.

Chapter 2 contains background theory and methodology, including the derivation of the seismic wave equations relevant to this research. The chapter also discusses the fundamental principles of the reflection seismic method, the application to near-surface investigation, and calculation and application of seismic attributes.

Chapters 3, 4, and 5 represent separate, independent papers that have been submitted to different peer-review journals. Each of these chapters begins with an introduction to the problem and the objectives of the investigation, and is subsequently followed by the geological setting, methodology, description of the seismic data source, the interpretation and discussion of the data processing,

results, conclusions, and references. In order to avoid repetition, for example, where the same seismic data source and geological setting were involved, as in Chapter 4 and 5, a full description of the data and the geology is provided in Chapter 4 and only summarized in Chapter 5.

Chapter 3 is a paper describing the near-surface high-resolution reflection seismic investigation conducted at Benoni area and the Springlake Colliery mine, with the objective of assessing the coal-mining-related subsidence and sinkhole features in the two study areas. This work was presented at the 2nd Biennial SEG International Conference on Engineering Geophysics in Al-Ain, U.A.E., in November 2015. The paper is currently under review in the Journal of Environmental and Engineering Geophysics with a manuscript number 16-035R1.

In chapter 4, a long-lived, half-graben bounded fault located within the exploration Block 2A of the Orange Basin was investigated using the high-resolution 3D reflection seismic data. A detailed description of the fault was achieved through the combination of conventional seismic interpretation and seismic attributes analysis. The vertical migration of fluids along the fault and the recent tectonic activities around it were also investigated. Part of this chapter has been published in the international journal Tectonophysics (Isiaka et al., 2017).

Chapter 5 contains the investigation of an enigmatic circular geological structure in the Orange Basin using the high-resolution 3D reflection seismic data. The work includes the detailed description of the circular structure using the 3D volume-rendering technique. The technique is able to reveal the detailed morphological features of this circular structure that suggests a possible impact

structure. This work was presented at the 14th Biennial SAGA International Conference and Exhibition in Drakensberg, South Africa, in July 2015, and the 35th International Geological Congress (IGC) in Cape Town, South Africa, in August 2016. The work is currently under review in the Journal of African Earth Science with paper number AES4985.

Chapter 6 completes the thesis with summary of the findings from the research work, as well as conclusions and recommendations for future investigation.

## 1.2 Coal exploration and mining in the Karoo Basin of South Africa

The Karoo Basin of South Africa is a unique foreland basin in Africa, being the only basin in Africa that contains complete sedimentary records from the Late Carboniferous to Jurassic period (Allen et al., 1986; Cadle et al., 1993). The basin has an areal extent of ~ 600,000 sq. km (Fig. 1.1), and contains ~ 5500 m thickness of deep marine to fluvial Karoo Supergroup deposits (e.g., Fildani et al., 2009; Flint et al., 2011). The sedimentary deposits within the basin vary in thickness from the north to the south of the basin, with the greatest sedimentary thickness occurring in the southern margin of the basin (Cadle et al., 1993). The sedimentary succession consists of the Late Carboniferous Dwyka Group, which is made up of diamictites, varves and glacio-fluvial deposits (Flint et al., 2011). Overlying the Dwyka Group is the predominantly siliciclastic sediments of the Ecca Group, which is divided into the Pietermaritzburg Formation, Vryheid Formation and the Volksrust Formation. The Ecca Group is succeeded by the fluvial, lacustrine Beaufort Group and the volcanic Stormberg Group (Fig. 1.1).

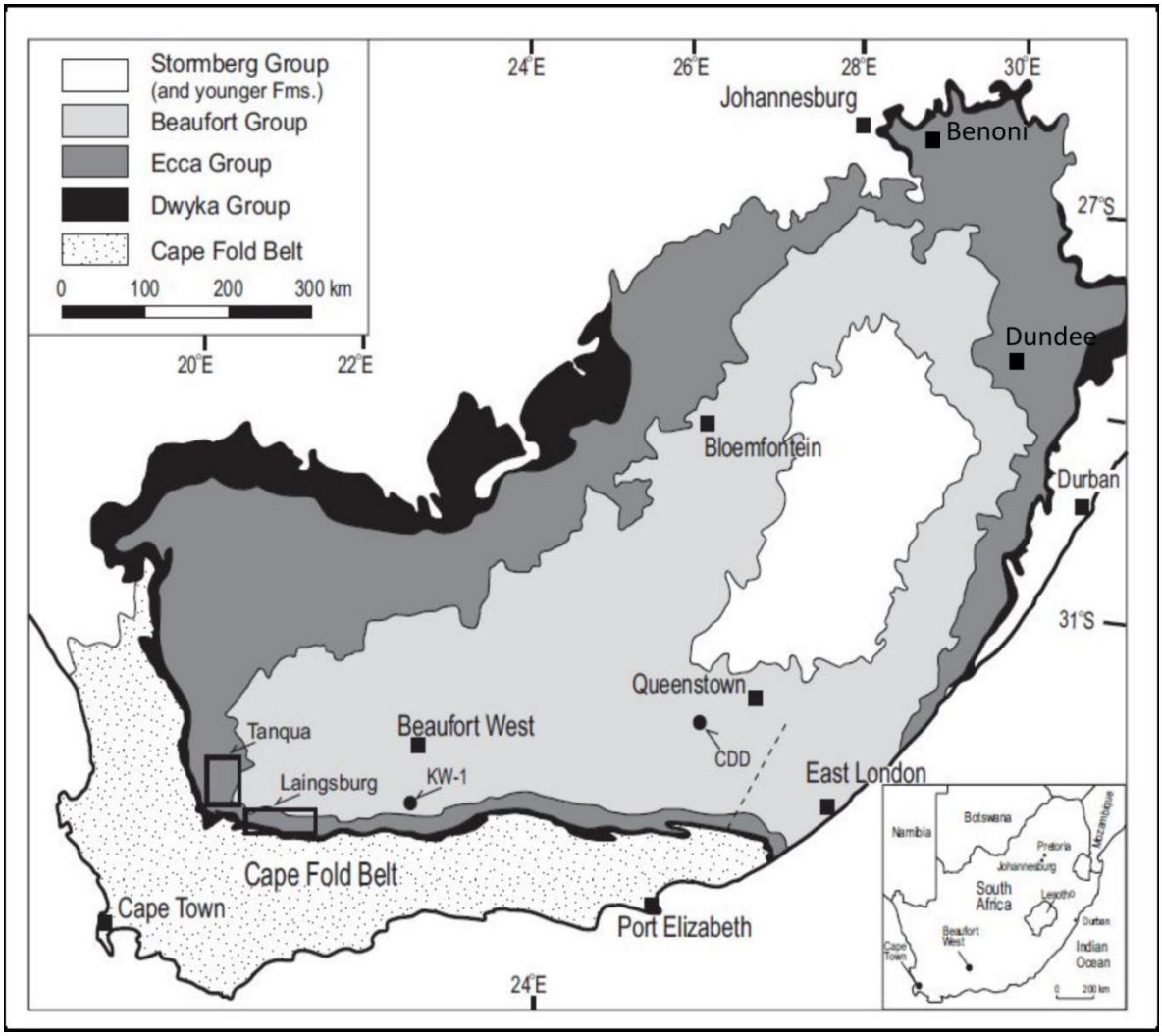



Figure 1.1: The geological map of Karoo Basin showing the different stratigraphic groups (modified from Catuneanu et al., 2005 and Fildani et al., 2009).

The occurrence of coal in South Africa was documented between 1838 and 1859 in the Kwazulu-Natal, Mpumalanga, and Eastern Cape Provinces (Jeffrey et al., 2015). However, the first commercial mining of coal did not take place until 1870 in the Eastern Cape (Jeffrey et al., 2015). The economically exploitable coal seams usually occur within the alternating conglomeratic sandstones and shales of the Vryheid Formation of the Ecca Group (Cadle et al., 1993). Coal is South Africa's most available and cheapest source of energy, providing about 70% of

South Africa's primary energy. In 2016 coal was the commodity with the largest sales, and the largest earner of foreign exchange (Chamber of Mines of South Africa, 2016).

The extraction of coal in South Africa is carried out using three different methods. These methods include the bord and pillar method, longwall method, and the open-cast mining method. The bord and pillar mining method is also referred to as the room and pillar method, where some of the coal is removed and some left in place as pillars to support the overlying rocks. This method allows a considerable amount of coal to be left in the ground for subsequent partial extractions towards the end of mining (Jeffrey et al., 2015). However, the roof rocks may collapse into the mined-out zone if insufficient pillar support is left at the end of mining. The longwall mining method involves the removal of the entire coal seam from the ground, while the roof is allowed to collapse into the mined-out void. This often results into subsidence of the surface due to collapse of the overlying rocks in shallow underground mines (Jeffrey et al., 2015).

The open-cast mining method is becoming more popular nowadays in South Africa, due to technology that allows coal at greater depth to be extracted economically (Jeffrey et al., 2015). Many abandoned underground mines that still have significant reserves are being re-mined using open-cast methods (Jeffrey et al., 2015). In the open-cast method, the top soil cover is removed and stockpiled, while the overburden rock is blasted and removed to expose the underlying coal seam. The advantage of the open-cast method is that land restoration is possible after the end of mining, which is achieved by returning the blasted overburden broken rocks and the stockpiled top soil to fill the mine pits. This is then followed

by landscaping and the replanting of the original vegetation type (Jeffrey at al., 2015).

## 1.3 History of hydrocarbon exploration in South Africa

Hydrocarbon exploration was first conducted in South Africa in 1940s by the Geological survey of South Africa in the onshore basins. The search was intensified in 1965 following the formation of the Soekor (Pty) Ltd in the onshore region of the Karoo, Algoa and the Zululand Basins (PASA, 2017). Two years later, hydrocarbon exploration had extended into the offshore region with the granting of concessions to some international oil companies, including Total, Gulf Oil, Superior, Esso and Shell, The exploration in the offshore led to the first hydrocarbon discovery (in the form of gas and condensate) by Superior Oil in the offshore Pletmos Basin in 1969. Meanwhile, from the mid-1970s to the late 1980s, the exploration for oil in the offshore suffered a great setback following the withdrawal of the international companies due to political sanctions against South Africa. The South African owned state oil and gas exploration company, Soekor (Pty), was, during this period, the only company operating in the offshore areas until 1994 when the offshore exploration was reopened to international investors. Since the resumption of oil exploration in the offshore in 1994, 300 exploration wells, including appraisal and production wells, have been drilled, while 233,000 km of 2D seismic data and 10,200 sq. km of 3D seismic data have been acquired (PASA, 2017). Several small oil and gas fields have also been discovered in the offshore areas since the resumption of the oil exploration, with the majority of the discoveries located within the Bredasdorp Basin.

In the Orange Basin, one oil and several gas and condensate discoveries have been made, leading to the Ibhubesi gas field, which is currently undergoing appraisal and development. The Orange Basin contains several petroleum systems that are sourced from active source rocks. These include the Aptian source rocks (van der Spuy, 2003) and the Cenomanian-Turonian source rocks (Aldrich et al., 2003). However, the most documented petroleum system in the Orange Basin is the discovery of the natural gas system, which is sourced from the lower Aptian and Barremian shaly source rocks located in the depocentre of the Orange Basin. Several indicators of active source rocks at depth, such as seismic gas chimneys, seafloor gas escape features, gas hydrate and discrete bright spots are common in the Orange Basin (PASA, 2017).

## 1.4 Research motivation

### 1.4.1 Coal-mining-related subsidence

Subsidence is an event that is associated with the gradual or sudden collapse of the ground surface into underground voids or cavities. It is a common hazard in many abandoned old coal mines, where the presence of near-surface cavities poses a safety hazard. In old workings, where the room and pillar method of coal extraction was employed, the deterioration of the pillars supporting the roof over time can result to the failure of the pillars, which may give rise to subsidence above the old workings (van Schoor and Fourie, 2014). Subsidence may have a significant impact on surface structures such as buildings, bridges, and roads, causing damage through instability, failure, and the eventual collapse of structures that may also result to the loss of life and property. Water-filled subsidence can

result in isolated ponds that may pose a great risk to human and animal lives, while severe economic damages can be a direct consequence of subsidence, especially in urban areas (Intrieri et al., 2015). Therefore, it is important to identify and delineate areas prone to subsidence prior to construction to avoid any economic or loss of human life.

### 1.4.2 Hydrocarbon leakage and offshore neotectonics

Hydrocarbon leakage through vertical migration to the surface may serve as a direct indicator of an active (yielding hydrocarbon) or previously active (depleted) source rock at depth, and, in some instances, may lead to the discovery of oil fields. Evidence of hydrocarbon leakage features such as gas chimneys, pockmarks and mud volcanoes are important exploration tools for evaluating shallow and deep hydrocarbon prospects (Berge, 2013), and can provide insights into understanding the hydrocarbon migration path. Besides its use as an exploration technique, natural hydrocarbon leakage also has a profound effect on the environment, causing environmental pollution and the depletion of the ozone layer through the natural methane that is released into the atmosphere. A significant relationship also exists between hydrocarbon leakage and fault reactivation. Fault reactivation can lead to the leakage of hydrocarbons, which may result into the depletion of the reservoir (e.g. Jones et al., 2000), while fluid movement along reactivated faults has also been linked to the origin of earthquake swarms with magnitude up to $M_L$ 5 (e.g. Zoback and Zinke, 2002).

The study of Cenozoic reactivation of older faults in southern Africa was motivated by the need to understand the present-day tectonic stress regime

affecting the region. South Africa is located on a continental passive margin, where seismic activities are usually rare. However, the region in recent times has witnessed several earthquake activities (e.g., Hartnady, 2002; Viola et al., 2005), with some of these events causing serious damage. A famous example is the $M_L$ 6.3 earthquake that rocked the town of Tulbagh in Western Cape, South Africa in 1969 (e.g. Andreoli et al., 1996). Besides the occurrence of earthquakes, the need for the geological storage of nuclear wastes also prompted the study of older faults and fractures that are liable to be reactivated. The neotectonic events in southern Africa have been largely attributed to two major stress fields, which include an extensional NNE trend that corresponds to the East Africa Rift System, and the NW-WNW compressive Wegener Stress Anomaly (e.g., Andreoli et al., 1996; Viola et al., 2005). According to Bird et al. (2006), the latter is caused by the NE-SW extensional stress resulting from the resistance of the unbroken lithosphere to the relative rotation of the incipient Somalia plate away from the Africa plate.

Evidence of neotectonic activity has been reported in most part of southern Africa, both in the onshore and the offshore environments (Andreoli et al., 1996; Viola et al, 2005, 2012; Bird et al., 2006; White et al., 2009; De Beer, 2012; Madi, 2016). However, critical to this study is the evidence of Paleocene to Holocene fault reactivation that was reported along the southwest Atlantic coast of South Africa. The alignment of mud-volcanoes due to active faulting was first reported in the offshore Orange Basin by Ben-Avraham et al. (2002). Viola et al. (2005) later compared this phenomenon in a broad tectonic setting to onshore faulting, and proposed that the mud-volcanoes were caused by the reactivation of an older

normal fault in a strike-slip regime. A recent study by De Beer (2012) also identified Neogene to Quaternary faulting along the Namaqualand coast, which was caused by extensional normal faulting, while the Pleistocene to Holocene reactivation of the Hebron fault along the coast of Namibia has also been proposed to be dominantly due to normal faulting caused by extension as a result of gravitational instability along the coast (White et al., 2009).

## References


Aldrich, J., Zilinski, R., Edman, J., Leu, W., Berge, T. and Corbett, K., 2003. Documentation of a new petroleum system in the South Atlantic, *American Association of Petroleum Geologists,* Annual Convention.

Allen, P. A., Homewood, P., and Williams, G. D., 1986. Foreland basins: an introduction, in: Allen, P. A. and Homewood, P. (Eds.), Foreland Basins. *International Association of Sedimentology Special Publication*, **8**, 3-12.

Andreoli, M. A. G., Doucoure, M., Van Bever Donker, M., Brandt, D., and Andersen, N. J. B., 1996. Neotectonics of southern Africa- a review, *Africa Geoscience Review*, **3**, 1-16.

Ben-Avraham, Z., Smith, G., Reshef, M., and Jungslager, E., 2002. Gas hydrate and mud volcanoes on the southwest African continental margin off South Africa, *Geological Society of America*, **30**, 927-930.

Berge, T. B., 2013. Hydrocarbon seeps: recognition and meaning, in: Aminzadeh, F., Berge, T. B., and Connolly, D. L., (Eds.), Hydrocarbon seepage: from source to surface, Geophysical Developments, *Society for Exploration Geophysicists*, **16**, 1-7.

Bird, P., Ben-Avraham, Z., Schubert, G., Andreoli, M., and Viola, G., 2006. Patterns of stress and strain in southern Africa, *Journal of Geophysical Research*, **111**, B08402, doi:10.1029/2005JB003882.

Cadle, A. B., Cairncross, B., Christie, A. D. M., and Roberts, D. L., 1993. The Karoo Basin of South Africa: type basin for the coal-bearing deposits of southern Africa, *International Journal of Coal Geology*, **23**, 117-157.

Catuneanu, O., Wopfner, H., Eriksson, P. G., Cairncross, B., Rubidge, B. S., Smith, R. M. H., and Hancox, P. J., 2005. The Karoo basins of south-central Africa: *Journal of African Earth Sciences*, **43**, 211-253, doi: 10.1016/j.jafrearsci.2005.07.007.

Chamber of Mines, 2017. Facts and Figures 2016. Chambers of Mines of South Africa.

De Beer, C. H., 2012. Evidence of Neogene to Quaternary faulting and seismogenic deformation along the Namaqualand coast, South Africa, *South African Journal of Geology*, **115**, 117-136.

Fildani, A., Weislogel, A., Drinkwater, N. J., McHargue, T., Tankard, A., Wooden, J., Hodgson, D., and Flint, S., 2009. U-Pb zircon ages from the southwestern Karoo Basin, South Africa- implications for the Permian-Triassic boundary, *Geological Society of America*, **37**, 719-722.

Flint, S. S., Hodgson, D. M., Sprague, A. R., Brunt, R. L., Van der Merwe, W. C., Figueiredo, J., Prelat, A., Box, D., Di Celma, C., and Kavanagh, J. P., 2011. Deposition architecture and sequence stratigraphy of the Karoo basin floor to shelf edge succession, Laingsburg depocentre, South Africa, *Marine and Petroleum Geology*, **28**, 658-674.

Hartnady, C. J. H., 2002. Earthquake hazard in Africa: Perspectives on the Nubia-Somalia boundary, *South Africa Journal of Science*, **98**, 425-428.

Intrieri E., Giovanni, G., Nocentini, M., Lombardi, L., Francesco, M., Fidolini, F., and Casagli, N., 2015. Sinkhole monitoring and early warning: An experimental

and successful GB-InSAR application, *Geomorphology*, **241**, 304-314. doi.org/10.1016/j.geomorph.2015.04.018

Jeffrey, L., Henry, G., and McGill, J., 2015. Introduction to South African coal mining and exploration, in: Van Schoor, M. and Fourie C. J. S. (Eds.), A guide for applying geophysics to coal mining problems in South Africa, *COALTECH*, 4-21.

Jones, R. M., Boult, P., Hillis, R. R., Mildren, S. D., and Kaldi, J., 2000. Integrated hydrocarbon seal evaluation in the Penola Trough, Otway Basin: *Australian Petroleum Production and Exploration Association Journal*, **40**, 194-211.

Madi, K., 2016. Seismicity and neotectonic uplift in the Augrabies Falls National Park, Namaqualand, Northern Cape, South Africa, *Earthquake Science*, **29**, 281-289, doi10.1007/s11589-016-0166-z.

PASA, 2017. Petroleum Exploration in South Africa.

Van der Spuy, D., 2003. Aptian source rocks in some South African Cretaceous basins, *Geological Society, London, Special Publications*, **207**, 185-202.

Van Schoor, M. and Fourie, C. J. S., 2014. The application of geophysics in South African coal mining and exploration, *Journal of the South African Institute of Mining and Metallurgy*, **114** (10), 875-879.

Viola, G., Andreoli, M., Ben-Avraham, Z., Stengel, I., and Reshef, M., 2005. Offshore mud volcanoes and onland faulting in southwestern Africa: neotectonic implications and constraints on the regional stress field, *Earth and Planetry Science Letters*, **231**, 147-160.

Viola, G., Kounov, A., Andreoli, M. A. G., and Mattila, J., 2012. Brittle tectonic evolution along the western margin of South Africa: more than 500 Myr of continued reactivation, *Tectonophysics*, **514-517**, 93-114. doi:10.1016/j.tecto.2011.10.009.

White, S., Stollhofen, H., Stanistreet, I. G., and Lorenz, V., 2009. Pleistocene to Recent rejuvenation of the Hebron Fault, SW Namibia, in: Reicherter, K.,

Michetti, A.M., and Silva, P. G. (Eds.), Palaeoseismology: Historical and Prehistorical Records of Earthquake Ground Effects for Seismic Hazard Assessment, *The Geological Society London Special Publications*, 316, 293-317. doi: 10.1144/SP316.18.

Zoback, M. D. and Zinke, J. C., 2002. Production induced normal faulting in the Valhall and Ekofisk oil fields, *Pure and Applied Geophysics*, **159**, 403-420.

# Chapter 2

# Seismic Wave

## 2.1 Introduction

Seismic waves are disturbances or energy that propagate through a medium (usually earth materials), causing a temporary displacement or deformation of particles within the medium. Away from the source such an earthquake or explosion, this temporary displacement is infinitesimally small and occurs through an elastic deformation that usually disappears after the disturbance causing the deformation is removed. Most earth materials including rocks exhibit elasticity, which is the ability to reverse back to their original condition after being deformed by external forces. An elastic material under the influence of external forces will experience a deformation that is exemplified by changes in size and shape. The relationship between these changes or deformation and the applied forces can be explained using the concepts of stress and strain.

Stress is the force acting on a unit area, and varies as the value of the force changes. It is important to distinguish between normal stress and shear stress. A stress is said to be normal if the force is acts perpendicular to the area, and shear when the force acts tangentially. Strain is the change that occurs when an elastic body is subject to a stress, and can be defined as the relative change or fractional change in a dimension or shape of a body. Similar to stress, strain can be distinguished into normal and shear strain depending on the direction of displacement.

## 2.2 Seismic wave theory

### 2.2.1 Seismic wave equation

A linear relationship exists between stress and the corresponding strain for a material under the influence of elastic deformation. This relationship is referred to as Hooke's law of elasticity, and holds only when the strains produced are infinitesimally small. Strains due to the passage of seismic waves are usually small and less than magnitude of $10^{-8}$ (Sheriff and Geldert, 1995), validating the application of Hooke's law in seismic wave propagation. According to Hooke's law, strain ($\boldsymbol{\varepsilon}_{ii}$) is directly proportional to the stress ($\boldsymbol{\sigma}_{ii}$), and the ratio of the stress to strain defines an elastic constant (or an elastic modulus). Based on this stress/strain relationship, elastic moduli can be defined for different types of deformation, including Young's modulus, rigidity modulus, and the bulk modulus.

Young's modulus is defined from the extensional deformations, where each longitudinal strain component ($\boldsymbol{\varepsilon}_{ii}$) is proportional to the corresponding longitudinal stress ($\boldsymbol{\sigma}_{ii}$) components, that is;

$\boldsymbol{\sigma}_{xx} = \mathbf{E}\boldsymbol{\varepsilon}_{xx}$, $\boldsymbol{\sigma}_{yy} = \mathbf{E}\boldsymbol{\varepsilon}_{yy}$, and $\boldsymbol{\sigma}_{zz} = \mathbf{E}\boldsymbol{\varepsilon}_{zz}$ (using the Einstein summation notation) (2.1)

The constant of proportionality, **E**, is the Young's modulus.

The rigidity modulus (or shear modulus) is defined from shear deformations. Like longitudinal strain, each shear strain ($\boldsymbol{\varepsilon}_{ij}$) component is proportional to the corresponding shear stress component ($\boldsymbol{\sigma}_{ij}$), that is;

$$\boldsymbol{\sigma}_{xy} = \boldsymbol{\mu}\boldsymbol{\varepsilon}_{xy},\ \boldsymbol{\sigma}_{yz} = \boldsymbol{\mu}\boldsymbol{\varepsilon}_{yz},\ \text{and}\ \boldsymbol{\sigma}_{zx} = \boldsymbol{\mu}\boldsymbol{\varepsilon}_{zx} \qquad (2.2)$$

The proportionality constant, **μ**, is the rigidity modulus.

The bulk modulus (or incompressibility) is defined from the dilatation or change in volume experienced by a body under hydrostatic pressure. For a body under a hydrostatic condition, the shear component is equal to zero, while the normal stress or pressure is directed inwardly (-p) and equal in all directions. The pressure (-p) causes a decrease in the volume, and the change in volume per unit volume is called the dilatation (Δ). Hence, the bulk modulus, K, is the ratio of the hydrostatic pressure to the dilatation; that is,

$$\mathbf{K} = -p/\Delta \qquad (2.3)$$

The inverse of the bulk modulus ($K^{-1}$) is the compressibility.

Generally, in an isotropic medium (i.e. when properties do not depend on the direction) Hooke's law's proportionality relating the stress and the strain leads to complicated relations that can be expressed in relatively simple equations (Timoshenko and Goodier, 1951; Love, 1944):

$$\boldsymbol{\sigma_{ii}} = \boldsymbol{\lambda\Delta} + \mathbf{2\mu\varepsilon_{ii}} \qquad (i = x, y, z), \qquad (2.4)$$

$$\boldsymbol{\sigma_{ij}} = \mathbf{2\mu\varepsilon_{ij}} \qquad (i, j = x, y, z: i \neq j). \qquad (2.5)$$

The quantities **λ** and **μ** are known as Lamê's constants, and **μ** is a measure of the resistance to shearing strain referred to as the modulus of rigidity, incompressibility, or shear modulus.

In an elastic body, deformation causing an increase in length in one direction will cause a corresponding decrease in the other direction. Assuming a positive

longitudinal strain occurs along the x- direction ($\varepsilon_{xx}$), which causes a corresponding decrease in longitudinal strain in the y- and z- directions. If the longitudinal strain along x- direction ($\varepsilon_{xx}$) is taken to be positive, then the transverse longitudinal strains ($\varepsilon_{yy}$) and ($\varepsilon_{zz}$) along the y- and z- direction respectively will be negative but proportional to $\varepsilon_{xx}$. Hence, this relationship can be expressed as

$$\boldsymbol{\varepsilon_{yy} = -\nu\varepsilon_{xx}} \text{ and } \boldsymbol{\varepsilon_{zz} = -\nu\varepsilon_{xx}} \quad (2.6)$$

The constant of proportionality, **ν**, is the Poisson's ratio.

The relationship between the elastic constants **E**, **ν**, and **K**, and the Lamê's constants, **λ** and **μ** can be obtained by substituting the values of **E**, **ν**, and **K** from the preceding equations in Hooke's law, which result in the following expressions;

$$\mathbf{E} = \frac{\mu(3\lambda+2\mu)}{\lambda+\mu} \quad (2.7)$$

$$\boldsymbol{\nu} = \frac{\lambda}{2(\lambda+\mu)} \quad (2.8)$$

$$\mathbf{K} = \frac{1}{3}(3\lambda + 2\mu) \quad (2.9)$$

$$\boldsymbol{\lambda} = \frac{\boldsymbol{E\nu}}{(\mathbf{1}+\boldsymbol{\sigma})(\mathbf{1}-\mathbf{2}\boldsymbol{\sigma})} \quad (2.10)$$

### 2.2.2 Types of seismic waves

Seismic waves consist of body waves that travel through the body of a medium, and surface waves that travel along the free surfaces and interfaces between layers

with contrasting elastic properties, particularly the ground surface. Two types of body waves can be identified based on the nature of elastic deformation and mode of propagation. The first type of body wave causes change in compression and dilatation, and is referred to as a P-, compressional, longitudinal, or dilatational wave. The P-wave is the first (primary) event to be recorded after an earthquake, and propagates longitudinally in the direction of particle displacement (Fig. 2.1a).

The second type of body wave causes shearing or changes in shape. It is referred to as the secondary wave (as it is the second major event to be observed on an earthquake record), S-wave, rotational, or transverse wave. It propagates in a perpendicular direction to particle displacement (Fig. 2.1b). Plane polarization of S-waves can occur if particle vibration or motion is restricted to one plane only. In this case, the displacement of the particle can occur only in a vertical plane (vertically polarized SV-wave) or along a horizontal plane (horizontally polarized SH-wave).

The surface wave consists of the Rayleigh and the Love waves. The Rayleigh waves, also known as ground roll, are the most important surface waves, because they constitute the major component of noise caused by surface waves in near-surface reflection seismic data. They travel along the free surface of the Earth with amplitudes that decrease exponentially with depth, and give rise to particle motion that is in a vertical plane containing the direction of wave propagation. The particle motion in Rayleigh waves at the surface is retrograde (i.e. having an elliptical particle motion that is opposite in direction to the propagation direction) (Fig. 2.2a). Rayleigh waves are coupled P- and SV-waves trapped within the near surface (Yilmaz, 2015), and travel only through the solid medium.

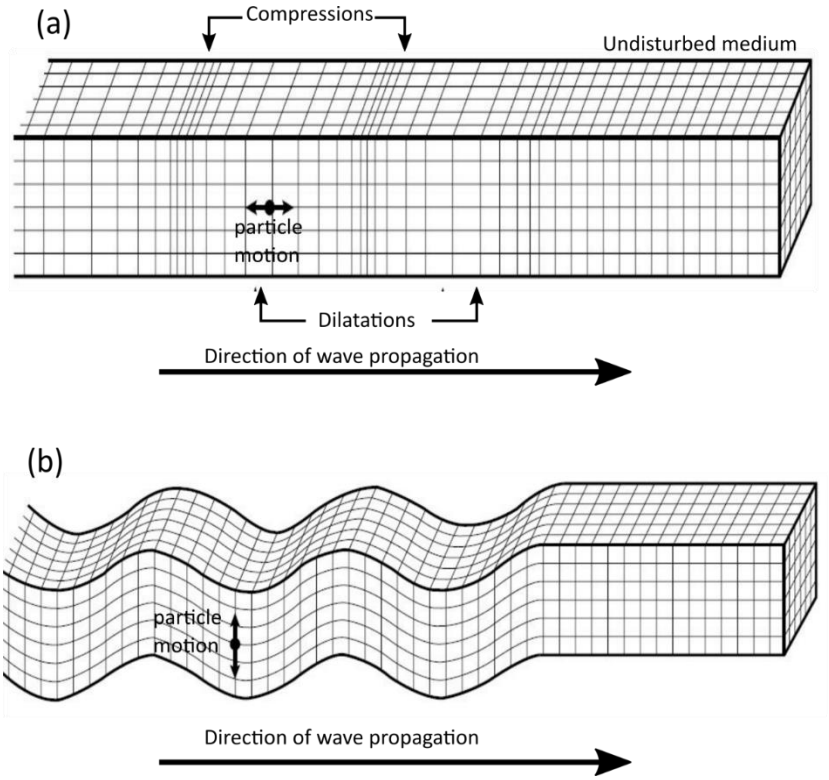



Figure 2.1: Elastic deformations and ground particle motions associated with the passage of body waves. (a) P-wave, (b) S-wave (modified after Kearey et al., 2002).

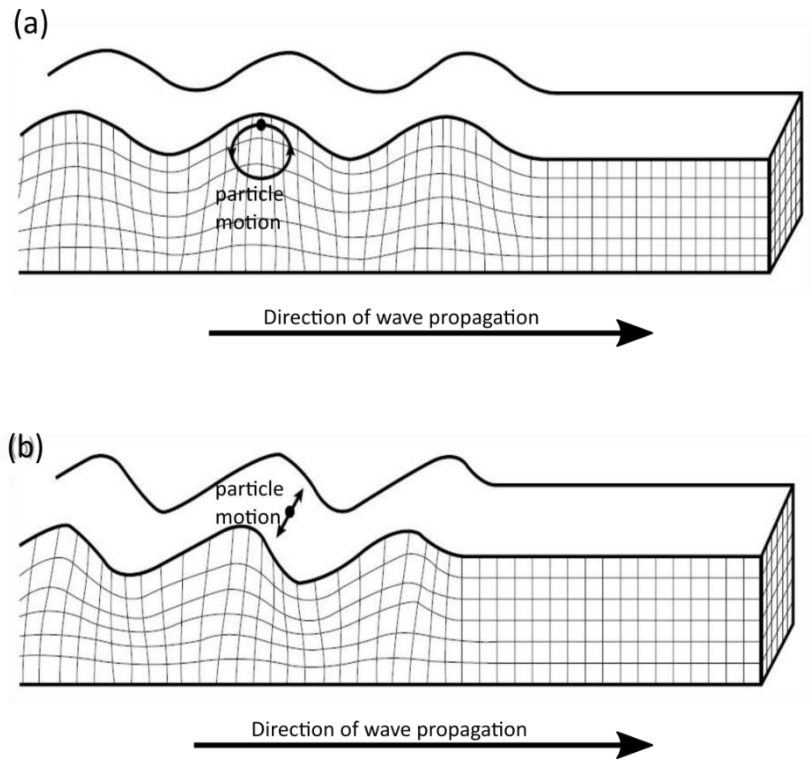



Figure 2.2: Elastic deformations and ground particle motions associated with the passage of surface waves. (a) Rayleigh wave. (b) Love wave. (modified after Kearey et al., 2002)

Love waves occur only where a medium with a low S-wave velocity overlies a layer with a higher S-wave velocity (Reynolds, 2011), and are horizontally polarized shear waves (SH-waves) characterized by a particle whose motion is perpendicular to the direction of wave propagation but parallel to the surface (Fig. 2.2b).

### 2.2.3 Seismic wave velocities

Seismic wave propagation can be described by the combination of Hooke's law and Newton's second law of motion. If a force, $F_x$, acting on rock produced an infinitesimal increase in length, dx, of a small volume element of the rock which has mass $\rho dx.A_x$, where $\rho$ is the density of the rock and Ax is the unit area. The net force acting on this element of rock in the x- direction is given by

$$dF_x = \frac{\partial F_x}{\partial x} dx \tag{2.11}$$

If the force, $F_x$, is caused by the stress element $\sigma_{xx}$ acting on the area $A_x$, and is equal to $\sigma_{xx}A_x$, then the equation of motion along the x- direction becomes:

$$(\rho dx A_x)\frac{\partial^2 u}{\partial t^2} = dx A_x \frac{\partial \sigma_{xx}}{\partial x} \tag{2.12}$$

Hooke's law in equation (2.3) in terms of a strain in x- direction is given by

$$\sigma_{xx} = E\varepsilon_{xx} = E\frac{\partial u}{\partial x} \tag{2.13}$$

Substitution of equation (2.13) into equation (2.12) gives the displacement equation along the x- direction in terms of strain (e.g., Lowrie, 1997):

$$\frac{\partial^2 u}{\partial t^2} = V^2 \frac{\partial^2 u}{\partial x^2} \tag{2.14}$$

where V is the velocity of the wave given by:

$$V = \sqrt{\frac{E}{\rho}} \tag{2.15}$$

For a longitudinal or compressional P-wave that passes through a medium as a series of dilatations and compressions, equation (2.14) becomes;

$$\frac{\partial^2 \Delta}{\partial t^2} = \alpha^2 \frac{\partial^2 \Delta}{\partial x^2} \tag{2.16}$$

where α is the wave velocity and, using equation (2.9), is given by:

$$\alpha = \sqrt{\frac{\lambda + 2\mu}{\rho}} = \sqrt{\frac{K + \frac{4}{3}\mu}{\rho}} \tag{2.17}$$

Liquids and gases do not shear, therefore μ for liquids and gases is zero, and equation (2.17) for wave velocity in liquid and gases becomes:

$$\alpha = \sqrt{\frac{K}{\rho}} \tag{2.18}$$

Similarly, the shear wave velocity (β) is given by:

$$\beta = \sqrt{\frac{\mu}{\rho}} \tag{2.19}$$

The modulus of rigidity, μ, is zero for fluids, hence β also becomes zero. Therefore, shear waves do not propagate through liquids and gases. The Poisson's ratio (ν) for any material can be determined by taking the ratio of the velocity of P- and S-waves (Kearey et al., 2002), which gives:

$$\alpha/\beta = \sqrt{\frac{2(1-\nu)}{(1-2\nu)}} \tag{2.20}$$

The seismic velocity in rocks depends on several factors, which include porosity, lithology, cementation or burial history, depth, age, pressure regime, and interstitial fluids (Sheriff and Geldart, 1995). The velocity of P-waves in rocks is markedly affected by the nature of the interstitial fluid or fluids present within the pores, and can show a significant decrease when, for example, water is replaced by gas. This is particularly important in the near-surface, where a low velocity layer (weathered layer) exists above the water table.

Near-surface materials such as sand, silt, and clay always have P- and S-wave velocities that are much lower than those of the subsurface rocks. In a shallow soil column, typical P-wave velocity ranges between 400- 800 m/s, and sometimes as low as 150 m/s, or as high as 1200 m/s (Sheriff and Geldart, 1995; Yilmaz, 2015). The velocity of S-waves can be as low as 100 m/s, and may increase to approximately 700 m/s as depth of the soil column increases (Yilmaz, 2015). Seismic wave velocities in soils are influenced by porosity, pore shape, pore pressure, pore fluid saturation, confining pressure, and temperature (Yilmaz, 2015).

Surface waves are generally confined to a low velocity near-surface layer, such as a soil column, and diminish as they get farther from the surface. They propagate in horizontal directions with phase velocity that depends on the frequency or wavelength, which causes them to be dispersive. Love waves are intrinsically dispersive even in a homogeneous layer overlying a heterogeneous half-space (Lowrie, 1997), while Rayleigh waves are non-dispersive in a homogenous half-space. Surface waves generally have phase velocities that are less than P-wave velocities and equal to or less than S-wave velocities (Yilmaz, 2015).

### 2.2.4 Seismic energy decay

The energy of a seismic wave becomes weaker as it travels away from the source, resulting in amplitude that decreases with increasing distance from the source. This decrease in amplitude is known as attenuation, and is partly due to the spherical or geometrical spreading of the seismic wave as it propagates away from its source, and partly due to absorption of energy as the seismic wave travels through imperfect elastic materials (Lowrie, 1997). As the seismic energy propagates away in a spherical spread from the source (Fig. 2.3), its intensity, which is the energy per unit area of the wavefront, is inversely proportional to the spherical distance, $r$, away from the source. Therefore, as the wavefront spreads from $r_1$ to $r_2$, the amplitude loss, $A_0$, in decibel (dB) is;

$$A_0 = 10\log \frac{r_2}{r_1} \tag{2.21}$$

where $r_1$ and $r_2$ are the radial distance from the source. During seismic data processing, this amplitude loss due to geometrical spreading is recovered by

correction using a processing algorithm that is based on the equation (2.21) (Evans, 1997).

Amplitude is also lost due to absorption when a wavefront vibrates through rock particles. This loss of energy, which is in form of heat energy, varies exponentially with distance from the source, and can be expressed in terms of amplitude (Evans, 1997) as;

$$A_2 = A_1 e^{-q(r_2 - r_1)} \tag{2.22}$$

where $A_1$ and $A_2$ are the amplitude at distance $r_1$ and $r_2$ respectively, and q is the absorption coefficient of the material.

$$\text{The absorption loss in decibels (dB)} = 10\log e^{-q(r_2 - r_1)} \tag{2.23}$$

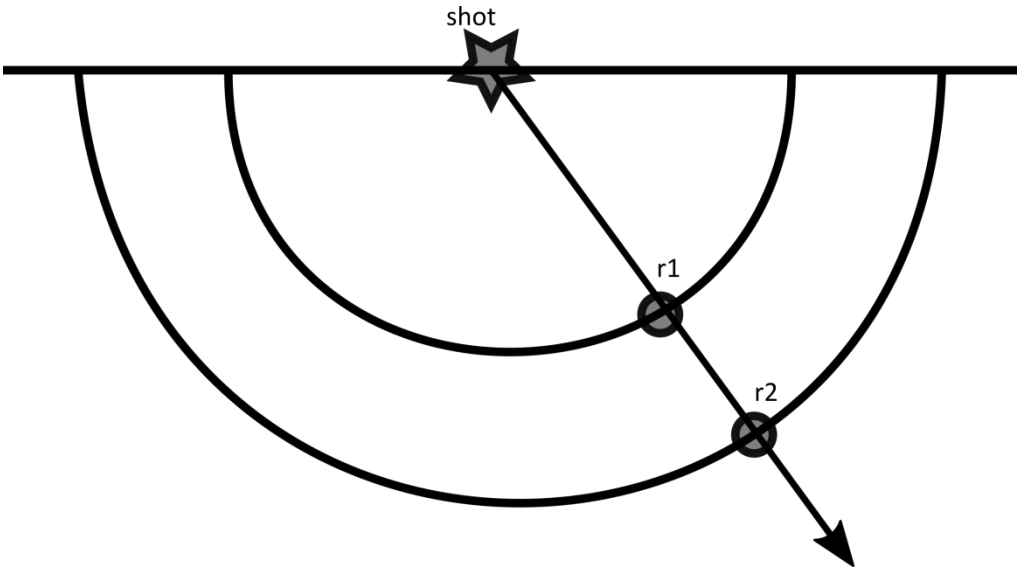



Figure 2.3: Energy losses due to spherical divergence of the seismic wave, $r_1$ and $r_2$ are the radial distance from the source (modified after Evans, 1997).

The values of q express the proportion of energy lost during transmission through a distance equivalent to a complete wavelength ($\lambda_d$), and range from 0.25-0.75

$dB\lambda^{-1}$ for common earth materials (Kearey et al., 2002). Assuming q is 0.25 $dB\lambda^{-1}$, and wavelength $\lambda_d = v/f$, equation (2.23) can be expressed in terms of the velocity (v) and the dominant frequency (*f*) (Evans, 1997) as;

$$\text{Absorption loss in dB} = \frac{1.1\, f(r_2 - r_1)}{v} \qquad (2.24)$$

Thus equation (2.24) implies that for a fixed velocity, absorption loss depends on the frequency and the distance from the source. Hence, higher frequency waves are attenuated more rapidly than lower frequency waves as a function of distance, assuming the seismic velocity is constant.

### 2.2.5 Seismic resolution

The seismic resolution limit refers to the minimum separation between two features in seismic data for which they can be clearly distinguished. It may also be referred loosely to the minimum feature that can be seen or detected in seismic data (Sheriff and Geldart, 1995). Hence, it is pertinent to differentiate between seismic resolution limit and detection limit. Seismic resolution has to do with two seismic events that are separated and have boundaries that can clearly be distinguished from each other, while detection limit is the minimum thickness for a bed to give a reflection and stand out above the background (Sheriff and Geldart, 1995). The limit of resolution is determined by the tuning thickness, which is equal to a quarter wavelength in thickness of a bed (Widess, 1973). It is the thickness for which constructive or destructive interference will occur between the reflections from the upper and lower interface of a bed (Widess, 1973).

Seismic resolution comprises both vertical and horizontal resolutions. The vertical resolution, in terms of a seismic wave, can be defined as how far apart, in space or time, two interfaces must be to show as separate reflectors on a seismic record (Sheriff and Geldart, 1995). Vertical resolution determines the vertical limit or bed thickness that is seismically resolvable. Provided an appreciable acoustic impedance contrast exists among subsurface layers, vertical resolution is fundamentally dependent on the predominant frequency of the seismic signal (*f*), interval velocity of the subsurface media (v), and the predominant wavelength in the seismic signal ($\lambda_d$). Generally, vertical resolution decreases with depth due to frequency loss and increases in interval velocity (e.g. Widess, 1973; Sheriff, 1977). Therefore, wavelength ($\lambda_d$), which is the yardstick for measuring vertical resolution, depends on the velocity (v) and the frequency (*f*), and can be expressed as follows (Yilmaz, 2001);

$$\lambda_d = \frac{v}{f} \tag{2.25}$$

Equation (2.25) thus implies that a higher frequency is required to achieve higher resolution (Sheriff, 1977). The generally acceptable threshold for vertical resolution is $\lambda_d/4$ given by Widess (1973), where $\lambda_d$ is the predominant wavelength. This criterion is however subjective and depends on the signal- to-noise ratio of the seismic data, as well as the reflection coefficient at the reflector's boundary (Yilmaz, 2015).

Similarly, the horizontal or lateral resolution, in terms of a seismic wave, can be defined as how far apart two features involving a single interface must be separated to show as separate features (Sheriff and Geldart, 1995). The horizontal

resolution, like the vertical resolution, is also affected by several factors such as signal/noise ratio, trace spacing (sampling), bin size, frequency bandwidth, and, most importantly, the radius of the Fresnel zone. The Fresnel zone is defined as the circular area on a subsurface reflector at a depth which reflects energy that arrives at earth's surface within a time delay equal to half the dominant period (T/2) (Chaouch and Mari, 2006). The radius of the Fresnel zone is the limiting factor that determines the lateral or horizontal resolution on unmigrated seismic data, and is affected by the depth to the reflector ($Z_0$), velocity above the reflector (v), and the dominant wavelength (λ). The radius of the Fresnel zone, as given by Yilmaz (2001), is;

$$F_r = \sqrt{\frac{Z_0 \lambda}{2}} \tag{2.26}$$

This equation implies that the longer the dominant wavelength, the greater the radius of the Fresnel zone, and the lower the horizontal resolution. Since wavelength varies as an inverse of frequency, higher resolution is expected at higher frequencies. However, higher frequencies are usually attenuated more strongly as depth increases, resulting in deterioration of lateral resolution with depth.

Migration usually improves the lateral resolution by reducing the width of the Fresnel zone. This improvement in lateral resolution is significantly achieved in the 3-D migration of 3-D seismic data, as compared to 2-D data (Yilmaz, 2001), because of energy that is better focused, and the shortening of the radius of the Fresnel zone that occurs in all directions (Chaouch and Mari, 2006). In theory, the

lateral resolution is equal to approximately one-half the dominant wavelength ($\lambda_d/2$) after migration (Liner, 2016), but this is usually difficult to achieve in practice because of the limitation set by the bin size and the signal-to-noise ratio. Therefore, the lateral resolution obtainable in practice after migration of seismic data is usually equal to the dominant wavelength ($\lambda_d$) (Stolt and Benson, 1986).

## 2.3 Methodology

### 2.3.1 Seismic reflection method

The seismic reflection method is directed primarily at finding the depths to reflecting surfaces and the seismic velocities of subsurface rock layers (Lowrie, 1997). The method is based on the recording and analysis of the echoes reflected from the boundaries between rock layers with different seismic velocities and densities. This practice usually involves a seismic wave produced at the surface (e.g., explosion) at a known place at a known time that impinges on reflectors (geological layers) at depth and returns to the surface to be detected by a group of geophones arranged within the critical distance from the source point (Fig. 2.4). The path taken by the seismic wave is a two-way path, and the time it takes to return back to the surface is recorded as a two-way travel-time. The seismic reflection method is applicable to imaging deeply-seated subsurface features, and can provide high resolution images of features at greater depth that are often not visible to other geophysical methods such as gravity, magnetic and electrical methods. This technique is very popular in the oil industry, where it is used to image the stratigraphic and structural features that may trap hydrocarbons.

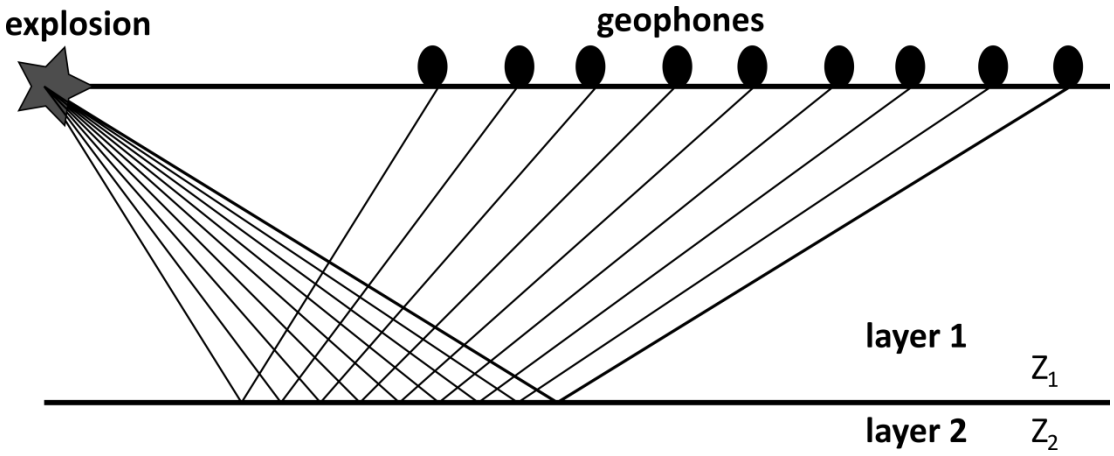



Figure 2.4: An illustration of the principle of reflection seismic method. Z1 and Z2 are the acoustic impedance of layers 1 and 2 respectively, (Z2 > Z1).

An important parameter in the application of the seismic reflection technique in exploration is the acoustic impedance (Z), which is the product of density (ρ) and seismic velocity (v). This parameter determines the amplitude and polarity of reflections at the boundary between two layers with contrasting acoustic properties. When a seismic wave arrives at the interface between two layers of different acoustic properties, part of the seismic energy is reflected, while part is transmitted (Fig. 2.5). The fraction of the incident energy that is reflected depends on the reflection coefficient ($R_C$), which is the measure of the acoustic impedance (Z) contrast between the two layers. Hence, assuming a normal incidence (Fig. 2.5), the relationship between the amplitude of the reflected wave ($A_r$) and the incident wave ($A_i$) can be expressed as:

$$A_r = R_C A_i \tag{2.27}$$

where $R_C$ is given by;

$$R_C = \frac{Z_2 - Z_1}{Z_2 + Z_1} = \frac{\rho_2 V_2 - \rho_1 V_1}{\rho_2 V_2 + \rho_1 V_1} \tag{2.28}$$

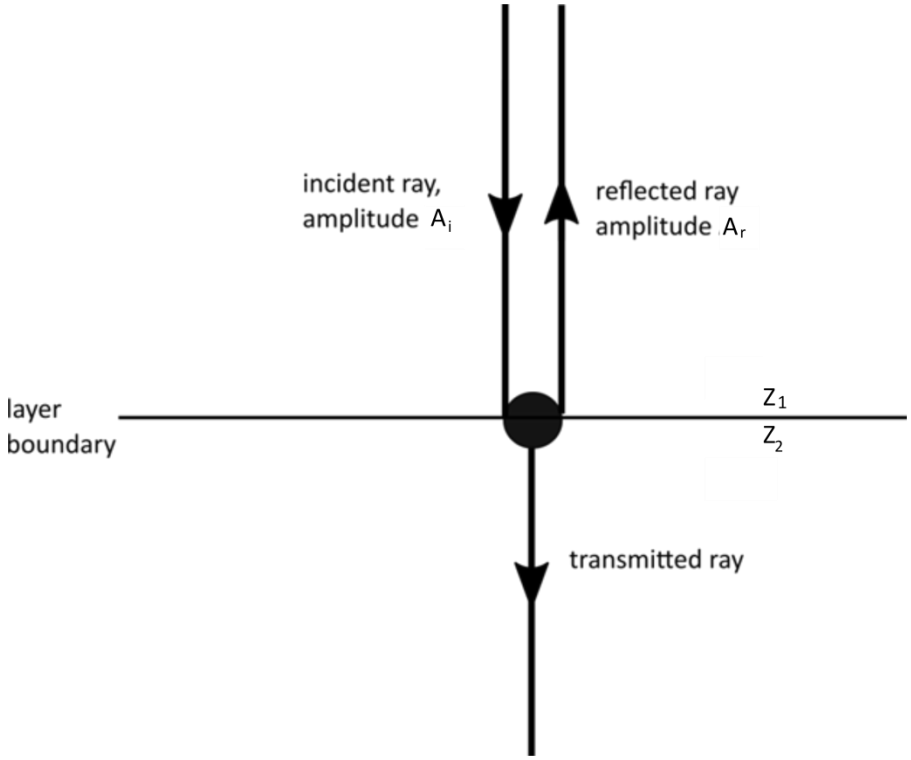



Figure 2.5: Reflected and transmitted rays associated with a ray arriving at normal incidence on an interface with appreciable impedance contrast (Z2 > Z1) (modified after Kearey et al., 2002)

It can be deduced from equation (2.28) that the higher the acoustic impedance (Z) contrast between two layers, the higher the reflectivity, and the better the detection of the boundary between the two layers. The values of $R_C$ range from -1 to +1, and become negative when the layer below the interface has lower acoustic impedance, compared to the layer above. In this case, the polarity of the reflected wave is opposite to the incident wave. Generally, any abrupt change in acoustic impedance will give rise to reflection, and a large $R_C$ value implies less energy transmission and high signal - noise ratio of the reflected wave.

### 2.3.2 Reflection seismic application to near-surface investigation

The reflection seismic method is usually considered to be an expensive geophysical method only suitable for the large-scale exploration for oil and gas. However, recent advancements in the technology of acquisition and processing of reflection seismic data has seen the emergence of affordable seismographs and cost-effective computers (Yilmaz, 2015). This has made the application of the reflection seismic method possible in small-scale exploration involving near-surface investigations. Near-surface refers to a region of tens to a few hundred meters below the ground surface. This region is generally composed of low-velocity, unconsolidated weathered rocks to relatively higher velocity, consolidated sedimentary and crystalline rocks. The technique employed in the oil and gas industry is similar to the application in near-surface, with the scale of investigation being the major difference. There are several methods employed in reflection seismic data acquisition for near-surface investigation, but the most popular is the common midpoint method (CMP). This method involves a spread of several geophones (ranging from 24 to 96- channels) that are laid out at regular intervals along a profile through the shot points.

Seismic energy sources in near-surface investigations are of several types, and can be classified into impact source and explosive source. Impact source includes sledge-hammers of about 5- 10 kg weight, weight drops, and accelerated weight drops, while dynamite, sparker, and guns are common examples of the explosive source (e.g. Yilmaz, 2015). The most commonly used seismic source is the sledgehammer, because it is relatively cheap, portable, easy to use and relatively safe (Pelton, 2005). Traditional recording systems in reflection seismic

investigations are usually a set of geophones connected to a take-out cable, which consists of 6-, 12-, 24-, 48-, 72- or 96- channel systems. However, modern developments have seen the utilization of land streamer (similar to offshore surveys), which is a towed array of geophones fixed on sleds (e.g. van der Veen et al., 2001; Miller et al., 2002; Pugin et al., 2002; Yilmaz, 2015), as well as the use of wireless recording systems (e.g. Yilmaz, 2015). These developments have significantly increased the efficiency and the ease of conducting shallow reflection surveys in the urban area as documented by numerous authors (e.g. Pugin et al., 2004; Yilmaz et al, 2006; Pullan et al., 2008; Krawczyk et al., 2012; Pugin et al., 2013).

The choice of geophones used in near-surface reflection seismic investigations depends on the type of waves to be recorded and the direction of wave propagation (Pelton, 2005). It is a common practice to detect P - and S-waves using vertical and horizontal geophones, respectively. This practice is based on the theoretical understanding of body wave propagation in a homogenous and isotropic elastic media. For example, when the direction of body-wave propagation is approximately vertical, P-wave should record best on a vertical geophone, while the S-wave should record best on horizontal geophones.

In order to eliminate high-amplitude, low-frequency surface wave energy during recording, Yilmaz (2015) recommends the use of vertical-component geophones, with a resonance frequency of 40 Hz or higher for shallow reflection seismic utilizing P-wave seismic imaging. S-wave reflections generally have lower frequency than P-wave reflections. Therefore, it is preferable to use horizontal component geophones with resonance frequency less than 40 Hz for seismic

surveys utilizing S-wave reflections (Yilmaz, 2015). The use of geophones with moderate natural frequency ranges between 25-40 Hz has also been suggested by Li et al. (2009) for shallow seismic exploration. Since high-resolution is the ultimate goal of shallow reflection seismic exploration, the geophone to be employed must be capable of recording the effective frequency that will provide a large signal-to noise ratio and high-resolution information (Li et al., 2009).

### 2.3.3 Sources of noise in near-surface reflection seismic data

Noise is one of the major problems usually encountered in near-surface applications of the reflection seismic method. The signal quality of near-surface reflection seismic data is profoundly affected by noise, which, based on source, can be due to the shot itself or to external sources such as wind or traffic (Ernst et al., 1998). The major causes of noise due to the shot are the irregularities and heterogeneities that exist near the earth's surface or within the soil overburden, which causes the scattering of the wave-field. This effect often results in coherent and dispersive events, such as surface waves or scattered ground roll that interferes with the reflection events.

Near-surface moisture content due to the saturated condition of the soil has also been reported as a major cause of the noise due to the shot (e.g. Jefferson et al., 1998). Large amplitude wavelets generated from highly saturated near-surface conditions can mask or degrade reflection events. Secondary reflections or multiples also constitute important examples of noise due to the shot, and can be caused by near-surface irregularities or shallow water-table condition (e.g. Miller and Xia, 1998). Another important cause of noise due to the shot is the

reverberation of the base-plate or the sledge-hammer during seismic data recording. This effect arises when multiple rebounds of the sledgehammer on the base plate occur, giving rise to false reflections or signal duplication on seismic data.

### 2.3.4 Seismic attributes

Seismic attributes are special quantities derived from seismic data that can be used to enhance the visualization of features of interest, which sometimes are too subtle to see or difficult to describe in seismic data. These special quantities are any measure of a seismic characteristic of interest, and could contain geometric, kinematic, dynamic, or statistical features (Chopra and Marfurt, 2007; Liner, 2016). Besides their use as visual enhancement, seismic attributes are also used to quantify features of interpretation interest, such as structural or depositional features (Chopra and Marfurt, 2007), or to predict reservoir properties (Liner, 2016). Since their introduction in the 1970s, many seismic attributes have been developed and this technology is still growing. Taner et al. (1979) were the first to describe seismic attributes using the concept of complex traces analysis, which they defined as:

$$CT(t) = T(t) + iH(t) \tag{2.29}$$

where $CT(t)$ is the complex seismic trace, $T(t)$ is the real part of the seismic trace, and $H(t)$ is the imaginary part or the Hilbert's transform of $T(t)$. Their analysis of seismic traces as part of complex (analytic) signals allows the determination of three complex seismic attributes namely, amplitude of the envelope or reflection strength, instantaneous phase, and instantaneous frequency.

Basically, seismic attributes involve one or a combination of more functions derived from the five attributes that describe seismic wave propagation in time and frequency domains. These five attributes are amplitude, period, polarity, frequency and phase. Examples include single trace attributes, such as the complex trace attribute or the instantaneous attributes. Multi-trace attributes are those derived from the calculation of coherence coefficients, which are a measure of trace to trace similarity or discontinuity, and include seismic attributes such as correlation, similarity, variance, and semblance. Recent advancement in the technology of seismic image processing has also seen the development of seismic attributes from tools that are common in medical imaging and digital photography (Liner, 2016). Examples of these attributes include texture segmentation and volume rendering.

**References**

Chaouch, A. and Mari, J. L., 2006. 3-D land seismic surveys: Definition of geophysical parameters, *Oil and Gas Science and Technology*, **61**, 611-630, doi:10.2516/ogst: 2006002.

Chopra, S. and Marfurt, K. J., 2007. Seismic attributes for prospect identification and reservoir characterization, in Hill, S. J. ed., *Society for Exploration Geophysicists Geophysical Developments Series*, **11**, 464 pp.

Ernst, F., Herman, G. and Blonk, B., 1998. Acquisition/processing-reduction of near-surface scattering effects in seismic data, *The Leading Edge*, **17**, 759-764.

Evans, B. J., 1997. A Handbook for Seismic Data Acquisition in Exploration, in Dragoset, G. H. Jr., ed., *Society for Exploration Geophysicists, Geophysical monograph series*, **7**, 305 pp.

Jefferson, R. D., Steeples, D. W., Black, R. A. and Carr, T., 1998. Effects of soil-moisture content on shallow-seismic data, *Geophysics*, **63**, 1357-1362.

Kearey, P., Brooks, M. and Hill, I., 2002. An Introduction to Geophysical Exploration, Third edition, *Blackwell Scientific Publisher*, Oxford, UK.

Krawczyk, C. M., Polom, U., Trabs, S. and Dahm, T., 2012. Sinkholes in the city of Hamburg: New urban shear-wave reflection seismic system enables high-resolution imaging of suberosion structures, *Journal of Applied Geophysics*, **78**, 133-143, doi:10.1016/j.jappgeo.2011.02.003.

Li, G., Gao, C. and Junyi, Z., 2009. Analysis of geophone properties effects for land seismic data, *Applied Geophysics*, **6**, 93-101, doi:10.1007/s11770-009-0003-4.

Liner, C. L., 2016. Elements of 3D seismology, in R. Latimer, ed., *Society of Exploration Geophysicists Investigations in Geophysics*, **19**, 340 pp.

Love, A. E. H., 1944. A Treatise on the Mathematical Theory of Elasticity, New York, Denver.

Lowrie, W., 1997, Fundamentals of Geophysics, *Cambridge University Press*, Cambridge, U.K.

Miller, R. D. and Xia, J., 1998. Large near-surface velocity gradients on shallow seismic reflection data, *Geophysics*, **63**, 1348–1356.

Miller, R. D., Park, C. B., Anderson, T. S., Ballard, R. F., Park, K., Xia, J. and Moran, M. L., 2002. Wavefield imaging to detect underground facilities, Proceedings of the Millitary Sensing Symposia Specially Group on Battlefield Acoustic and Seismic Sensing, August 23-26, Laurel, Maryland.

Pelton, R. J., 2005. Near-surface seismology: Surface-Based Methods, in: Butler, D. K. ed., Near-Surface Geophysics II, *Society for Exploration Geophysics Investigation in Geophysics*, **13**, 219-263.

Pugin, A. J. M., T. H. Larson, M. L. and Philips, A., 2002. Shallow high-resolution shear-wave seismic reflection acquisition using a land-streamer in the Mississippi River: Proceedings of the Symposium on the Application of Geophysics to Engineering and Environmental Problems (SAGEEP), 3-12.

Pugin, A. J. M., T. H. Larson, A., and Sargent, S. L., 2004. 3.5 km/day of high-resolution seismic reflection data using a land-streamer: Proceedings of the Symposium on the Application of Geophysics to Engineering and Environmental Problems (SAGEEP), 1380-1384.

Pugin, A. J. M., Pullan, S. E. and Hunter, J. A., 2013. Shear-wave high resolution seismic reflection surveys in Ottawa and Quebec City, Canada, *The Leading Edge*, **32**, 936-940, doi:10.1190/tle32030250.1.

Pullan, S. E., Pugin, A. J. M., Hunter, J. A., Cartwright, T. and Douma, M., 2008. Application of P-wave seismic reflection methods using the landstreamer-minivib system to near-surface investigations: Symposium on the Application of Geophysics to Engineering and Environmental Problems (SAGEEP), 359-367.

Reynolds, J. M., 2011. An introduction to Applied and Environmental Geophysics: Second edition, *John Wiley and Sons Publishing*, Oxford, U.K.

Sheriff, R. E., 1977. Limitations on resolution of seismic reflections and geologic detail derivable from them, *American Association of Petroleum Geologists Memoir*, **26**, 3-14.

Sheriff, R. E. and Geldart, L. P., 1995. Exploration Seismology, *Cambridge University Press*, Cambridge.

Stolt, R. H. and Benson, A. K., 1986. Seismic migration- theory and practice: Geophysical Press, London-Amsterdam.

Taner, M. T., Koehler, F. and Sheriff, R. E., 1979. Complex seismic trace analysis, *Geophysics*, **44**, 1041-1063.

Timoshenko, S. and Goodier, J. N., 1951. Theory of elasticity, New York, McGraw-Hill.

Van der Veen, M., Spitzer, R., Green, A. G. and Wild, P., 2001. Design and application of a towed land-streamer system for cost effective 2D and pseudo-3D shallow seismic data acquisition, *Geophysics*, 66, 482-500, doi:10.1190/1.1444578.

Widess, M. B., 1973. How thin is a thin bed? *Geophysics*, **38**, 1176-1180.

Yilmaz, Ö., 2001. Seismic data analysis: Processing, inversion, and interpretation of seismic data, *Society for Exploration Geophysicists Investigations in Geophysics*, **10**, doi:10.1190/1.9781560801580.

Yilmaz, Ö., Eser, M. and Berilgen, M., 2006. A case study for seismic zonation in municipal areas, *The Leading Edge*, **25**, 319-330, doi:10.1190/1.21841100.

Yilmaz, Ö., 2015. Engineering seismology with applications to geotechnical engineering, in Miller, R. D. ed., *Society for Exploration Geophysicists Investigation in Geophysics*, **17**. 948 pp.

# Chapter 3

# High-resolution Seismic Reflection Investigation of Subsidence and Sinkholes at Abandoned Coal Mine Sites in South Africa


**Summary**

The high-resolution seismic reflection method was used to investigate subsidence and sinkholes at two abandoned coal mine sites located in the Benoni area, near the city of Johannesburg, and Springlake Colliery near the town of Dundee in the Kwazulu-Natal Province. The investigation conducted in the two study areas has revealed the evidence of subsidence and sinkholes that are related to subsurface voids. In the Benoni area, near-surface coal-mining-related voids and dissolution cavities that occur within the underlying dolomite layer at the depth below about 50 m were found to be the major cause of subsidence- and sinkhole-related features that are common in the area. The suspected doleritic layer encountered in the boreholes in the north of the area was confirmed by the investigation to be an extensive sill of thickness of about 13 m. Similarly, in the Springlake mine, evidence of near-surface subsidence was confirmed by the investigation conducted within the suspected mined-out zones, where the major cause of subsidence is due to the collapse of the overburden strata into subsurface void created by the removal of coal. The observed subsidence thereby provide evidence that previous coal-mining activities in the area have extended beyond the known mined-out zones indicated in the Springlake Colliery mine plan.

## 3.1 Introduction

Subsurface cavities resulting from coal mining or dissolution of carbonate rocks (e.g., limestone and dolomite), may give rise to sudden catastrophic phenomena such as subsidence or sinkholes. These are common environmental hazards in many South Africa's abandoned coal mines sites and large areas underlain by carbonate rocks of the Transvaal Basin (2.65-2.05 Ga). At least 38 people were reported to have died in South Africa over the last 50 years in subsidence and sinkhole-related incidences, while the cost of damage caused by these hazards has been estimated to be in excess of R1 billion (~$70 Million) (e.g., Van Schalkwyk, 1998; Buttrick et al. 2001). The widespread occurrence of sinkholes and subsidence in South Africa has been largely attributed to ancient karst weathering events that occurred in the Karoo Basin (~ 250 Ma) to recent times (Eriksson and Altermann, 1998). These events are well preserved in the Transvaal Basin carbonates, where they occur as carbonate dissolution cavities at major unconformities and contacts within different stratigraphic units (Eriksson et al., 1995; Martini et al., 1995; De Bruyn and Bell, 2001). Subsidence is also common above cavities that develop as a result of pillar or beam failure in old abandoned coal mines, which, in some instances, may occur as water-filled subsidence, especially where the cavity breaks through to the surface, or the colliery roof has collapsed into mined-out zones (Van Schoor and Fourie, 2015).

Geophysical methods have been successfully applied in the mitigation of these hazards, by locating and delineating potential zones where cavities produced by the collapse of roofs into mine workings or sinkholes may exist (e.g. Butler, 1984; Miller and Steeples, 1991; Zhou et al., 2002). The significant contrasts in physical

properties (e.g., density, conductivity, velocity) usually exhibited by these cavities with the surrounding rocks, make the application of geophysical methods suitable for their delineation. However, methods need to be tested and adapted to local conditions, since every geophysical method has its limitations. Geophysical methods, including gravity, electrical resistivity, ground penetrating (GPR), and airborne thermal imaging methods (e.g. Breytenbach and Bosch, 2011; Van Schoor, 2002; Van Schoor and Fourie, 2015) have been locally tested in the past. Among all these geophysical techniques, the gravity method had the most success and is still widely used to delineate potential subsidence zones, especially in dolomitic terrain. However, gravity survey results often suffer from ambiguity, while the application of the technique is complicated by the selection of the appropriate survey grid size that can accurately delineate a wide range of sizes of near-surface voids (Van Schoor, 2002).

The seismic reflection technique has been applied effectively worldwide to investigate near-surface subsidence and sinkhole features. Several subsurface investigations of cavities related to sinkholes and subsidence using seismic reflection techniques have been documented. For example, Steeples et al. (1986) were able to delineate sinkholes produced by the dissolution of salt along a highway in Kansas City using seismic reflection, where subsidence associated with sinkhole formation has resulted in the rebuilding of the highway. The technique has also been used to map the voids created by mining of coal in regions where abandoned coal mines are located, as well as to investigate coal-related subsidence features (e.g. Branham and Steeples, 1988; Miller et al., 2005; Miller and Millahn, 2006; Zhou et al., 2015). The application of the seismic

reflection technique for investigating near-surface voids and cavities is based on the high acoustic impedance contrast that exists between the voids and the surrounding rocks. Characteristic disruption or distortion of bedding planes, abrupt termination of layers, and collapse structures are some of the prominent features commonly associated with sinkholes and subsidence zones. These features can be effectively imaged using the seismic reflection technique (Miller et al., 2005).

This study is a preliminary high-resolution seismic reflection investigation conducted at coal mine sites located in the Benoni area (Fig. 3.1a), near Johannesburg, and Springlake Colliery mines, near the town of Dundee in Kwazulu-Natal (Fig. 3.1b), South Africa. The coal mine site in the Benoni area is one of several abandoned coal mine sites that are being considered for industrial and commercial development. Coal was reported to have been mined within the vicinity of this area in the early 1930s, using the room and pillar method. However, there are no mine records or plans that show the extent and depth of the coal workings in the area. Recent evidence of subsidence-related events (e.g. water-filled subsidence, leaning structures, and sinkholes) are common in the study area, especially in the undermined area. These may have resulted from the collapse of the colliery roof into the mined-out zones (Fig. 3.2). An initial geotechnical investigation conducted in the area through percussion drilling also revealed the existence of weathered bands of dolomite beneath the coal-bearing strata, thereby raising concerns over the potential development of dolomite-related sinkholes or subsidence.

Similarly, the Springlake Colliery mine in the town of Dundee (Fig. 3.1b) is an old coal mine that is currently operated by Shanduka Group. Like the Benoni area, the room and pillar method was used for coal mining in the area in the past. Meanwhile, lack of adequate records of previous mining plans has made it difficult to ascertain the extent of the coal mining in some parts of the mine. Infrastructural expansion within the Springlake Colliery mine area has also been hampered by the lack of mine records. The available mine plans show known mined-out zones. However, there are suggestions that mining activities had extended beyond these established zones. The suspected areas have also been avoided for any infrastructural development, due to vulnerability to subsidence or sinkhole formation that may cause the failure of surface engineering structures. This preliminary study is therefore aimed at using high-resolution seismic reflection method to investigate subsidence- and sinkhole-related features in these two sites.

## 3.2 Location and geology

### 3.2.1 Case study 1 (Benoni Area)

The abandoned coal mine is situated within the Benoni Agricultural Holdings, which is located east of Johannesburg, and forms part of the Ekurhuleni Metropolitan Municipality in the Gauteng province of South Africa (Fig. 3.1a). According to the regional geological map (Fig. 3.1a), the study area is underlain by two major lithostratigraphic groups, the Karoo and the Transvaal Supergroups. The Karoo Supergroup rocks are younger (Late Carboniferous-Early Jurassic) and

are deposited on the Transvaal Supergroup (Archean-Proterozoic). In the study area, the Karoo Supergroup is made up of the Dwyka Group and the Ecca Group. The Dwyka Group, which is the oldest unit of the Karoo Supergroup (Johnson et al., 1996), occurs towards the east and northwestern part of the area, while the Ecca Group, represented by the Vryheid Formation, occurs in most part of the area.

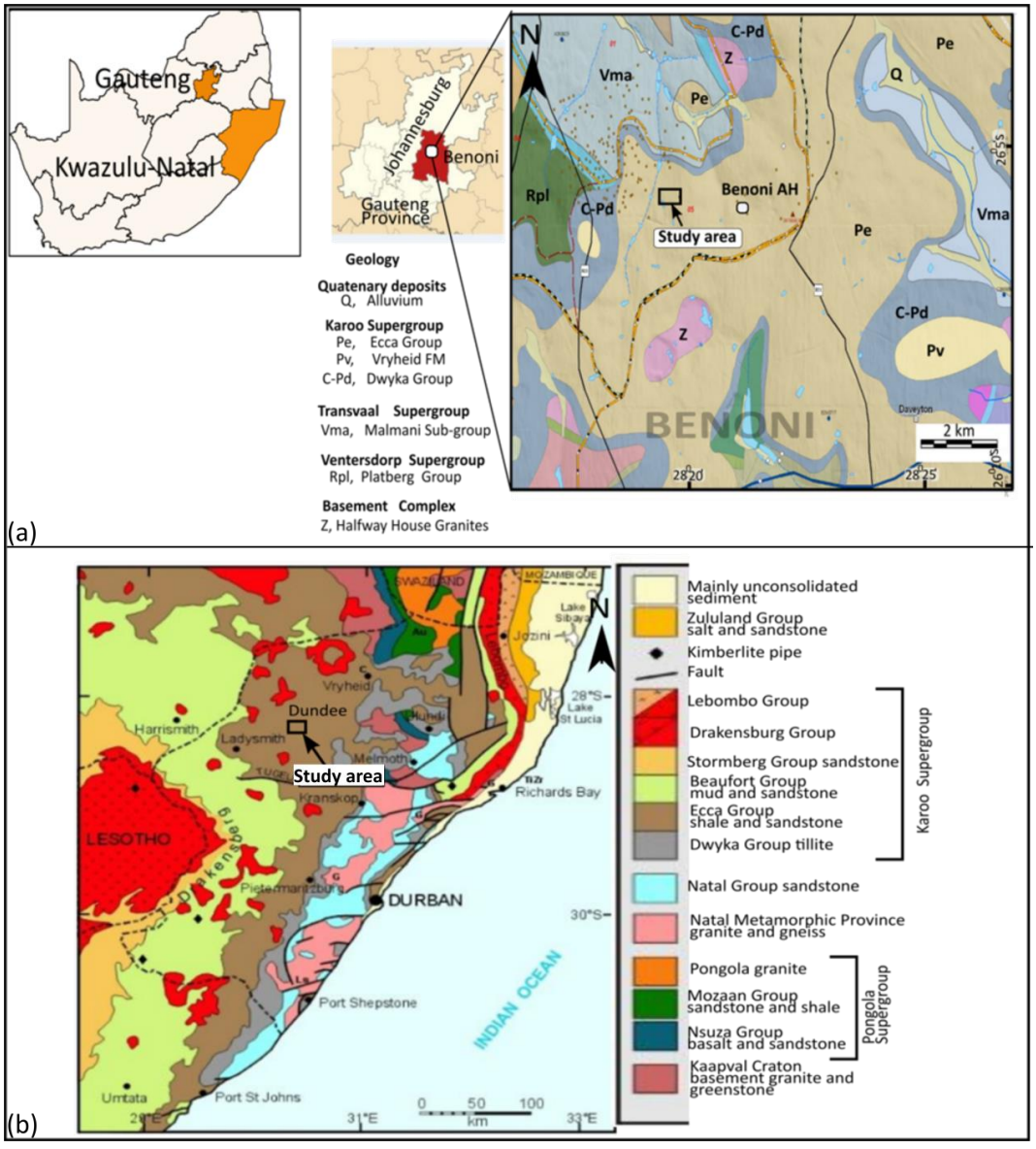



Figure 3.1: Location and regional geological map of Benoni (a) and Kwazulu-Natal (b) showing the two study areas (modified after Department of Water and Sanitation, 2009; Council for Geosciences, 2001).




Figure 3.2: Surface evidence of recent subsidence-related events at Benoni area. (a) Water-filled subsidence (b) Abandoned leaning structure caused by subsidence (c) Sinkholes caused by the collapse of the colliery roof into mined-out zone (d) A recently formed sinkhole.

The Transvaal Supergroup in the area is represented by the Malmani Subgroup of the Chuniespoort Group (Eriksson and Reczko, 1995), and occurs towards the east and northwestern part. The Malmani Subgroup is dominantly made up of dolomite and consists of five formations which are differentiated on the basis of chert content, stromatolite types, interbedded subordinate carbonaceous mudrocks, and rare quartzitic lithologies (Button, 1973). The Dwyka Group consists of various rock types that reflect glacial or glacial-related origin such as diamictite, conglomerate, fluvio-glacial pebbly sandstone, rhythmite and mudrock with dropstones (Johnson et al., 1996). The Ecca Group is made up of dark-colored

shales with interspersed siltstones and sandstones, and occasional coal seams, deposited subaqueously under reducing conditions in marine, deltaic and fluvial environments (Johnson et al., 1996), while the Vryheid Formation consists mainly of light grey sandstones. Minor igneous intrusions, in the form of dolerite sills or dykes, and Quaternary deposits (such as alluvium, sand and gravel) also occur in the study area.

The local geology of the study area is well known to the depth of 40 m, based on the geotechnical investigation that was previously conducted by Bear GeoConsultants (2012). The geotechnical investigation utilized percussion drilling to determine the undermined areas around the abandoned mine. One of the objectives of the investigation was to determine the depth at which the undermining had taken place, since there are no records to establish the extent of the coal workings. Four percussion holes, including three boreholes in the south and one in the north of the area (Fig. 3.3a), were drilled during the investigation. Coal seams were encountered in boreholes BH003, BH001, and BH002 (Fig. 3.3b) at the depth of 6, 7 and 13 m below the surface, respectively. The coal seam is about 7 m thick, and deepens towards the west of the area as shown by the stratigraphic correlation among the boreholes (Fig. 3.3b). Meanwhile, borehole BH004 in the north did not intersect any coal. Instead, it encountered an intrusive doleritic rock at the depth of 17 m (Fig. 3.3b).

Dolomites of the Transvaal Supergroup were also encountered in BH001 and BH003 at depths of 25 m and 29 m respectively. The intrusive doleritic rock encountered in borehole BH004 in the north is thick (~10 m) and competent. Meanwhile, it is difficult to ascertain if this doleritic rock occurs as a dyke or as a

sill in the area, as the borehole was terminated within the intrusive rock at 27 m below the surface. However, if the intrusive doleritic rock occurs as a sill, there is likelihood that dolomite may exist below it as well. The geotechnical investigation also revealed anomalous zones of high drilling rate within the dolomite formation encountered in BH001 and BH003, and were interpreted as weathered or karst zones which may have been subsequently filled with less dense materials. The presence of these karst zones could give rise to potential development of sinkholes or subsidence, especially if the water table is significantly lowered.

### 3.2.2 Case study 2 (Springlake Colliery mine)

The Springlake Colliery is located in the town of Dundee in Kwazulu-Natal province of South Africa (Fig. 3.1b). The regional geology of the area is similar to Benoni area, and dominantly underlain by the Ecca Group of the Karoo Supergroup. The local geology is revealed by the three exploration boreholes (BHL39, BHL40 and BHL42) that were drilled in the area, and consists of dolerite sills, sandstones, carbonaceous shale, and coal (Fig. 3.4). The boreholes only show the subsurface stratigraphy from the depth of 22 m to approximately 57 m, and include the dolerite sill, whose top is intersected at depths between 22 and 28 m, followed by interbedded sandstones and carbonaceous shale. The coal seams were encountered at depths between 47 and 56 m (Fig 3.4b).

## 3.3 Seismic data acquisition

High-resolution seismic reflection data were acquired with the aid of a 24-channel Geometric Geode in the two study areas, with an energy source provided by a 7

kg sledge hammer striking an aluminum plate. In order to enhance the quality of the signal, a vertical stacking of four shots per station was used in both surveys.

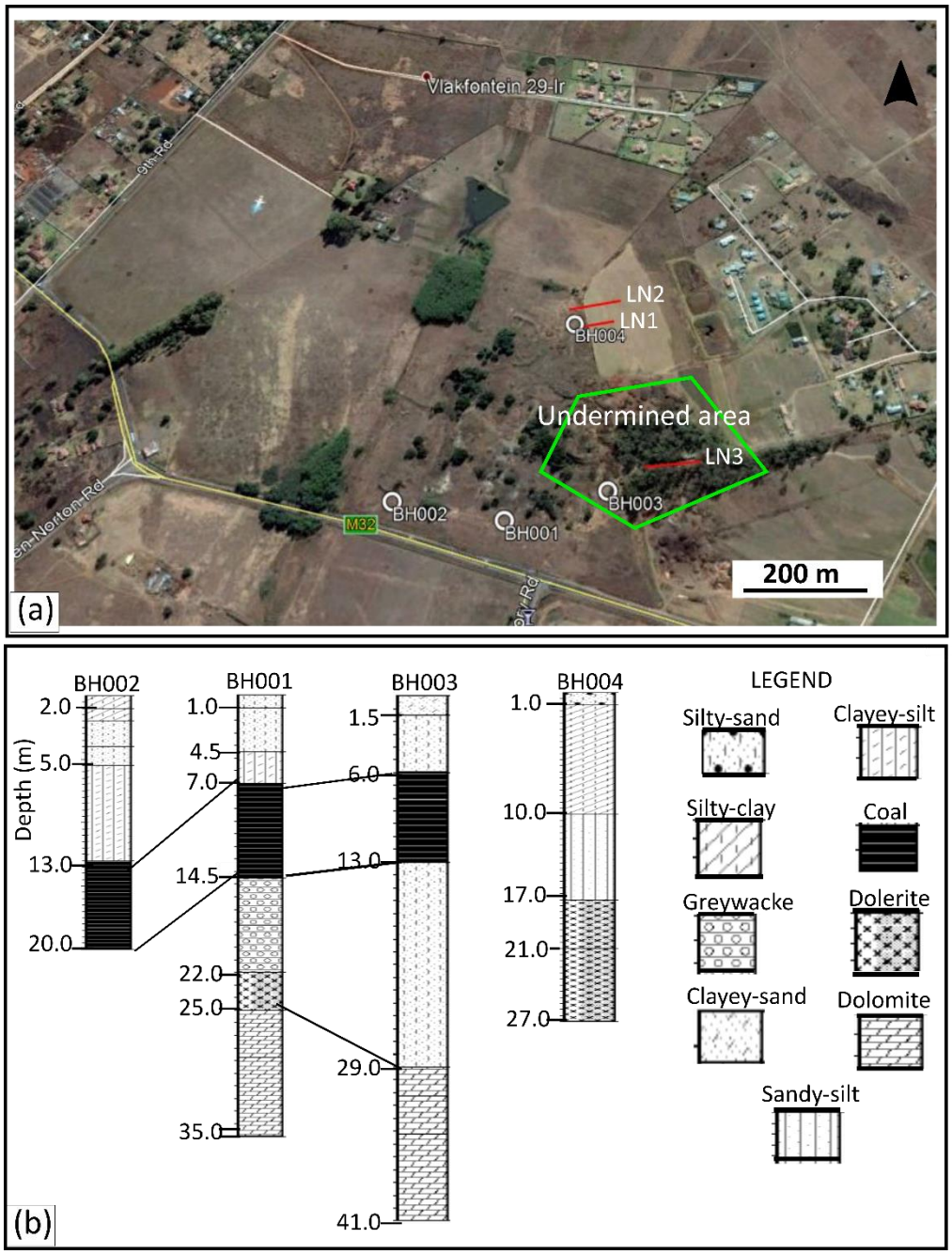



Figure 3.3: (a) Satellite image of Benoni study area showing the location of the boreholes and the seismic lines acquired in the area. (b) The stratigraphical correlation of the geology encountered in the boreholes shows that the coal seam deepens towards the west of the study area. Note the undermined area within the polygon.

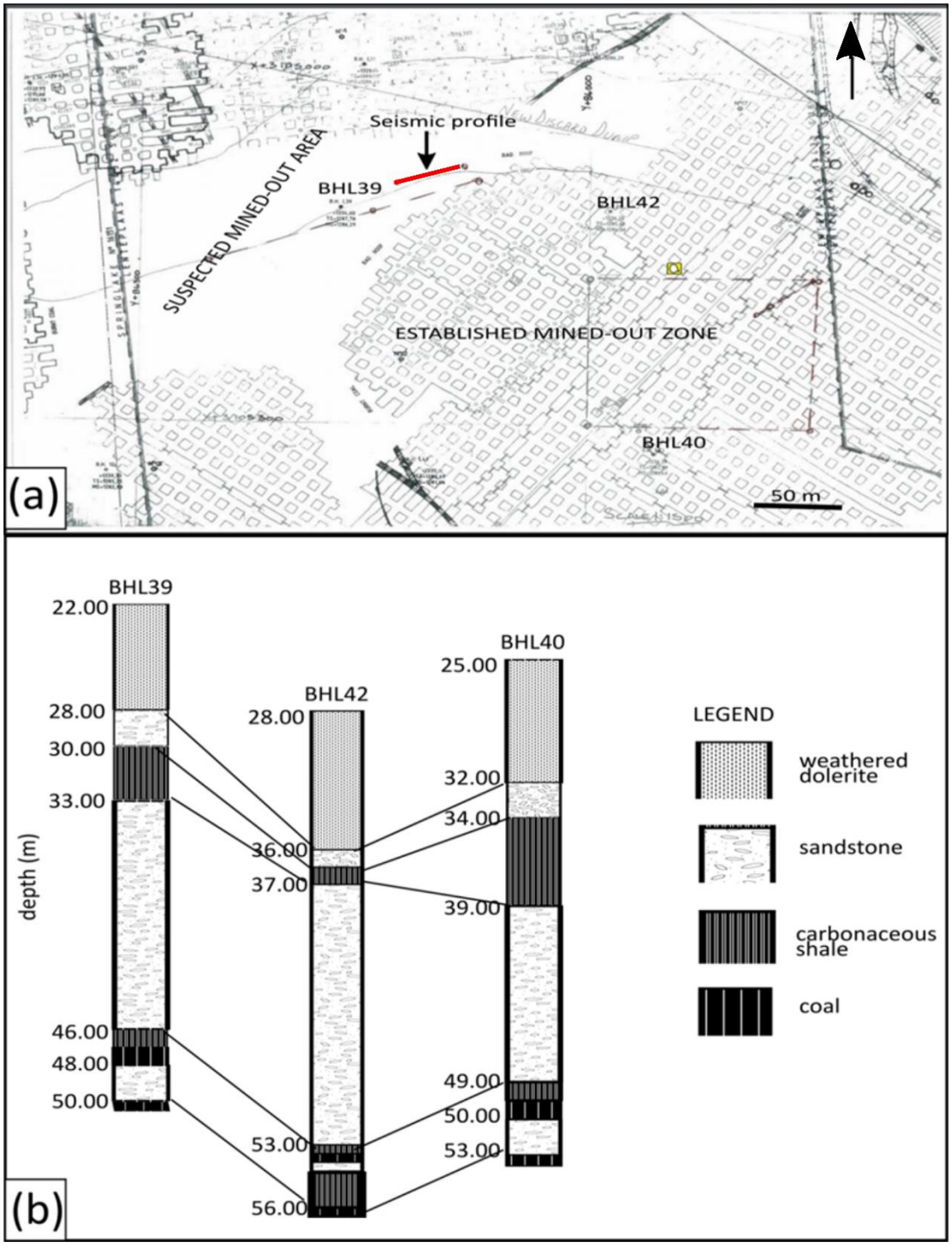



Figure 3.4: (a) Underground mine plan of the Springlake mine showing the seismic profile acquired across the suspected mined-out zone. (b) Boreholes from the Springlake mine showing the subsurface stratigraphy.

In the Benoni area, three types of vertical geophone with different resonance frequencies were deployed during the seismic data acquisition, and include 100 Hz, 48 Hz, and 14 Hz geophones. Three seismic lines, LN1, LN2 and LN3, were acquired in the area (Fig. 3.3a). Two of the seismic lines, LN1 and LN2, were acquired in the north of the study area, outside the undermined area. The objectives were to determine if the intrusive doleritic rock encountered in the borehole BH004 was a dyke or an extensive sill, and to map subsurface voids that may exist between the dolerite/limestone boundary, knowing that the rate of karstification is enhanced along stratigraphical boundaries within the Karoo Basin.

The third seismic line, LN3, was acquired along borehole BH003, adjacent to the leaning structure within the undermined area (Fig. 3.5). The objective was to delineate subsurface subsidence- and sinkhole-related features that may occur below the profile. The acquisition geometry along each of the profiles was similar with shot and geophone spacing of 2 m. The two geophone types of 48 and 100 Hz were utilized for the data acquisition along LN1, with the objective of comparing their resolution. Meanwhile, to obtain an appreciable fold of coverage and a significant profile length, the 48-channel 14 Hz geophone type was employed for the data acquisition along LN2 and LN3. The acquisition geometry was the same for the two geophone types along the profile LN1, with each spread consisting of 24 geophones per spread, and a minimum and maximum offset of 8 and 54 m respectively. Similarly, the acquisition geometry employed along profile LN2 and LN3 was the same, and consists of 48 geophones per spread and a minimum and maximum offset of 2 and 96 m respectively.




**Figure 3.5: A s**eismic line acquired adjacent to the abandoned leaning structure in the undermined area.

At the Springlake mine, one seismic profile was acquired outside the established mined-out area, where previous coal mining may have extended (Fig. 3.4a). The objective of selecting this area was to search for evidence that may confirm previous mining activities, such as subsurface voids and related subsidence. The seismic data were acquired along a 50 m long profile using the 14 Hz vertical geophone. This geophone type was selected because it consists of 48 geophone units that can provide appreciable fold of coverage as compare to other geophones with 24 units. The survey geometry in this area was carefully selected to avoid spatial aliasing due to geophone spacing (e.g. Liner, 2016). Therefore, the

geometry of the spread consists of 48 geophones that were spaced at 1 m, with a shot interval of 2 m. The summary of the parameters employed in the seismic data acquisition for both study areas is presented in Table 3.1.

Table 3.1: Seismic data acquisition parameters

| **Acquisition Parameters** | **Benoni area** | **Springlake mine** |
|---|---|---|
| Energy source type | Sledge hammer | Sledge hammer |
| Source weight | 7 kg | 7 kg |
| Geophone types | Vertical geophones (100 Hz, 48 Hz and 14 Hz), | 14 Hz vertical geophone |
| Seismograph | 2x Geometric Geode 24-channel | 2x Geometric Geode 24-channel |
| Geophone spacing | 2 m | 1 m |
| Shot spacing | 2 m | 2 m |
| Vertical stacking | 4 | 4 |
| Minimum offset | 8 m (LN1), 2 m (LN2 and LN3) | 2 |
| Maximum offset | 54 m (LN1), 96 m (LN2 and LN3) | 50 |
| Sampling rate | 0.25 ms | 0.25 ms |
| Record length | 500 ms | 1 s |
| Record format | SEG-2 | SEG-2 |

## 3.4 Seismic data processing

The processing of the seismic data was carried out with using the ReflexW seismic data processing package. Similar processing sequence was used for all the datasets acquired in the two study areas. The summary of the data processing sequence is presented in Table 3.7. The seismic data acquired in both study areas generally show high signal-to-noise ratio, with visible reflection and the first break refraction events in the pre-stack shot gathers (Fig. 3.6). Preliminary processing, including trace editing, reverse polarity correction and frequency

filtering, was applied to the seismic datasets. Noisy and dead traces resulting from bad geophone coupling and non-responsive geophone channels were removed from the datasets (Fig. 3.6a). Signal duplication caused by the reverberation of the base-plate is observed below approximately 200 ms in some of the datasets (3.6b). Hence, a time cut at 200 ms was applied to cancel the effect of these false signals on subsequent data processing (3.6c).

The frequency spectrum for the whole dataset acquired along each of the seismic lines is compared in Figure 3.7a-e. The datasets acquired along each line in the Benoni area show similar dominant frequency of approximately 100 Hz (Fig. 3.7a-d), while the Springlake datasets are dominated by frequency of approximately 45 Hz (Fig. 3.7e). Spectral analysis using the Fourier Transform was conducted on some selected traces along each of the seismic lines (Fig. 3.8). The aim was to determine the frequency components of the different seismic events observed in the raw data for subsequent frequency filtering.

The surface waves are generally characterized by large amplitude, and can be interpreted in the amplitude spectra to be associated with the largest amplitudes occurring at the low frequencies (Fig. 3.8), while the reflection signals are expected to be the dominant events at high frequencies. The amplitude spectra obtained for selective traces from the Benoni datasets generally show the largest amplitude below approximately 80 to 100 Hz (Fig. 3.8a), while the Springlake datasets show the frequencies corresponding to the surface waves to occur below approximately 65 Hz (Fig. 3.8b). Therefore, in order to suppress the surface waves and the high frequency random noise from the seismic data, a Butterworth bandpass filter of 85-250 Hz was generally applied to the Benoni datasets (Fig

3.9), while a Butterworth bandpass filter of 65-200 Hz was applied to the Springlake datasets.

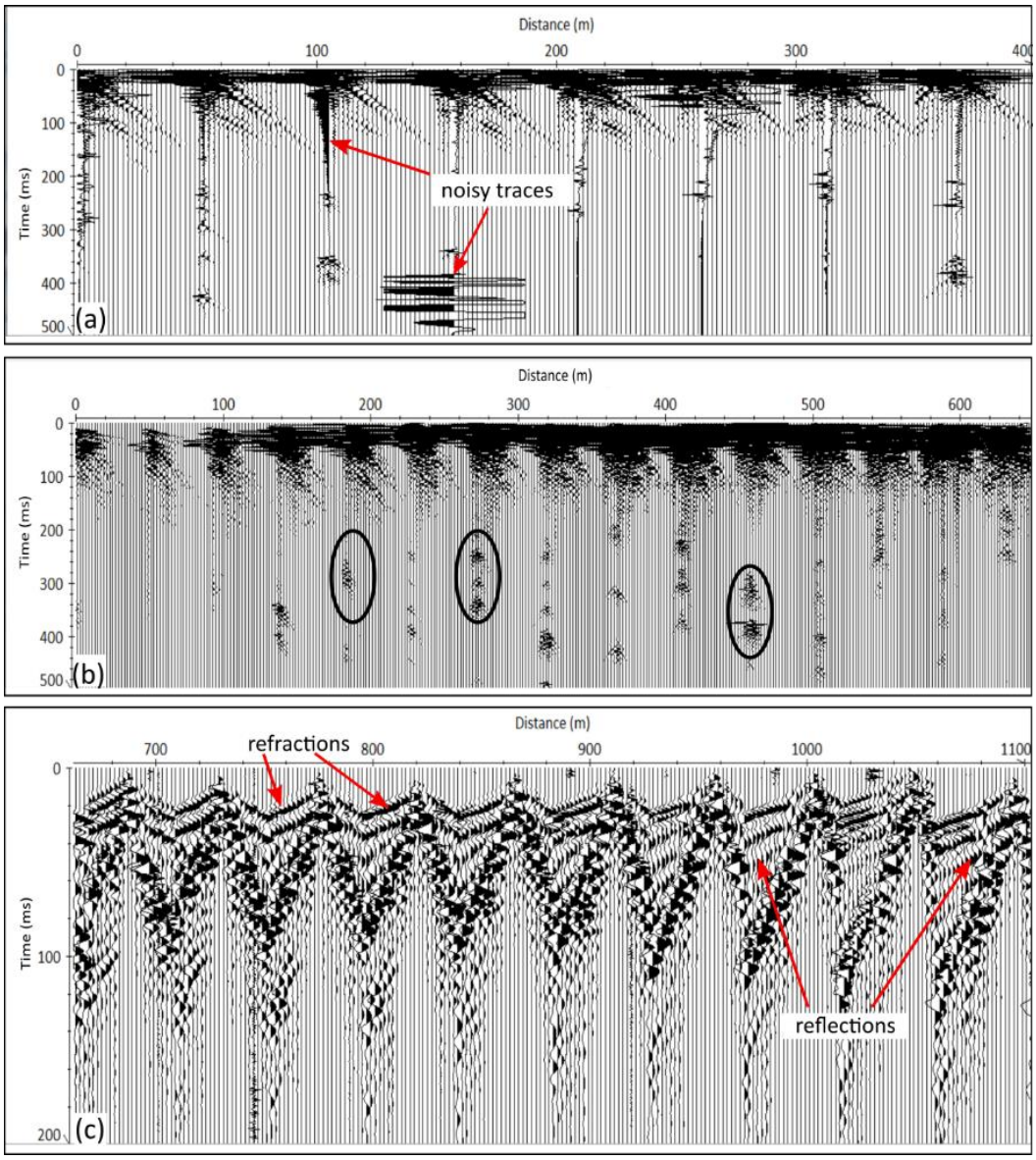



Figure 3.6: Trace editing (a) Raw shot gathers before trace editing and (b) after trace editing. Note the signal duplication due to reverberation of the base plate in the circled region below 200 ms. (c) Typical shot gathers from outside the undermined area showing the data after time-cut, with trace normalized gain applied for display. Note the reflection and refraction events in the raw shot gathers.

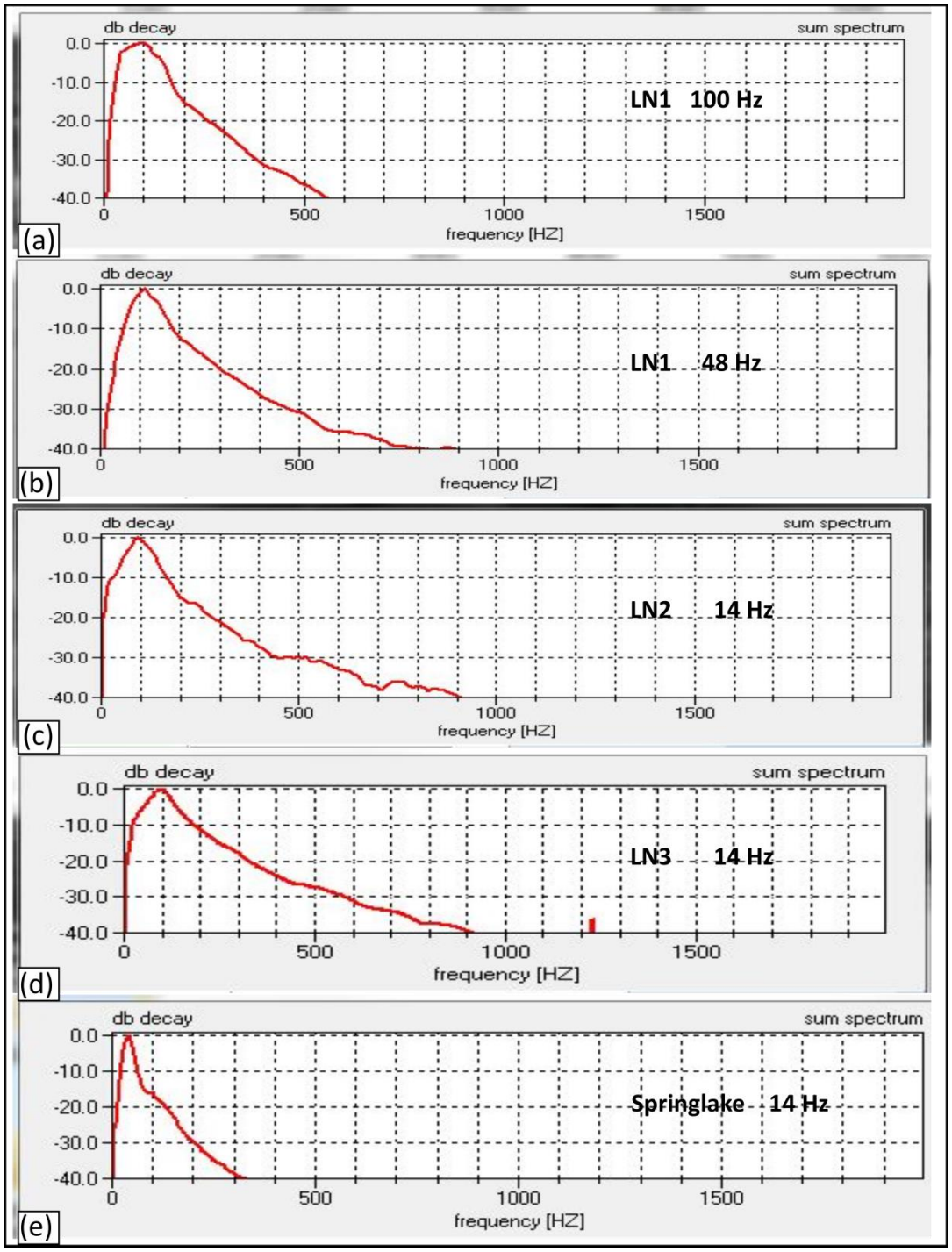



Figure 3.7: Frequency spectrum of the whole dataset acquired along each of the seismic lines. (a) LN1 using the 100 Hz geophone type, (b) LN1 using the 48 Hz geophone type, (c) LN2 using 14 Hz geophone type, (d) LN3 using 14 Hz geophone type, and (e) Springlake using 14 Hz geophone type.

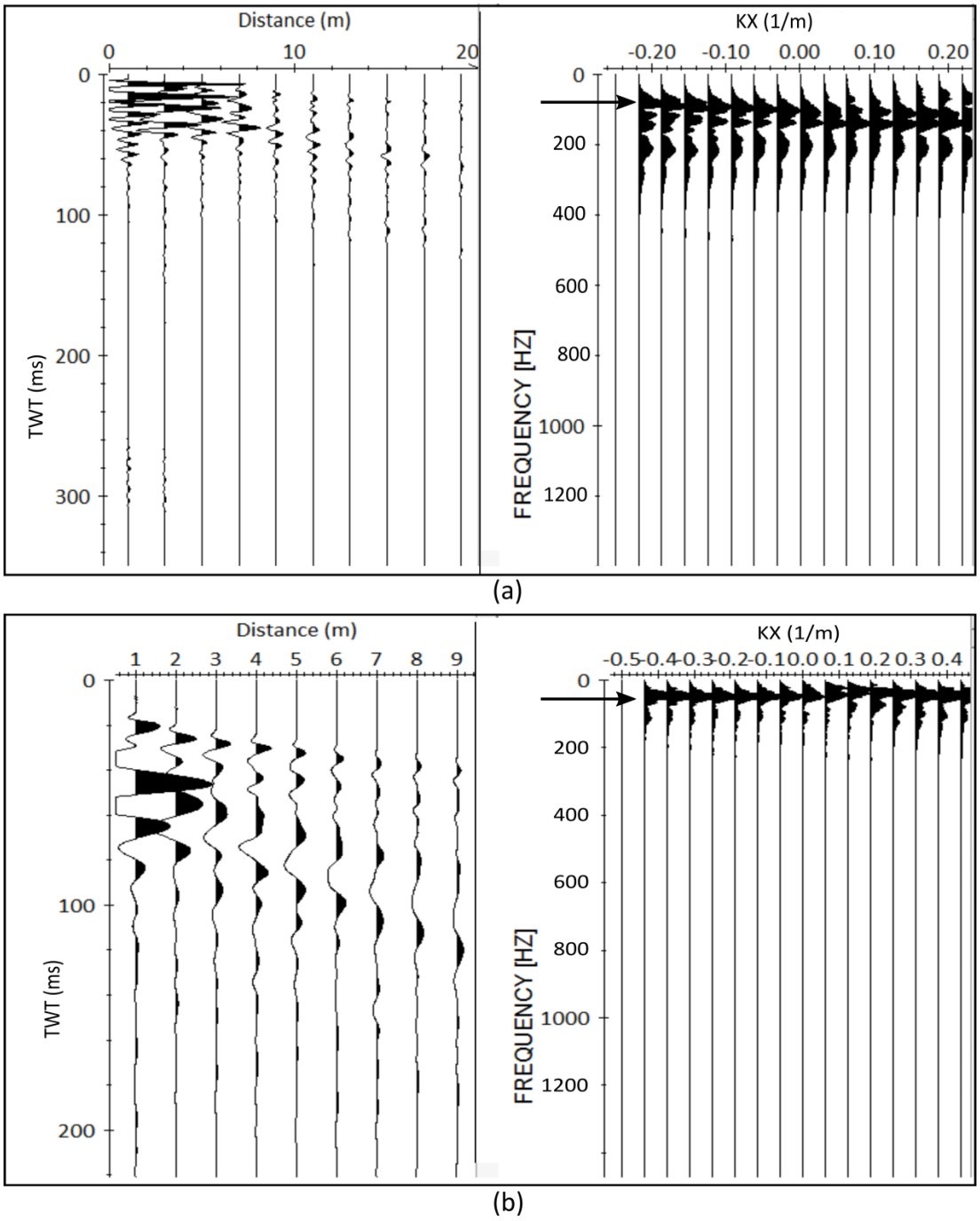



Figure 3.8: Selected traces and the corresponding amplitude spectra for (a) the Benoni datasets and (b) the Springlake datasets. The arrow indicates the largest amplitude corresponding to the frequencies of the surface waves.

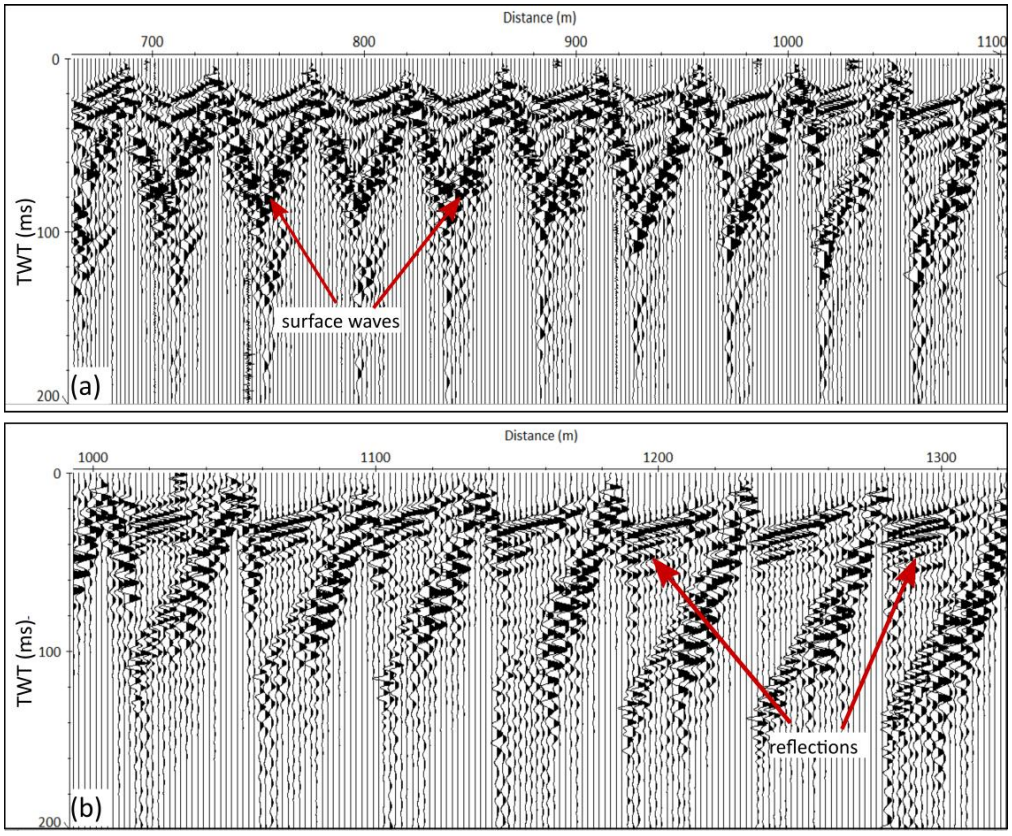



Figure 3.9: Pre-stack shot gathers (a) before and (b) after applying a Butterworth bandpass filter of 85-250 Hz. Note the suppression of the ground-rolls (surface waves) and the enhancement of the reflection events.

The pre-stack frequency filtering was followed by the muting of the surface waves that occur in the form of airwaves, which was done by applying a surgical bottom mute at apparent velocity of 330 m/s (Fig. 3.10). Meanwhile, refraction muting was not applied to the datasets. This is to avoid degrading the quality of the reflection signals from the near shallow reflectors that might be masked by the refracted events. Static correction using the intercept method was applied to the datasets before stacking. The two study areas are generally flat, with no significant undulation in topography. Therefore, the elevation static correction was not necessary, and the delay-time due to the weathered layer was the only static correction applied to the datasets. In order to determine the time-shift

applicable for the static correction, refraction analysis, using the intercept method, was conducted at selected shots along the profiles. The results of the refraction analysis are presented in Table 3.2-3.6, with the Benoni datasets showing considerable variation in the delay-time correction and thickness of the weathered layer obtained for the datasets acquired within and outside the undermined area.

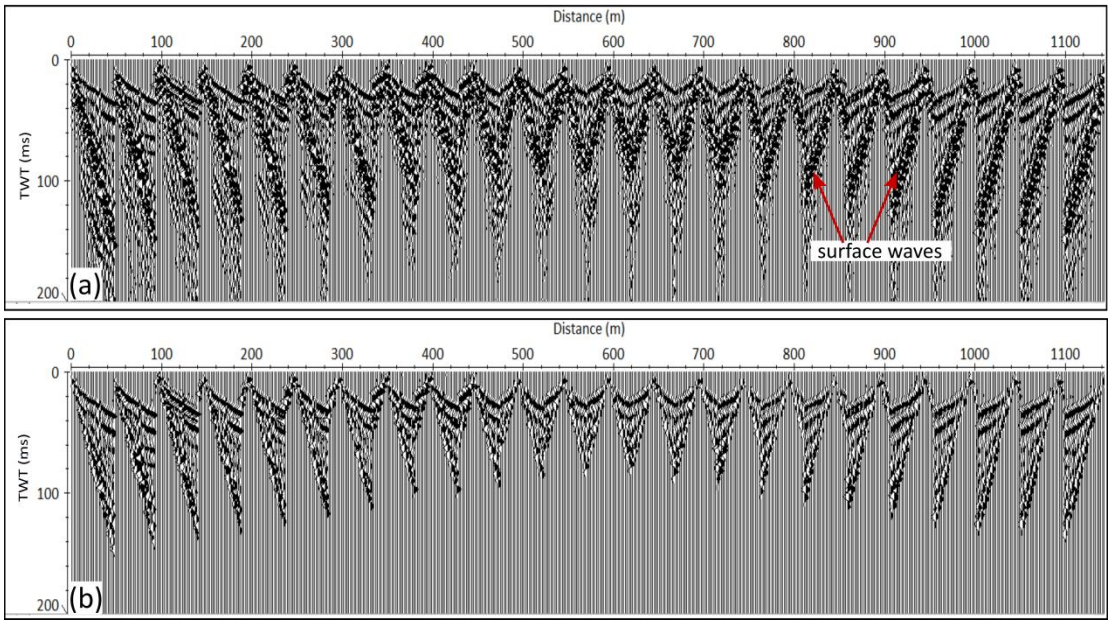



Figure 3.10: Pre-stack shot gathers before (a) and after surgical muting (b). Note the muting of the surface waves that occur in the form of air waves.

Table 3.2: Refraction static analysis along LN1 (100 Hz geophone)

| Shot station | Velocity of the weathered layer (m/s) | Weathered layer thickness (m) | Time-shift applied (ms) |
|---|---|---|---|
| 8 | 952 | 2.94 | 6.18 |
| 20 | 1000 | 3.62 | 7.24 |
| 34 | 696 | 3.03 | 6.82 |
| 42 | 960 | 4.29 | 8.94 |
| 54 | 884 | 2.74 | 6.20 |

Table 3.3: Refraction static analysis along LN1 (48 Hz geophone)

| Shot station | Velocity of the weathered layer (m/s) | Weathered layer thickness (m) | Time-shift applied (ms) |
|---|---|---|---|
| 8 | 909 | 2.57 | 5.70 |
| 20 | 975 | 3.92 | 8.00 |
| 34 | 769 | 2.8 | 7.30 |
| 44 | 908 | 3.83 | 7.50 |
| 54 | 1067 | 3.05 | 5.71 |

Table 3.4: Refraction static analysis along LN2

| Shot station | Velocity of the weathered layer (m/s) | Weathered layer thickness (m) | Time-shift applied (ms) |
|---|---|---|---|
| 0 | 667 | 3.67 | 11.01 |
| 12 | 731 | 2.81 | 7.69 |
| 24 | 820 | 4.55 | 11.10 |
| 36 | 739 | 3.25 | 8.80 |
| 48 | 667 | 4.63 | 13.88 |
| 60 | 808 | 3.79 | 9.38 |
| 72 | 661 | 3.57 | 10.80 |
| 84 | 853 | 3.94 | 9.24 |
| 96 | 667 | 4.87 | 14.60 |

Table 3.5: Refraction static analysis along LN3

| Shot station | Velocity of the weathered layer (m/s) | Weathered layer thickness (m) | Time-shift applied (ms) |
|---|---|---|---|
| 1 | 725 | 13.87 | 38.37 |
| 13 | 612 | 10.50 | 34.31 |
| 27 | 589 | 11.81 | 40.10 |
| 43 | 569 | 9.78 | 34.38 |
| 55 | 597 | 11.00 | 38.13 |
| 71 | 564 | 10.86 | 38.51 |
| 83 | 788 | 16.72 | 42.44 |
| 95 | 626 | 12.27 | 39.20 |

Table 3.6: Refraction static analysis along the Springlake profile

| Shot station | Velocity of the weathered layer (m/s) | Weathered layer thickness (m) | Time-shift applied (ms) |
|---|---|---|---|
| 0 | 391 | 5.50 | 28.13 |
| 8 | 468 | 5.10 | 21.80 |
| 18 | 458 | 5.04 | 21.83 |
| 28 | 395 | 4.40 | 23.28 |
| 38 | 439 | 3.70 | 16.86 |
| 50 | 436 | 4.70 | 21.56 |

The static correction was subsequently followed by the normal move-out (NMO) correction and the stacking of the datasets, which were simultaneously carried out in the common mid-point (CMP) domain. Prior to the stacking of the seismic datasets, velocity analysis, using the constant velocity stacking (CVS) method (Baker, 1999; Yilmaz, 2001), was conducted to determine the optimum 2D velocity model that would adequately flatten the hyperbolas and stack the traces. The CVS method was chosen for the velocity analysis because it allows the faster picking of stacking velocities that produce the best stack from series of interactive velocity panels. However, the CVS method usually requires initial minimum and maximum boundaries of the NMO velocities to generate a series of velocity panels at constant velocity intervals. A 2D velocity model, which is obtained by selecting the velocity values that best fit the hyperbolas from these velocity panels, is subsequently used for the NMO correction and the stacking of the traces. In order to estimate the minimum and maximum velocity boundaries that would be used to generate the CVS panels, hyperbola fitting was conducted directly on the reflection events observed in some selected CMP gathers, which generally indicated a NMO velocity range of 1100-2800 m/s. Therefore, a minimum and maximum velocity boundary of 1000 and 4000 m/s respectively

was used to generate a set of velocity panels at constant velocity increment of 500 m/s. The seismic datasets acquired in the two study areas were generally stacked at optimum stacking velocity range of 1800-2400 m/s (Fig. 3.11).

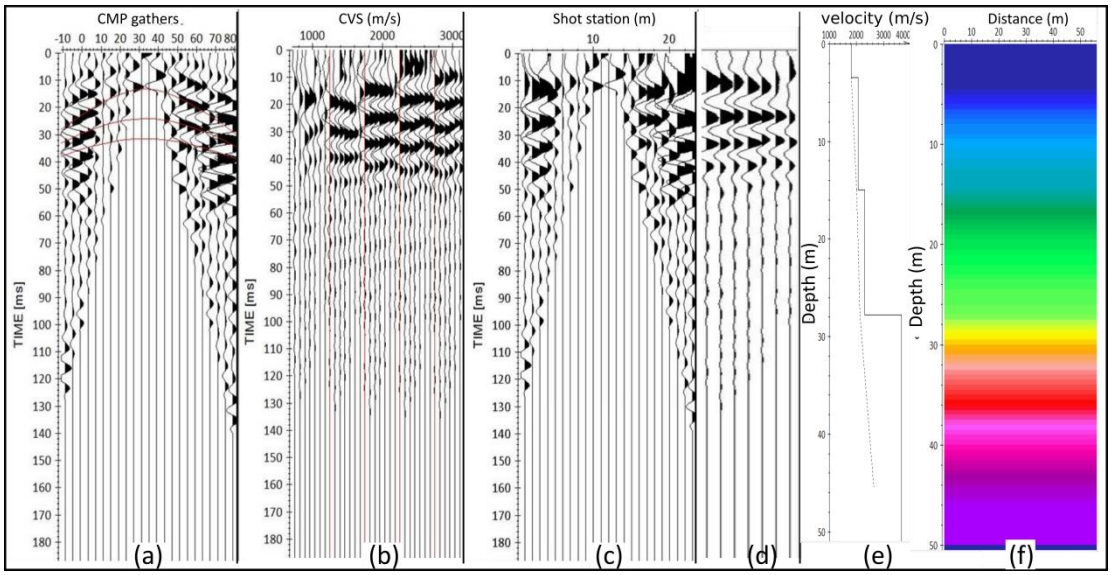



Figure 3.11: Illustration of the CVS analysis (a) Hyperbola fitting conducted on a CMP gather, (b) CVS panels generated using minimum and maximum velocity boundaries of 1000 and 4000 m/s, respectively at a constant velocity increment of 500 m/s, (c) An NMO corrected shot gather, (d) CMP stack displayed for 7 adjacent CMP gathers (e) 1-D velocity model picked from the CVS panels, and (d) The corresponding 2-D velocity model obtained from the stacking velocities that were picked from the CVS panels.

In order to improve the quality of the stacked sections, a post-stack, bandpass frequency filter was generally applied to eliminate some of the low frequency, coherently stacked ground-rolls, and high frequency noise that were observed in the stacked sections. Based on the spectral analysis of the stacked traces, the bandpass frequency filters of 85-95-140-160 Hz was applied to the stacked sections of the Benoni datasets obtained along LN1 (Fig. 3.12), while the bandpass frequency of 55-65-105-120 Hz, 65-75-130-150 Hz, and 55-65-95-105 Hz were applied to the stacked sections obtained along profile LN2, LN3, and the Springlake datasets respectively. The bandpass frequency filtering was

immediately followed by the migration of the stacked sections, which was done using the Kirchhoff migration method (Sheriff and Geldart, 1995) at a maximum dip and average medium velocity of 3.5 ms and 2000 m/s respectively. This was followed by the application of an automatic gain control (AGC) at 50 ms window length. Finally, the migrated data were time -to- depth converted using the 2D velocity model obtained from the CVS analysis.

Table 3.7: Seismic data processing sequence

| Processing Sequence | Description |
|---|---|
| 1 | Reformat from SEG-2 to ReflexW format |
| 2 | Trace editing (polarity check, removal of noisy and dead traces) |
| 3 | Butterworth bandpass filter to suppress the ground-rolls (85-250 Hz for the Benoni datasets and 65-200 Hz for the Springlake datasets) |
| 4 | Surgical bottom mute at 330 m/s apparent velocity (to eliminate air-waves) |
| 5 | Refraction static analysis |
| 6 | Refraction static correction |
| 7 | CMP sorting |
| 8 | Velocity analysis using constant velocity stacking method (CVS) |
| 9 | NMO analysis |
| 10 | NMO correction |
| 11 | Stacking |
| 12 | Post-stack bandpass frequency filtering |
| 13 | Migration (Kirchhoff's migration at 3.5 ms maximum dip and medium velocity of 2000 m/s) |
| 14 | AGC at 50 ms window length |
| 15 | Time-to-depth conversion |

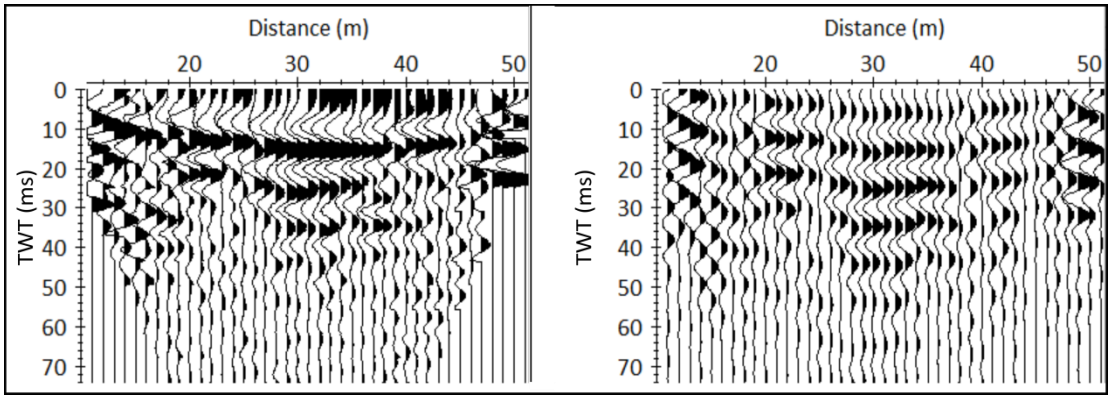



Figure 3.12: An example of a filtered stacked section obtained with the 48 Hz geophone along LN1 showing the stacked data before (left) and after (right) the application of a bandpass frequency of 85-95-140-160 Hz. Note the improvement in the resolution of the reflection events in the images on the right.

## 3.5 Numerical modeling

In order to aid the interpretation of the observed seismic sections, 2D synthetic stacked models, obtained using the forward modelling module in the ReflexW package, were used to verify some of the reflection events observed in the seismic sections. The 2D synthetic, zero offset seismograms were generated using the finite difference method, while the model parameters employed in the simulation were derived from the geological information encountered in BH003 and BH004 as presented in Table 3.8 and 3.9 respectively. The simulation of the synthetic seismograms was based on the horizontal layer model, with the assumption of an exploding reflector as the energy source. According to the synthetic models (Fig. 3.13), the top of the coal seam is predicted to occur at 11 ms two-way-time (TWT), while the top of the dolerite is predicted at 21 ms TWT. Meanwhile, it was not possible to generate synthetic stacked models from the Springlake boreholes, due to the missing geological information in the shallower part of the boreholes. However, another geophysical method, using the electrical resistivity

tomography (ERT) method, was conducted parallel to the profile to verify the anomalies observed in the Springlake seismic section.

Table 3.8: Model parameters for borehole BH003

| Layers | Depth (m) | P-wave (m/s) | Density (g/cm$^3$) |
|---|---|---|---|
| Silty-sand | 0-2 | 600 | 1.5 |
| Silty-clay | 2-6 | 1600 | 2.1 |
| Coal | 6-13 | 2000 | 1.3 |
| Silty-sand | 13-29 | 2200 | 2.3 |
| Dolomite | 29- ~ | 3500 | 2.8 |

Table 3.9: Model parameters for borehole BH004

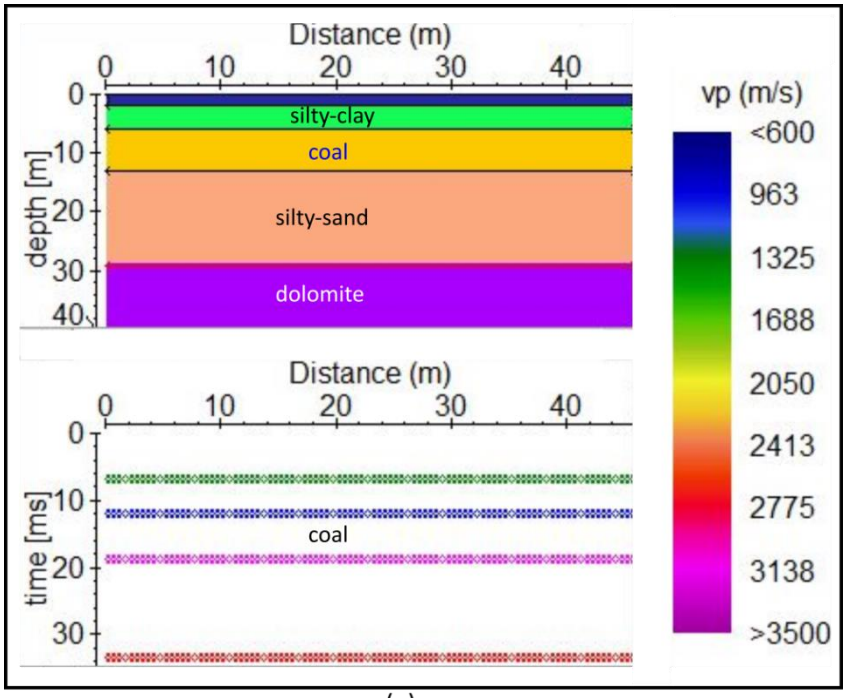
| Layers | Depth (m) | P-wave (m/s) | Density (g/cm$^3$) |
|---|---|---|---|
| Silty-sand | 0-3 | 900 | 1.9 |
| Silty-clay | 3-10 | 1650 | 2.1 |
| Sandy-silt | 10-17 | 2200 | 2.3 |
| Weathered dolerite | 17-21 | 2700 | 2.7 |
| Fresh dolerite | 21- ~ | 3200 | 2.9 |

## 3.6 Results and interpretation

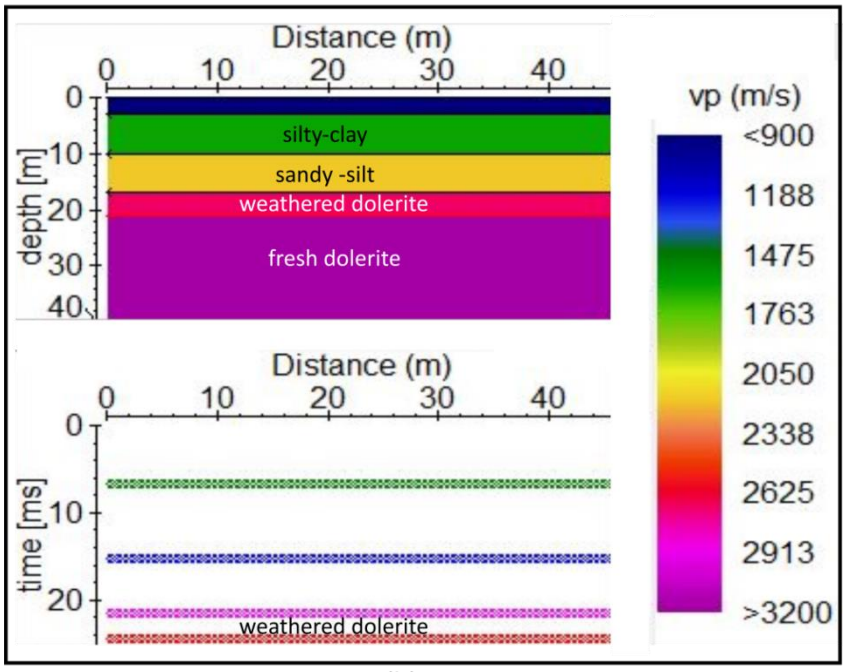
The seismic datasets acquired in the Benoni study area generally show a predominant signal frequency of approximately 100 Hz, which, in addition to the medium velocity, is an important factor that determines the resolution limit of a seismic dataset. Hence, the objective to resolve the coal seam and the dolerite layer in the study area will depend on the layer medium velocity and the dominant frequency recorded in the datasets. Based on the 1-D velocity model obtained from the CVS analysis (Fig. 3.11), the average medium velocity within the region occupied by the coal seam and the dolerite layer, is approximately 2000 and 2800 m/s respectively. If the Widess' minimum resolution criteria of a quarter

wavelength (Widess, 1973) is considered, the minimum thickness that can be resolved based on the 100 Hz dominant frequency is 5 m and 7 m for the coal seam and the dolerite layer, respectively. Therefore, based on the Widess' minimum resolution criteria, the thickness of the coal seam and the dolerite layer encountered in the boreholes are within the seismic resolution limit of the datasets.

The seismic datasets acquired along line LN1 with both geophone types (100 and 48 Hz) show high signal-to-noise ratio, with several reflection events that are visible in the pre-stack data (Fig. 3.13a, b, c). The seismic sections obtained for the two geophone types (100 and 48 Hz) along this line also display similar reflection events. The dolerite layer is shown as a strong continuous reflector on the seismic sections obtained for the two geophone types at approximately 21 ms TWT predicted by the synthetic model (Fig. 3.13d, e). Therefore, this may suggest that the dolerite layer along this profile occurs as a sill. Another continuous reflector is also observed immediately below the dolerite sill at approximately 31 ms, which corresponds to about 30 m in the depth migrated section (Fig. 3.14a, b). This reflector is interpreted to be the top of the underlying dolomite layer in the area, since dolomite is expected to be the dominant lithology at this depth based on the stratigraphy obtained from the boreholes. This implies that the dolerite layer in the north of the study area may reach up to about 13 m in thickness.




(a)




(b)

Figure 3.12: The depth sections with corresponding 2D synthetic seismograms for (a) Borehole BH003 showing the top of the coal seam at ~ 11 ms TWT, and (b) Borehole BH004 showing the top of the dolerite sill at ~ 21 ms TWT.

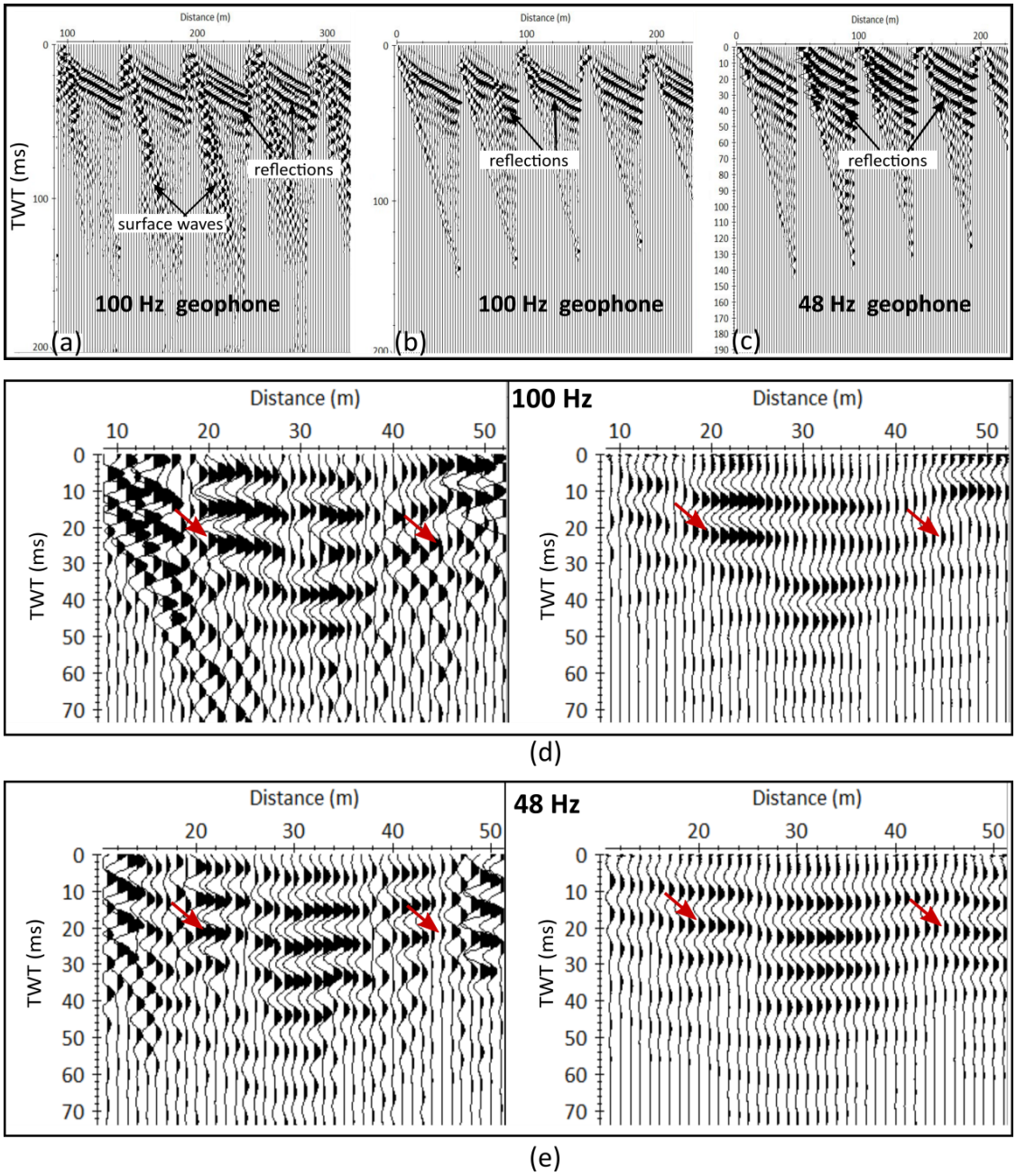



Figure 3.13: Pre-stack and the corresponding stacked sections obtained for the two geophone types along LN1. (a) Shot gathers from the 100 Hz geophone with visible reflection events after applying a bandpass Butterworth filter. Trace normalized gain is applied for display, (b) The same shot gathers from the 100 Hz geophone after applying a surgical bottom mute at 330 m/s. Note the muting of the surface air waves, (c) Shot gathers from the 48 Hz geophone showing visible reflection events after applying a bandpass Butterworth filter and a surgical bottom mute. Trace normalized gain is applied for display, (d) Stacked and the corresponding migrated section (without AGC) obtained with the 100 Hz geophone type, and (e) Stacked and the corresponding migrated section (without AGC) obtained with the 48 Hz geophone type. The top of the dolerite layer is indicated by the red arrow.

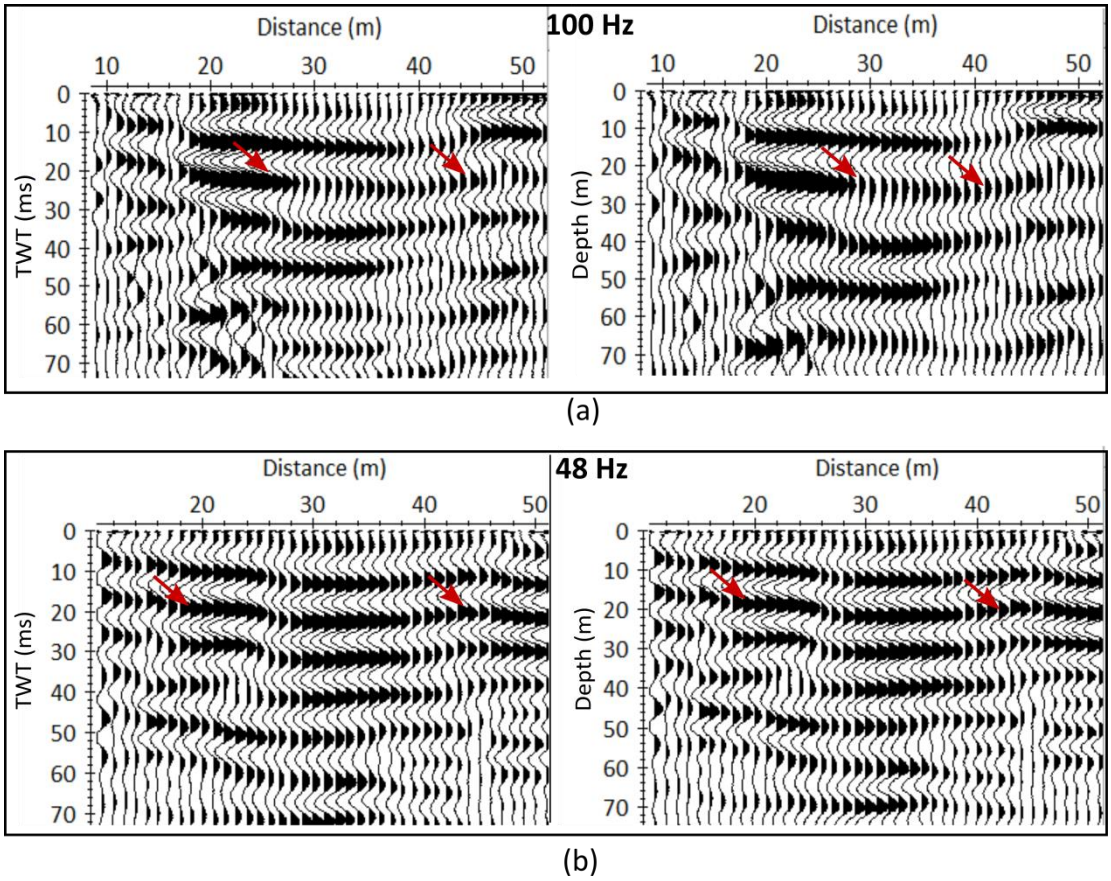



Figure 3.14: TWT migrated section (with AGC applied) and the corresponding depth sections obtained along LN1 (a) 100 Hz geophone type (b) 48 Hz geophone type. The arrow indicates the top of the dolerite layer.

Similarly, the datasets acquired along line LN2 show high quality data, with several visible reflection events in the pre-stack data after applying a bandpass filter (Fig. 3.15a). The extension of the dolerite layer below this profile is also confirmed by the strong continuous reflector that occurs at approximately 21 ms TWT on the stacked section (Fig. 3.15b). However, the dolerite layer exhibits variable geometry along this profile. The layer dips steeply from approximately 21 ms from the start of the profile to about 41 ms in the middle of the profile (corresponding to a dip magnitude of about 45° on the aspect ratio of 1:1) and shows as a near horizontal layer towards the end of the profile. Therefore, this

may suggest that the doleritic intrusion in this area exhibits a complex geometry, having the characteristics of sills and dykes. The strong reflector, suspected to be the dolomite layer underlying the doleritic layer, is also observed on the seismic section obtained along this profile at approximately 31 ms TWT (Fig. 3.15b, c).

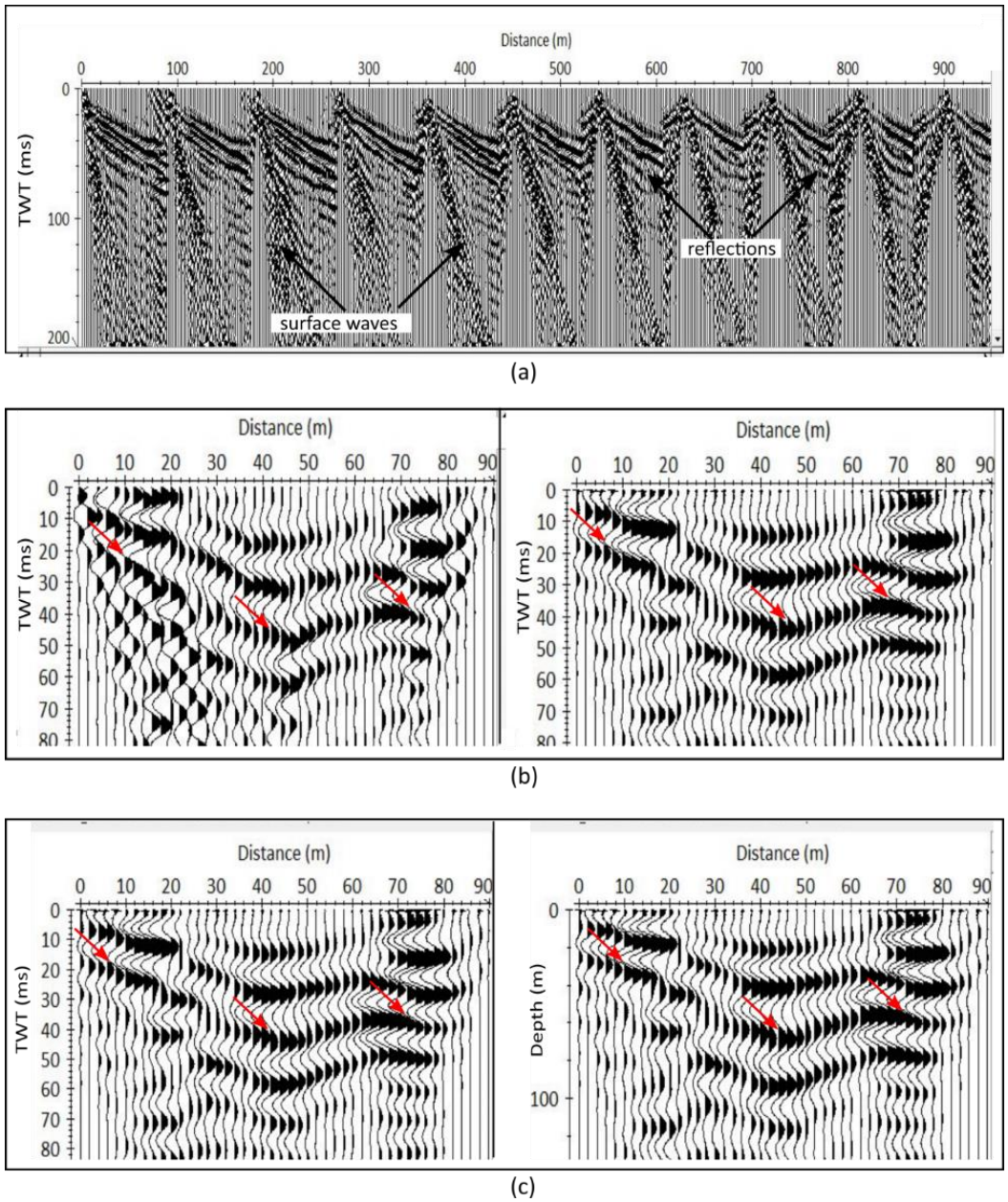



Figure 3.15: (a) Pre-stack shot gathers along LN2 showing visible reflection events after applying a bandpass Butterworth filter. Trace normalized gain is applied for display, (b) Stack and the corresponding time migrated section along LN2 with AGC applied, and (C) Time migrated (with AGC applied) and the corresponding depth section along LN2. The arrow indicates the top of the dolerite layer. Note the dipping of the dolerite layer from approximately 21 ms to about 41 ms.

The datasets acquired along the seismic line LN3, in the undermined area, also show several reflection events after applying a bandpass Butterworth filter, especially in the far offset shot gathers (Fig. 3.16a). The coal seam zone is identified by its characteristic coherent negative reflection amplitude on the seismic section obtained along this line (Fig. 3.16b), and occurs at approximately 11 ms TWT, which is similar to the TWT predicted by the synthetic model. Similarly, the room and pillar technique employed during the coal mining in the area can be deduced from the presence or absence of coherent reflection events from the coal seam, as observed in the migrated section (Fig. 3.16c). The region containing coherent negative reflection events from the coal seam probably corresponds to the un-mined pillars that were left behind to support the colliery roof, while the region with incoherent reflection events probably corresponds to the mined-out zones (Fig. 3.13c) that may have been filled with overburden sediments.

Alternating zones of chaotic reflections are also observed on the stacked seismic section along LN3 (Fig. 3.16b), and may have been caused by scattered and diffracted events emanating from voids or cavities that probably exist in the area. In the improved migrated section, these alternating chaotic reflection zones are seen to be devoid of reflection events, which may further suggest they are dissolution cavities that developed within the underlying dolomite rock at the depth of approximately 50 m below the profile (Fig. 3.16c).

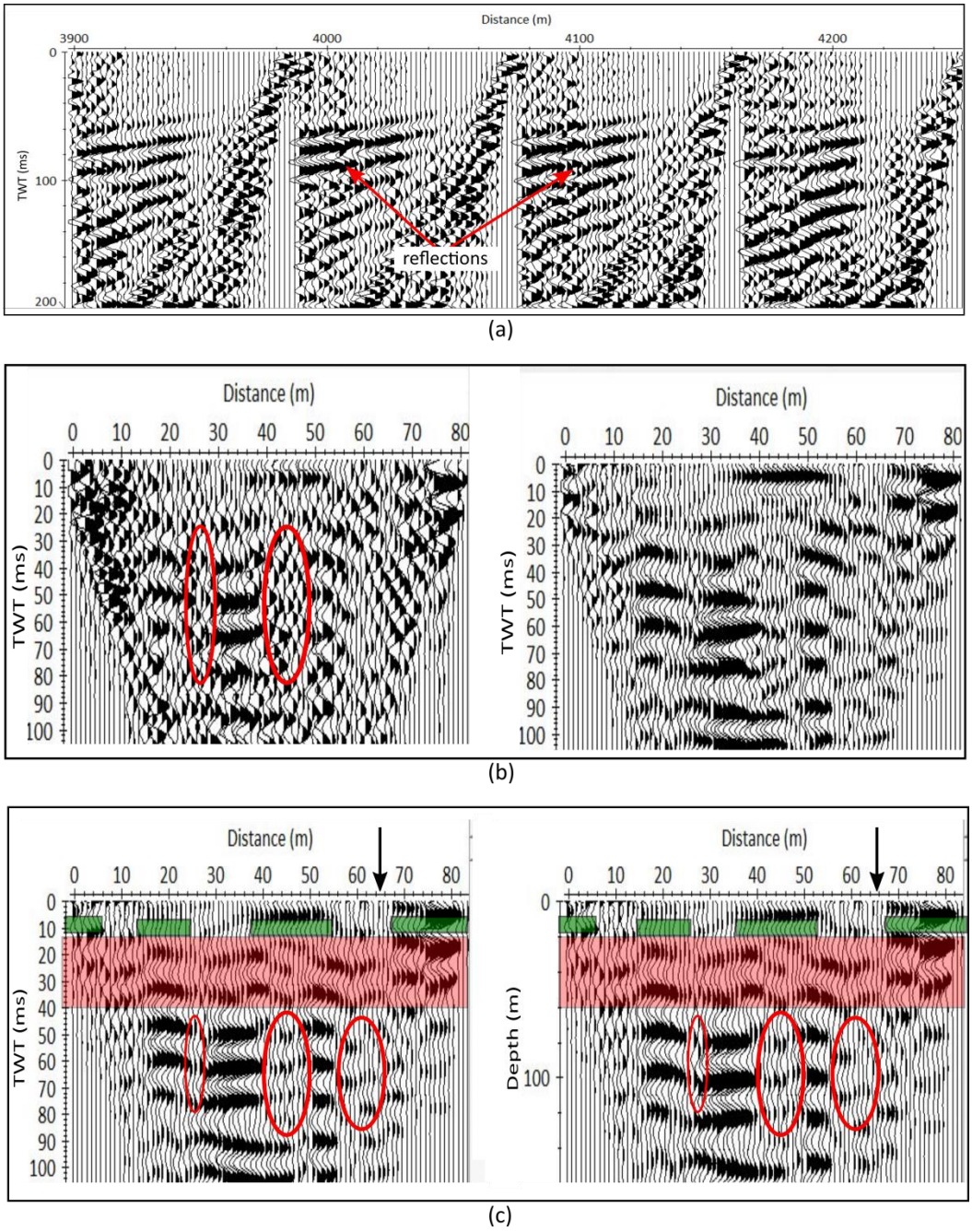



Figure 3.16: (a) Pre-stack shot gathers along LN3 with visible reflections after applying a bandpass Butterworth filter, with trace normalized gain applied for display (b) Stacked and the corresponding migrated section obtained along LN3. Note the alternating chaotic reflection zones (circled region) in the stacked section and the enhanced resolution in the migrated section, (c) Interpreted time and depth migrated section. The green colour highlights the coal seam zone within the un-mined pillars (note the coherent negative reflection amplitude characterizing the coal seam zone), while the highlighted region in red shows the disrupted bedding planes due to near-surface subsidence caused by the collapse of the overburden strata into dissolution cavities (circled region) within the underlying dolomite. The arrow indicates the location of the leaning structure in the undermined area.

Anomalous disruption of bedding planes, caused by layer undulation, is also observed to have developed directly above these cavities (Fig. 3.16c), thereby providing evidence for near-surface subsidence caused by the collapse of the overburden rock layers into dissolution cavities within the underlying dolomite. This scenario may be responsible for the abandoned leaning structure observed in the undermined area (Fig. 3.5), while the location of this structure directly above the mined-out zone (Fig. 3.16c) may also suggest an active subsidence that is due to the collapse of the colliery roof into the mined-out zone.

The Springlake datasets are generally dominated by low frequency ground-roll, but reflection events usually become visible after applying a bandpass Butterworth filter (Fig. 3.17a). The seismic sections obtained along the profile show several parallel continuous dipping reflectors that terminate at the centre of the profile (Fig. 3.17b). An anomalous disrupted zone characterized by strong discontinuous reflectors, which could indicate the presence of void or collapsed underlying pillars, is observed to occur directly below these gently dipping reflectors at the depth below approximately 40 ms (Fig. 3.17b). This disruptive zone occurs at depth of approximately 50 m (Fig. 3.18) and corresponds to the depth where the coal seam was encountered in the borehole. The general dip of these reflectors towards the centre of the profile may therefore suggest evidence of subsidence due to the collapse of the overburden strata. This subsidence could be due to the underlying mined-out voids or probably because of the failure of the pillars that act as supporting mechanism for the overburden strata (Fig. 3.17a). However, the system of pillar failure has been explained as the major mechanism for subsidence that occur at mining depth of greater than 50 m (van der Merwe

and Madden, 2010). Therefore, there is likelihood that the subsidence is caused by the failure of the supporting pillars.

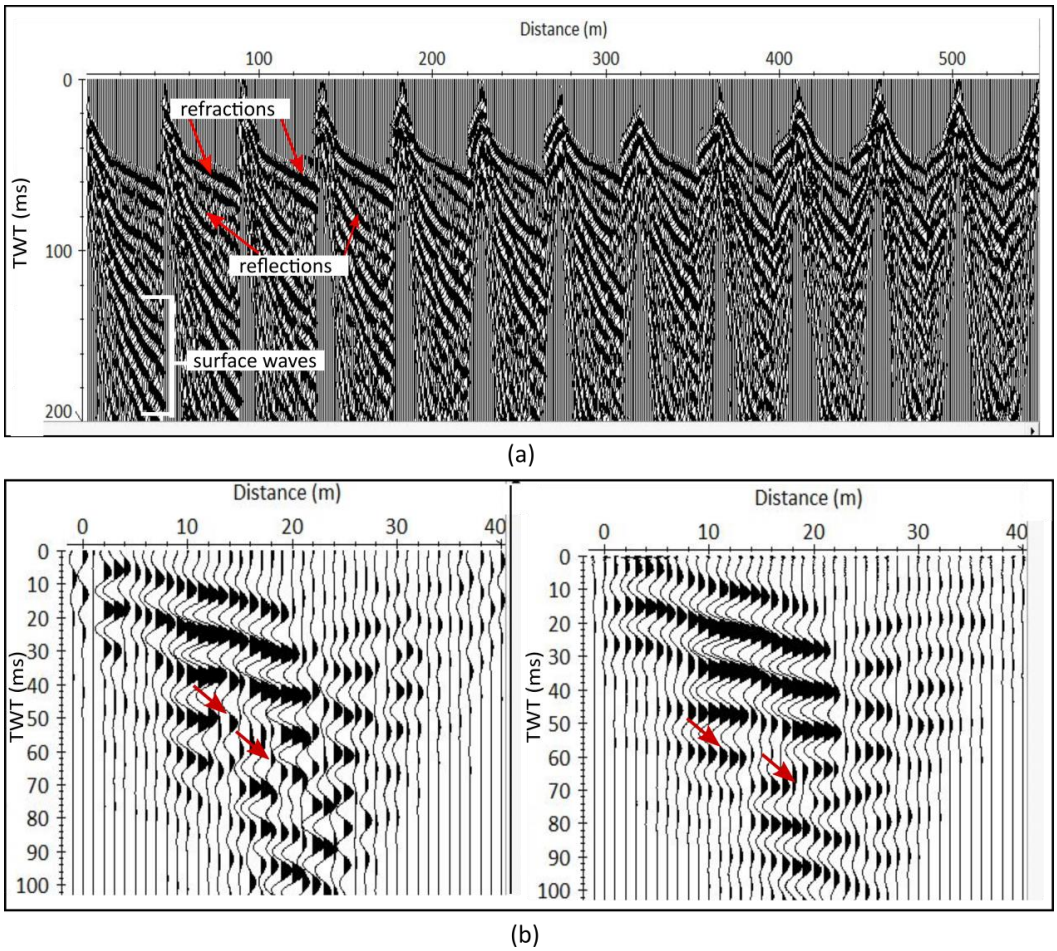



Figure 3.17**:** (a) Pre-stack shot gathers along the Springlake profile showing visible reflection events after applying a bandpass Butterworth filter, and (b) Stacked and migrated section (with AGC applied). Note the disrupted zone indicated with the arrows below ~ 40 ms.

In order to further verify the existence of the suspected void observed on the seismic section, an electrical resistivity method (ERT), using the Schlumberger electrode array configuration, was conducted parallel to the seismic profile. The 2D ERT survey utilized a roll-along method with 41 electrode channels that were spaced at 5 m. Meanwhile, the results of the ERT method did not correlate well with the seismic section. This may be due to the limited depth of approximately

46 m penetrated by the ERT method, as compared to the seismic method, or may be due to the acquisition of the two methods along different but parallel profiles. However, the ERT survey shows anomalous low resistivity zone at the depth of approximately 32 m, which may indicate the presence of a water-filled void (Fig. 3.18b) that apparently extends to a greater depth.

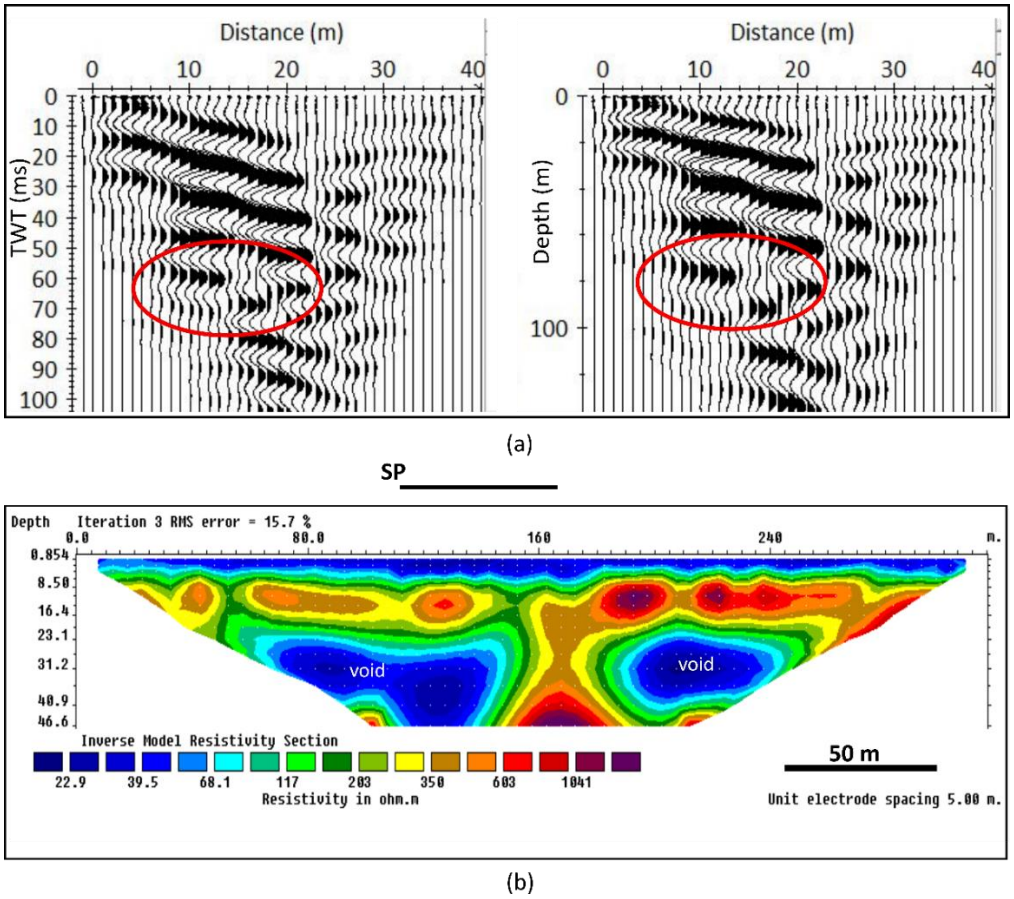



Figure 3.18: (a) The interpreted time migrated and depth section along the Springlake profile showing a disruptive zone probably due to collapsed pillar or void (circled region) (b) The 2D pseudosection from the ERT survey showing voids that probably extend to greater depth. SP indicates the region covered by the seismic line.

## 3.7 Conclusions and recommendations

The high-resolution seismic reflection investigation conducted in the two study areas has revealed the evidence of subsidence and sinkholes that are related to

subsurface voids or pillar failure. In the Benoni study area, the major cause of subsidence- and sinkhole-related features that are observed in the undermined area is due to the collapse of the overburden strata into near-surface voids caused by coal-mining and dissolution cavities that occur within the underlying dolomite layer. Therefore, it is recommended that the undermined area is avoided for any future infrastructural development, due to the vulnerability of this area to the formation of subsidence and sinkholes.

Meanwhile, the intrusive dolerite layer encountered in the north of the area is revealed by this investigation to exhibit a complex geometry bearing the characteristic of both sill and dyke. However, the dolerite layer may reach a considerable thickness of about 13 m towards the north of the study area. This implies that the northern part of the study area is less vulnerable to subsidence or sinkholes formation, because of the considerable thickness and competency of the underlying intrusive doleritic rock. Therefore, the north of the study area is recommended to be considered for future infrastructural development.

Similarly, evidence of near-surface subsidence is revealed by the seismic survey conducted within the suspected mined-out zones in the Springlake mine, where subsidence is caused by the collapse of the overburden strata due to the failure of the underlying supporting pillars. This evidence may suggest that previous coal-mining had extended beyond the established mined-out area indicated on the mine record. Therefore, it is recommended that a detailed geophysical investigation, involving high-resolution 3D seismic reflection, is conducted to adequately establish the extent of the previous mining activities in the study area.

The comparison of the resolution of the two geophone types along the same profile revealed that the two geophone types have similar vertical resolution as they were both able to resolve the dolerite layer investigated along the profile, Therefore, any of the two geophone types is recommended for future investigation involving the high-resolution seismic reflection method in the north of the study area.

## References


Baker, G. S., 1999. Processing Near-surface seismic reflection data: A primer, *Society for Exploration Geophysicists*, **9**, 77pp.

Bear Geoconsultants, 2012. Preliminary Geotechnical Assessment of Portion 62 Vlakfontein, Benoni Agricultural Holdings: Unpublished Report.

Branham, K. L. and Steeples, D. W., 1988. Cavity detection, using high-resolution seismic reflection methods, *Mining Engineering*, **40**, 115-119.

Breytenbach, I. J. and Bosch, P. J. A., 2011. Application, advantages and limitations of high-density gravimetric surveys compared with three-dimensional geological modeling in dolomite stability investigations, *Journal of the South African Institution of Civil Engineering*, **53**, 7-11.

Butler, D. K., 1984. Microgravimetric and gravity gradient techniques for detection of subsurface cavities, *Geophysics*, **49**, 1084–1096.

Button, A., 1973, A regional study of the stratigraphy and development of the Transvaal Basin in the eastern and north-eastern Transvaal, Ph.D. Thesis, University of the Witwatersrand, Johannesburg, 352 pp. (unpublished).

Buttrick, D. B., Van Shalkwyk, A., Kleywegt, R. J. and R. B. Watermeyer, 2001. Proposed method for dolomite land hazard and risk assessment in South Africa, *Journal of the South African Institution of Civil Engineering*, **43**(2), 27-36.

Council for Geosciences, 2001. Annual technical report.

Department of Water and Sanitation, 2009. Tshwane and Ekurhuleni Dolomite Compartments, Republic of South Africa.

De Bruyn, I. A. and Bell, F. G., 2001. The occurrence of sinkholes and subsidence depressions in the Far West Rand and Gauteng Province, South Africa, and their engineering implications, *Environment and Engineering Geoscience*, **7**, 281-295.

Eriksson, K. A. and Reczko, B. F. F., 1995. The sedimentary and tectonic setting of the Transvaal Supergroup floor rocks to the Bushveld Complex, *Journal of African Earth Science*, **21**, 487-504

Eriksson, P. G., Hattingh, P. J. and Altermann, W., 1995. An overview of the geology of the Transvaal Sequence and Bushveld Complex, South Africa, *Mineralia Deposita*, **30**, 98-111.

Eriksson, P. G. and Altermann, W., 1998. An overview of the geology of the Transvaal Supergroup dolomites (South Africa), *Environmental Geology*, **36**, 179-188.

Johnson, M. R., Van Vuuren, C. J., Hegenberger, W. F., Key, R., and Shoko, U., 1996. Stratigraphy of the Karoo Supergroup in Southern Africa: An overview. *Journal of African Earth Science*, **23**, 3-15

Martini, J. E. J., Eriksson, P. G. and Snyman, C. P., 1995. The Early Proterozoic Mississippi Valley-type Pb-Zn-F deposits of the Campbellrand and Malmani Subgroups, South Africa, *Mineralia Deposita*, **30**, 135-145.

Miller, R. D. and Millahn, K., 2006. High-resolution seismic reflection investigations of dissolution sinkholes (Extended Abstract): European Association of Geoscientists and Engineers (EAGE) 68$^{th}$ Conference and Exhibition, Vienna, Austria, June 12-15, 4p.

Miller, R. D. and Steeples, D. W., 1991. Detecting voids in a 0.6 m coal seam, 7 m deep using seismic reflection, *Geoexploration*, **28,** 109-119.

Miller, R. D., Villella, A., Xia, J. and Steeples, D. W., 2005. Seismic investigation of a salt dissolution feature in Kansas: Society of Exploration Geophysicists, Investigations in Geophysics, Buttler, D. K. ed., *Near-Surface Geophysics*, **13**, 681-694

Sheriff, R. E., and Geldart, L. P., 1995. Exploration seismology, *Cambridge University Press*.

Steeples, D. W., Knapp, R. W. and McElwee, C. D., 1986. Seismic reflection investigation of sinkholes beneath interstate Highway 70 in Kansas, *Geophysics*, **51**, 291-301.

Van der Merwe, N. J. and Madden, B. J., 2010. Rock engineering of underground coal mining, The Southern African Institute of Mining and Metallurgy, pp 260.

Van Shalkwyk, A., 1998. Legal aspects of development on dolomitic land in South Africa, *Environmental Geology*, **36**, 167-169.

Van Schoor, M., 2002. Detection of sinkholes using 2D electricity resistivity imaging, *Journal of Applied Geophysics*, **50**, 393-399.

Van Schoor, M. and Fourie, C. J. S., 2015. A guide for applying geophysics to coal mining problems in South Africa, *COALTECH*, South Africa, 136 pp.

Widess, M. B., 1973. How thin is a thin bed? *Geophysics*, **38**, 1176-1180.

Yilmaz, O. Z., 2001. Seismic data analysis, *Society of Exploration Geophysicists*, Tulsa, OK.

Zhou, W., Beck, B. F. and Adams, A. L., 2002. Effective electrode array in mapping karst hazards in electrical resistivity tomography, *Environmental Geology*, **42**, 922–928.

Zhou, B., Urosevic, M. and Baotang, S., 2015. Subsidence assessment using 3-D seismic data at Collingwood Park, Brisbane, *Journal of Environmental and Engineering Geophysics*, **20**, 257-272.

# Chapter 4

# 3D Seismic Analysis of the AK Fault, Orange Basin, South Africa: Implications for Hydrocarbon Leakage and Offshore Neotectonics


**Summary**

A high-resolution 3D reflection seismic dataset was processed and interpreted to produce a detailed description of the half-graben bounded AK Fault in the Ibhubesi gas field of the offshore Orange Basin. Seismic analysis of the fault involved the combination of both conventional seismic interpretation and seismic attributes. The main objective of the study was to provide insights into hydrocarbon leakage and neotectonic activities along the west coast shelf of South Africa. The AK Fault is one of several half-graben bounding faults that formed in the Late Jurassic to Early Cretaceous during the separation of the South American and the African continents. The AK Fault consists of five seismically detectable segments, whose evolution reflects characteristics of both the "coherent" and the "isolated" end-member model of segmented fault origin. Diapiric structures that are direct indicators of vertical fluid movement were also observed along the AK Fault system, providing evidence of the significant roles that the fault plays in promoting the vertical migration of hydrocarbon in the Orange Basin. Recent reactivation of the fault has also occurred along an oblique extensional regime that is dominated by normal dip-slip faulting, with minor shear components along the tips.

## 4.1 Introduction

Faults are important geological structures in petroleum exploration and production due to the role they play in the migration of hydrocarbon. They may act as conduits (i.e. forming a pathway for fluid movement) or as a sealing and permeability barrier to fluid flow. The ability of a fault to act as a barrier or conduit to fluid migration depends on a number of factors, which include the geometrical linkage with the reservoir, stress orientation, juxtaposition and the mechanical properties of the juxtaposed rocks, fault reactivation, seal failure, and inter-fault linkage (Bouvier et al., 1989; Burley et al., 1989; Hunt, 1990; Hardman and Booth, 1991; Sibson, 1996, 2000; O'Brien et al., 1999; Wiprut and Zoback, 2000; Cartwright et al., 2007; Manzocchi et al., 2008).

Besides the vital role of faults in fluid migration, most earthquakes are usually the result of deformational processes or displacement along fault surfaces. A direct relationship may also exist between fluid migration along faults and the occurrence of earthquakes (e.g. Rudnicki and Chen 1988; Hickman et al., 1995; Sibson, 1992, 1996, 2000; Yamashita, 1998). Fluid movement may initiate fault rupturing through elevated fluid pressure (Miller et al., 1996; Yamashita, 1998), just as swarms of earthquakes of magnitude up to $M_L$ 5 may be triggered by the migration of fluids through fault meshes (Sibson, 1996). The study of fault systems and fluid migration can therefore provide greater understanding of fluid transport within the crust, as well as a paleoseismic activity and earthquake hazard. In sedimentary basins, near-surface expulsion of fluids may be related to active fault systems at depth, which may manifest as fluid escape features or gas chimneys and mud volcanoes on seismic sections. These features have been

reported in many parts of the Orange Basin (e.g. Ben-Avraham et al., 2002; Viola et al., 2005; Kuhlmann et al., 2010, 2011; Boyd et al., 2011; Hartwig et al., 2012), and may provide insights into the seismicity recorded in Namaqualand and adjacent areas of southwestern Africa.

Neotectonic studies have recently gained more attention in South Africa due to the need for seismic hazard assessments of mines, sites of nuclear power generation, and nuclear waste disposal sites (Andreoli et al., 1996). Numerous studies utilizing geological mapping of active faults, in-situ stress analysis in mines, and borehole breakouts have been conducted, especially in the onshore environment, in order to understand the state of the present-day stress regime in Southern Africa (e.g. Ben-Avraham et al., 1995; Andreoli et al., 1996; Hartnady, 2002; Bird et al., 2006; White et al., 2009; Viola et al., 2005, 2012; De Beer, 2012; Hodge, 2013; Logue, 2016; Madi, 2016). Similarly, seismic reflection surveys motivated by recent oil exploration interest in the region have significantly improved the offshore geophysical database, thereby providing the opportunity to study and map several of these active structures in the offshore environment, giving insights into the tectonic processes. Several commercial 2-D seismic lines and high resolution 3-D seismic data have recently been acquired by oil and gas companies, with some available for research purposes.

One of these commercial 3D seismic data cubes from the exploration Block 2A has been used to carry out a detailed analysis of a major fault bounding the AK half-graben within the Ibhubesi gas field of the offshore Orange Basin (Fig. 4.1a). The objective of the study is to provide more insights into the hydrocarbon migration in the Orange Basin, as well as to assess the Cenozoic geodynamics,

including the neotectonic structural history of the south-west offshore of South Africa.

## 4.2 Tectonic setting and petroleum system of the Orange Basin

The AK Fault is prominent on the regional geological section across the central Orange Basin (Fig. 4.1b). It is one of the major half-graben bounding faults in the Orange Basin that evolved in response to the continental rifting of the Gondwanaland continent into Africa and South America, and the subsequent formation of the South Atlantic Ocean during the Late Jurassic to Early Cretaceous (Muntingh, 1993; Muntingh and Brown, 1993; Brown et al., 1995; Jungslager, 1999). The tectonic evolution of the Orange Basin comprises of two episodes. The pre-rift to syn-rift tectonic episode, represented by the time interval between the mid Jurassic to Early Cretaceous (~ 131 Ma), resulted in the formation of several N-S trending pre-rift and syn-rift grabens and half grabens that are aligned sub-parallel to the present-day coastline (Gerrard and Smith, 1982; Muntingh, 1993). The post-rift tectonic activity was characterized by marginal uplift and tilting, together with the development of growth faults and deep marine toe-thrusting in the Late Cretaceous (~67 Ma) (Jungslager, 1999; van der Spuy, 2003; Hartwig et al., 2012).

Evidence of neotectonic faulting, involving the Cenozoic reactivation of older Mesozoic faults, has also been documented in the Orange Basin and the near-shore Atlantic coast of southern Africa (e.g., Andreoli et al., 1996; Ben Avraham et al., 2002; Viola et al., 2005; White et al., 2009; De Beer, 2012). Ben Avraham et al. (2002) reported the alignment of mud-volcanoes in the offshore Orange

Basin, which Viola et al. (2005) later interpreted to be due to the Cenozoic reactivation of an older Cretaceous normal fault along a strike-slip regime (Fig. 4.1b).

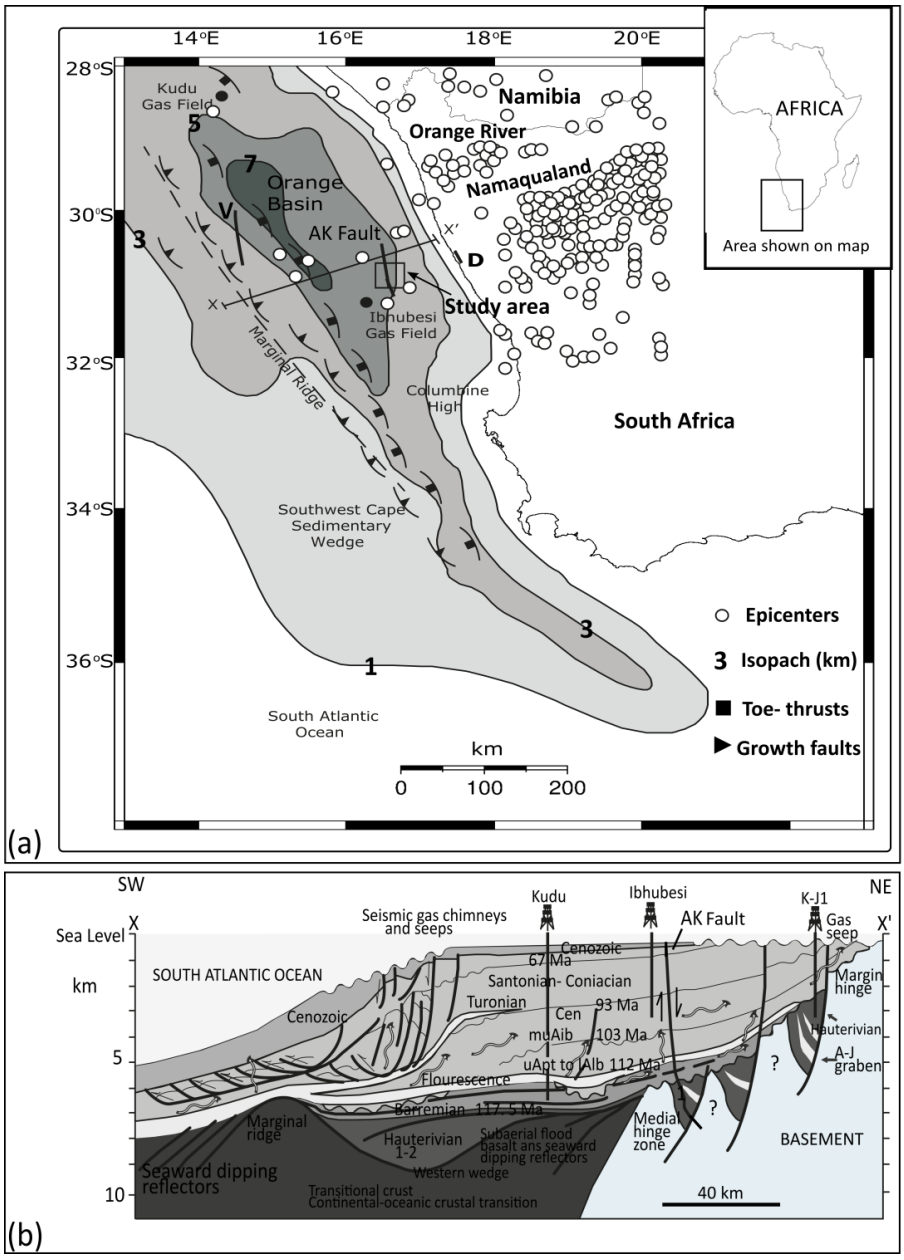



Figure 4.1: (a) Isopach map of the post-rift sedimentary succession in the offshore Orange Basin (modified from Jungslager, 1999). The outline of the AK Fault in the study area is shown along with the other two faults, "V" and "D" previously investigated by Viola et al., (2005) and De Beer (2012) respectively. The overlaid seismological data downloaded from the International Seismological Centre (2017) covers the region around southern Namibia and the Northern Cape, and shows the evidence of seismic activity within the vicinity of the AK Fault. (b) Geological cross-section across the central Orange Basin showing the AK Fault and other half-graben bounded faults (modified after Jungslager, 1999).

Pliocene to Pleistocene extensional normal faulting was also reported by De Beer (2012) along the Namaqualand coast, directly east of the study area (Fig. 4.1a). Similarly, Pleistocene to Holocene rejuvenation of the Hebron fault, southwest Namibia, has also occurred along an oblique, trans-tensional regime that is dominated by normal faulting (Viola et al., 2005; White et al. 2009).

The passive tectonic margin of South Africa is generally considered to be a stable region where seismic activity is relatively rare. However, historical records from the region have shown several earthquake events with magnitude generally less than $M_L$ 6.5 to have occurred in the area (Viola et al., 2005). The most devastating and the largest earthquake record in South Africa history occurred in 1969 in the town of Tulbagh with a magnitude $M_L$ 6.3. Earthquake swarms of magnitude $M_L$ 1-3 with an average record of six events per month have been documented in Ceres near Cape Town (e.g. Singh et al., 2009), while recurrent seismic activity measuring up to $M_L$ 4.9 is also common in the Augrabies area of the Namaqualand region (Brandt, 2011, Madi, 2016). Earthquake epicenter data retrieved from the International Seismological Centre (ISC) web site in 2017, and overlaid on the location map (Fig. 4.1a), also show relatively few seismic events (> $M_L$ 2) from the offshore region of South Africa with some of the events located within the vicinity of the AK Fault.

The Orange Basin (Fig. 4.1a) is the largest offshore basin of South Africa, occupying an estimated area of about 160 000 sq. km (Kuhlmann et al., 2010, 2011), and covers part of the offshore territory of Namibia and South Africa. The basin contains a sedimentary sequence that spans from Late Jurassic up to Holocene (Kuhlmann et al., 2010), with varied depositional thickness of about 7

km in the north to approximately 3 km in the south (Gerrard and Smith, 1982; Muntingh and Brown, 1993; Brown et al., 1995; Paton et al., 2007, 2008). The geological succession within the Orange Basin is divided into two major tectono-stratigraphic phases that are separated by a regional, ~131 Ma, Hauterivian unconformity. These include the older syn-rift and the younger post-rift and drift phases (Jungslager, 1999). The former is characterized by the development of isolated north-south trending grabens and half grabens, which are filled with lacustrine, fluvial, and aeolian sediments interbedded with volcanic rocks (Muntingh, 1993) that are truncated by the rift-drift Hauterivian unconformity. The latter was followed by the transitional succession of transgressive-regressive cycles of deepening-upward alternating fluvial red beds and marine sand. The time interval between the Late Barremian and the Early Aptian (~ 117.5 Ma) was marked by a major flooding event and the development of anoxic, source-rock-forming conditions (Muntingh, 1993; Jungslager, 1999; Van der Spuy, 2003; Paton et al., 2007). West of the study area, thermal subsidence of the continental margin and the expanding Atlantic Ocean characterized the Late Cretaceous drift stage (~ 65 Ma). These events culminated in the deposition of deep marine fans and turbidite sequences consisting of shale, siltstone, and sandstone (Muntingh, 1993; Jungslager, 1999; Kuhlmann et al., 2010). The drift succession also includes the deposition of Cenezoic prograding clastics sediments in the deep marine environment (Jungslager, 1999; van der Spuy, 2003).

The petroleum system of the Orange Basin has been discussed in detail by Muntingh (1993), Jungslager (1999), van der Spuy (2003) and Kuhlmann et al. (2010). They have identified four source rock intervals that include: (1) the

lacustrine and continentally-derived coal and carbonaceous shale of the Upper Jurassic-Lower Cretaceous syn-rift source rocks, (2) Barremian to Early Aptian transitional marine source rocks, (3) marine source rocks of the Cenomanian-Turonian interval, and (4) the transgressive anoxic marine source rocks of the Aptian. Only two liquid petroleum discoveries have so far been made in the AJ1 and the AK1 wells drilled in the AJ and the AK half-graben (Fig. 4.1b) respectively (Jungslager, 1999). The oil in the AJ1 well is derived from lacustrine sapropelic shale of the syn-rift source rocks (Jungslager, 1999). The source rocks contain a total organic carbon (TOC) of about 12 wt% and hydrogen index (HI) values greater than 600 mg hydrocarbon/g (Jungslager, 1999; Paton et al., 2007). Hydrocarbon, predominantly gas and condensate, have also been discovered in the AK1 well in commercial quantity with a good flow rate (Muntingh, 1993; Jungslager, 1999). This discovery led to the appraisal of the Ibhubesi gas field, which is South Africa's largest offshore gas field.

Reservoir rocks occur in both the syn-rift and the post-rift sedimentary sequence of the Orange Basin and include Upper Jurassic, Cretaceous, and Cenozoic clastic reservoir rocks (Muntingh, 1993; Muntingh and Brown, 1993; Jungslager, 1999). Fluvio-deltaic and lacustrine sandstone characterize the reservoirs in the syn-rift section (Jungslager, 1999), while the reservoir rocks of the post-rift section are typically made up of deltaic and turbidite sandstone. Hydrocarbon traps are both structural and stratigraphic. Structural traps include growth-fault-related structures and rotated fault blocks, while deep water fans, aeolian and turbidite sandstones characterized the stratigraphic traps (Muntingh, 1993, Muntingh and Brown,

1993; Jungslager, 1999). Primary reservoir seals are mostly marine mudstone and shale of the Cretaceous and Cenozoic deposits (Muntingh, 1993).

## 4.3 Data and methods

### 4.3.1 3D seismic reflection data acquisition

The 3D seismic survey was conducted in 1999 by Forest Oil International, with the primary objective of evaluating the exploration potential of the AK-wells and the amplitude anomalies observed in previous 2-D seismic data. The survey covers an area of 380 sq. km in exploration Block 2A of the Ibhubesi gas field, including an approximately 25- km long section of the AK Fault (Fig. 4.1a), The survey utilized a shot and receiver group interval of 25 m and 12.5 m respectively, and a nominal fold of 40 for the data acquisition. A time sampling interval of 2 ms was used in the data acquisition with a maximum recording length of 7s, which is sufficient to map the entire sedimentary sequence and part of the underlying crystalline basement. An anti-aliasing filter, with a low-cut frequency of 3 Hz at 12db/Oct and a high-cut frequency of 206 Hz at 276db/Oct, was employed in the data acquisition, resulting in a seismic dataset with a dominant frequency of about 100 Hz. Table 4.1 shows the summary of the acquisition parameters employed in the acquisition of the 3D seismic data.

### 4.3.2 3D seismic reflection data processing

The goal of seismic reflection data processing is to improve the quality of the signal, by eliminating unwanted events that may obscure the seismic reflection

events. The seismic data utilized for this study was processed by the Core Laboratories based in the United State of America using the processing sequence provided in Table 4.2. Data reformatting, geometry assignment, and gain recovery were among the initial processing sequence applied to the 3D seismic data (Table 4.2). The seismic data consists of 1018 inlines and 1381 crosslines, which were initially acquired in SEGD 8038 format and were reformatted into SEGY format that is compatible with the DISCO software package for processing. Reformatting is the first step in processing and involves reading the incoming tapes and rewriting them into specific internal format of a given processing system. The reformatting was subsequently followed by geometrical assignment that included the reconciliation of navigation and recorded seismic traces. The seismic data were free of high frequency noise or spikes, therefore trace editing involving the removal or suppression of spikes or noise bursts was not required. Gain recovery to correct for amplitude loss, due to spherical divergence, was applied using a spherical spreading correction, $V^2T$, with a residual gain of 0 db at 0 ms and 15 db at 7000 ms. A band-pass filter with low and high cut of 3 and 90 Hz, respectively, was then applied before the data was resampled to 4 ms.

Velocity analysis was performed at four different stages of the data processing, using a series of 11 CDPs at each location in all the four stages. Multiple attenuation was carried out using radon parabolic demultiple and spiking deconvolution with an operator length of 200 ms. However, prior to the application of radon parabolic demultiple, an initial set of velocities was picked on a 2 km grid of the seismic dataset obtained after applying spherical divergence and deconvolution.

Table 4.1: Seismic data acquisition parameters

| | |
|---|---|
| Energy source type | Dual airguns |
| Source volume | 3090 cubic inches |
| Source depth | 6.0 m |
| Shot interval | 25 m (flip/flop) |
| Streamer length | 4037 m |
| Number of streamers | 8 |
| Group interval | 12.5 m |
| Number of channels | 324 per stream |
| Streamer depth | 9.0 m |
| Nominal fold | 40 |
| Source to near receiver offset | 150 m |
| Sample rate | 2 ms |
| Record length | 7 s |
| Record format | SEGD- 8036 |

This dataset was used as the NMO function for applying the parabolic radon demultiple. Radon parameters of 150 p-values with a moveout of -200 to 2350 ms were then applied to the data to suppress the multiples. The second velocity analysis was performed on a 1 km grid with more accuracy, as compared to the initial set of velocities, owing to the suppression of the energy of the multiples in the dataset. The second velocity obtained after suppressing the multiples was then used for the 3D dip moveout (DMO) correction.

Table 4.2: Processing sequence for the seismic data

| Processing Sequence | Description |
|---|---|
| 1 | Convert from SEGD to disco internal format |
| 2 | Assign 3D geometry |
| 3 | Spherical divergence ($V^2T$) for gain recovery: 0 ms at 0 dB, 7000 ms at 15 dB |
| 4 | Bandpass filter: 3-90 Hz |
| 5 | Resampling to 4 ms |
| 6 | Shot average spiking deconvolution<br>Operator length: 200 ms<br>Near offset: 800-6000 ms<br>Far offset: 3500-6500 ms |
| 7 | NMO remove (radon velocities at 2 km grid) |
| 8 | Front end mute |
| 9 | CDP sort |
| 10 | Apply AGC: 1000 ms |
| 11 | Radon multiple attenuation |
| 12 | Remove AGC 1000 ms |
| 13 | NMO remove (radon velocities at 1 km grid) |
| 14 | 2:1 trace compression |
| 15 | NMO (DMO velocities at 1 km grid) |
| 16 | Mute |
| 17 | AGC 7000 ms |
| 18 | Trace interpolation to 12.5 x 12.5 m bins |
| 19 | Trace balance; start time -1000 ms, gate length -6000 ms |
| 20 | Finite difference migration (20 offsets) |
| 21 | NMO remove (DMO velocities) |
| 22 | Velocity analysis (0.5 km grid) |
| 23 | Mute |
| 24 | Stack |
| 25 | FXY deconvolution (25% addback) |
| 26 | AGC 2000 ms |

A Kirchhoff-based DMO was used for the DMO correction, and was run on 20 different offset groupings at a maximum dip of 40 ms/trace. Prior to the migration of the seismic dataset, another set of velocities was picked on the post-DMO data

at 1 km grid interval, which was used as the migration velocity for the seismic dataset. Migration of each of the 20 offsets was performed using a 1-pass finite difference Omega-x algorithm, with the maximum dip of 60° at migration frequencies of 6 to 70 Hz. The final set of velocities was then picked at 0.5 km grid interval and used for the final pre-stack time migration of the dataset. In order to further improve the signal-to-noise ratio of the seismic dataset, a linear predictive filter, using the FXY deconvolution coherency, was applied, and was followed by the application of 2000 ms AGC to the final stack volume. Table 4.2 shows the details of the processing sequence employed in the processing of the 3D seismic data.

### 4.3.3 3D seismic data resolution

The seismic data have a dominant wavelength of 24 m, assuming the average P-wave velocity in the entire sedimentary column is about 2400 m/s. This velocity value was used for the time-depth conversion wherever it is required in this study. The vertical resolution limit, using Widess' dominant wavelength criteria of one-quarter wavelength, is 6 m. The horizontal resolution is determined by the radius of the Fresnel zone, which theoretically, after migration, is 12 m. However, in practice, due to the limitation set by bin size and signal-to-noise ratio, the horizontal resolution is usually equal to the dominant wavelength after migration (e.g. Stolt and Benson, 1986), which for this seismic data is 24 m.

## 4.4 Methodology

A combined method of both conventional seismic interpretation and seismic attribute analyses was employed to achieve a detailed geometrical description of

the AK Fault system. Seismic analysis of the fault was undertaken along cross-sections and time slices, together with manual-guided automatic horizon tracking, and the use of seismic attributes such as edge and semblance (e.g. Chopra and Marfurt, 2007; Iacopini et al., 2016). The edge attribute is an edge detection attribute that uses a Sobel operator to highlight areas where there is a change in the movement and direction of the dip vectors. The attribute depends on the dip field, which represents the angle of the underground formations, and is suitable for visualizing seismic discontinuities due to faults or fractures. The semblance attribute, on the other hand, is a coherence-based attribute that measures waveform similarity between traces, and can reveal abrupt structural changes such as faults and fractures. The attribute is also sensitive to amplitude, and is suitable for delineating deformational features along the fault zone, particularly in noisy seismic data (Iacopini et al., 2016).

## 4.5 Results and discussion

### 4.5.1 AK Fault geometry

The AK Fault is a major structure defined by prominent discontinuous anomalies in the seismic sections, as it extends from the crystalline basement, through the entire post-drift sediments, up to the seabed (Fig. 4.2). It generally dips landward in a NE direction and has an overall maximum throw of approximately 100 ms TWT, which is equivalent to about 120 m. The fault is listric in form, with dip magnitude that changes with depth, and shows a minor development of a roll-over anticline on the hanging-wall (Fig. 4.2).

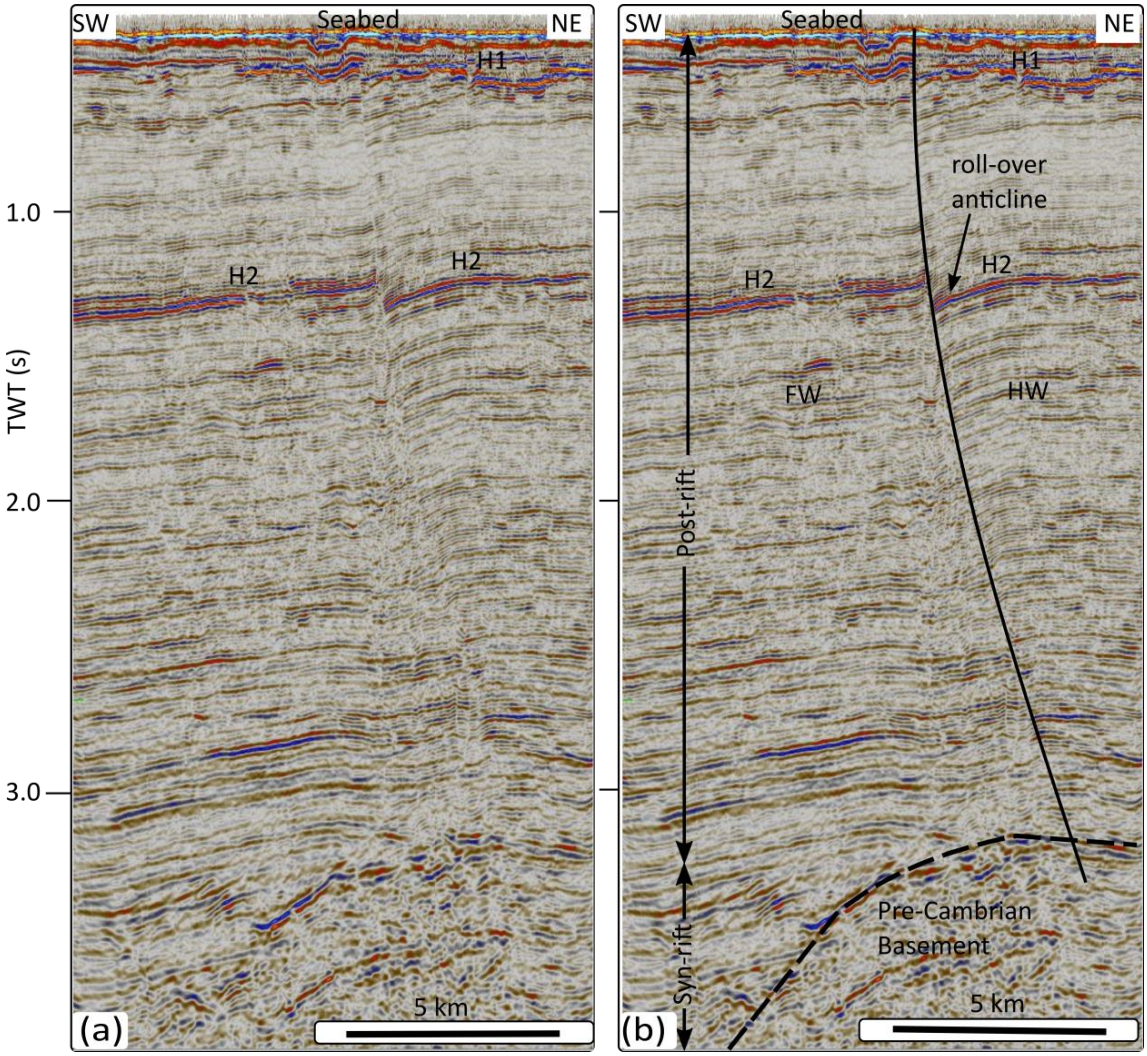



Figure 4.2: Seismic section across the northern segment of the AK Fault. (a) Uninterpreted section (b) Interpreted section showing the penetration of the fault from the underlying basement through the post-rift sediment up to the seabed, and the associated roll-over anticline. H2 and H1 horizons represent the primary reservoir seals of the Cretaceous and the Cenozoic deposits, respectively (Muntingh, 1993; Jungslager, 1999). FW- footwall, HW- hanging wall.

In a semblance attribute slice obtained at 1240 ms, the AK Fault displays variable trend along its strike, and shows two prominent segments in the north and the south that are obliquely oriented to each other (Fig. 4.3). The northern segment of the fault trends $320^0$, but changes strike direction towards the south where it assumes a trend of approximately $350^0$.

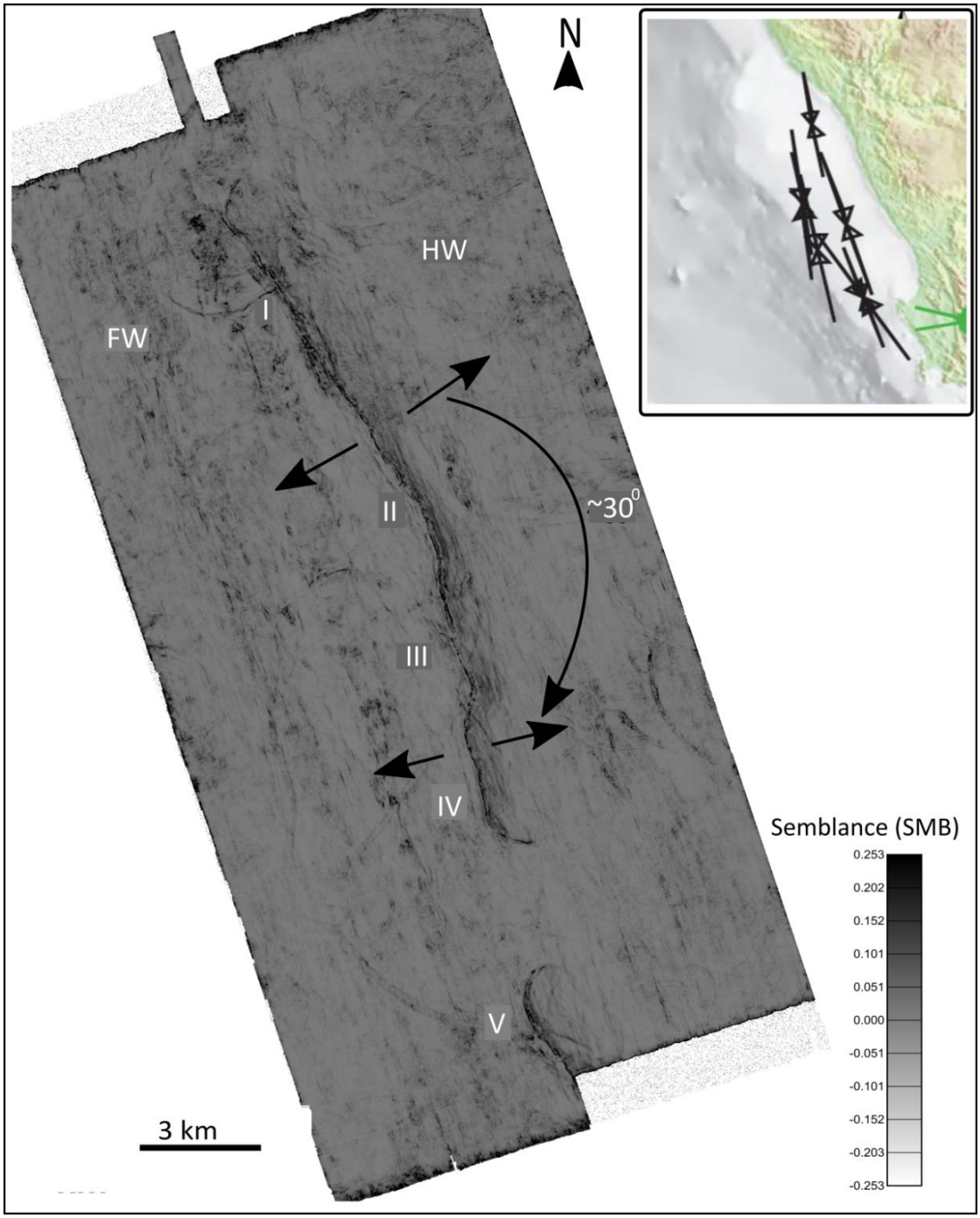



Figure 4.3: Geometry of the AK Fault in semblance slice at 1240 ms showing the different segments of the fault and a possible stress re-orientation through approximately $30^0$. The inserted map shows the average orientation of the greatest horizontal compressive stress (SHmax) in the offshore Orange Basin as determined by Logue (2016) and copied from the World Stress Map (Heidbach et al., 2016). FW- footwall. HW- hanging wall.

This variation in trend along the AK Fault strike may suggest a stress re-orientation during its evolution, which could be due to the clockwise rotation of the orthogonal extension direction through approximately 30° (Fig. 4.3). Five segments, with individual strike length of approximately 3-6 km (Fig. 4.3), can be identified along the AK Fault trace. These segments include two straight fault segments I and II in the north, which are connected along an overlap, and three curved fault segments III, IV and V in the south that are linked or separated from each other (Fig. 4.3).

The AK Fault generally displays listric geometry on seismic sections, except at the bend, where the fault trace has a sigmoidal shape (Fig. 4.4b), which may be due to the mechanical resistance to change in stress direction along the bend. Interpreted seismic sections across the AK Fault also reveal that the base of the fault segments in the north is rooted in the underlying crystalline basement (Fig. 4.2), while the curved fault segments in the south have a base that terminates along a basal decollement above the basement (Fig. 4.4c and d). Evidence of Cenozoic reactivation of the AK Fault is observed on the seismic section across one of the curved fault segments, where the Lower Cretaceous fault is cross-cut by the main Upper Cretaceous to Cenezoic fault (Fig. 4.4c). Anticlockwise rotation of beds within this zone is also noticeable (Fig. 4.4c), and may have occurred due to the free-board failure of the hanging wall along a basal decollement.

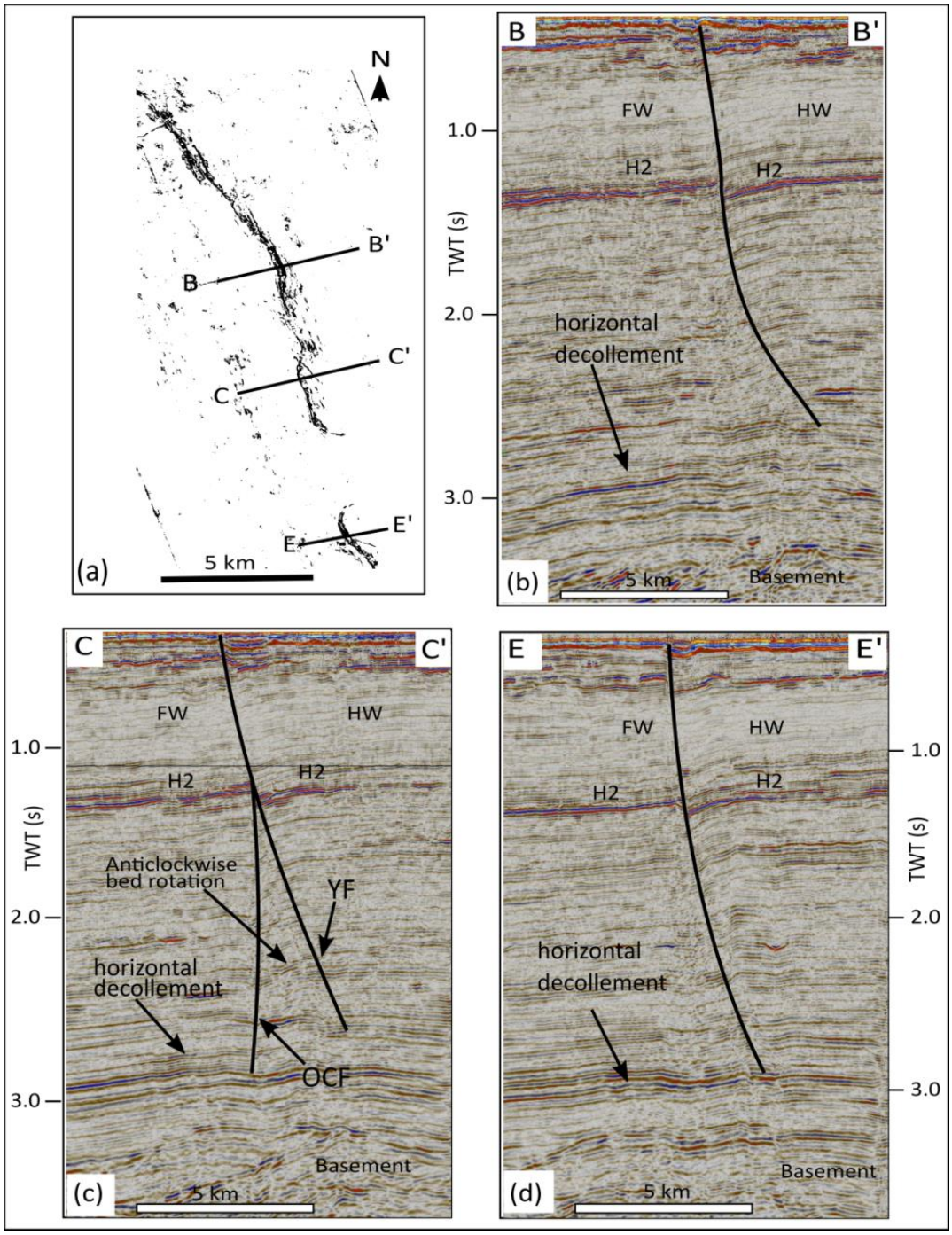



Figure 4.4: Interpreted perpendicular sections along the strike of the AK Fault. (a) Cross-sections along the different segments of the fault. (b) Sigmoidal fault plane geometry along the fault's bends. (c) Evidence of reactivation of the AK Fault revealed by the cross-cutting of the Early Cretaceous fault (OCF) by the Late Cretaceous, Cenozoic fault (YF) and the anticlockwise rotation of beds caused by the freeboard failure of the hanging-wall along a horizontal decollement. (c) Listric geometry of the AK Fault with its base along a horizontal decollement above the underlying crystalline basement. FW- footwall, HW- hanging wall.

### 4.5.2 Geometry of the relay zones

Segmented normal faults in an extensional tectonic setting usually interact at points known as relay zones or step-overs, where individual fault segments link together to form a longer fault system (Fossen and Rotevatn, 2016). The relay zones are also referred to as transfer zone, or segment boundaries (e.g. Morley et al., 1990; Gawthorpe and Hurst, 1993), where strain or displacement is transferred from one segment of the fault to the other (Rosendahl et al., 1986; Childs et al., 1995; Kristensen et al., 2008). The relay zone geometry is influenced by high shear strain, which may cause bed rotations and formation of relay ramps (Walsh et al., 2002). It is also a complex zone of localized structural deformations, such as faulting, fracturing or folding of rock (Fossen and Rotevatn, 2016).

The geometry of the relay zone is examined between the two overlapping fault segments I and II in details, using the semblance seismic attribute at different time-slices of 1100 ms, 1240 ms, and 1320 ms TWT (Fig. 4.5 (a), (b), (c)). The result shows two fault segments that are separated by an overlap at the depth of 1100 ms TWT (Fig. 4.5a), but are connected along a central fault that cuts across the center of the overlap at the depth of 1240 ms TWT (Fig. 4.5b). At the depth of 1320 ms TWT, the two overlapping faults are seen to have abandoned their respective fault tips to link together along the central fault, where they form a continuous through-going single fault trace (Fig. 4.5c). Similarly, the dimension of the relay zone is also observed in map-view to vary with depth. The dimensions (i.e. length by width) of the relay zone at 1100 ms are approximately 750 m by 300 m, but increases significantly to approximately 1500 m by 500 m at the depth of 1240 ms. Meanwhile, no increment in length or width is observed at

the depth of 1320 ms in map-view, as the dimension of the relay zone remains relatively unchanged.

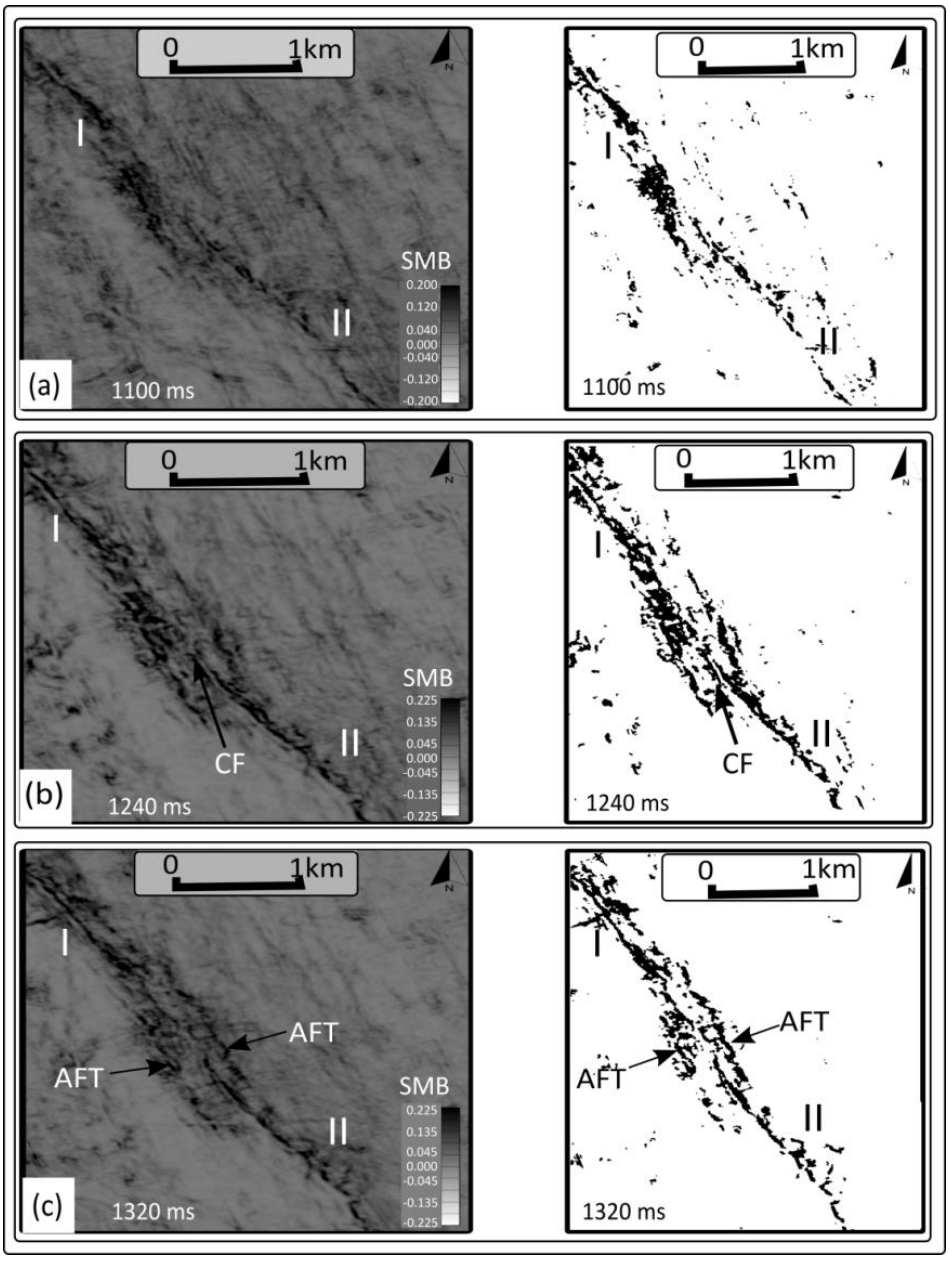



Figure 4.5: Variation in the geometry and map-view dimension of the relay zone between the two overlapping faults I and II with depth. (a) Relay zone at depth of 1100 ms showing the overlap between the two faults I and II. (b) Relay zone breaching at depth of 1240 ms along a central fault (CF) with increase in the map-view dimension. (c) A fully breached relay zone, where the two overlapping faults have abandoned their fault tips (AFT) to link together along the central fault (CF) with no changes in map-view dimension.

Further investigation conducted along the sections perpendicular and parallel to the relay zone (Fig. 4.6 (a), (b), (c)) reveals two faults that are linked together at depth (Fig. 4.6b), with apparent localized folding of the sedimentary layers that suggest a shear deformation (Fig. 4.6c). Similarly, detailed inspection of the curved fault segments in a semblance attribute slice shows a salient feature (e.g., Fossen and Rotevatn, 2016) between curved fault segment III and IV (Fig. 4.7). This may suggest a possible linkage zone, where previously-isolated individual fault segments III and IV had connected to form a through-going fault. Fault-parallel extensional fractures, with dominant NNW trend, as well as a set of subsidiary antithetic faults, are also observed in the fault zone (Fig. 4.7), particularly in the hanging wall side of the AK Fault system.

### 4.5.3 The segmented origin of the AK Fault

Segmented normal faults are common structural phenomena in most rift basins, and their evolution can be explained through a complex model involving two end-members, namely the "isolated fault model" and the "coherent fault model". The isolated fault model considers a large fault system to be a product of fault growth and linkage of initially isolated individual smaller fault segments, where fault growth or increment in fault length is achieved through lateral fault tip propagation during fault slip episodes (e.g. Walsh and Watterson, 1988; Cowie and Scholz, 1992; Gillespie et al., 1992; Trudgill and Cartwright, 1994; Cartwright et al., 1995; Huggins et al., 1995).

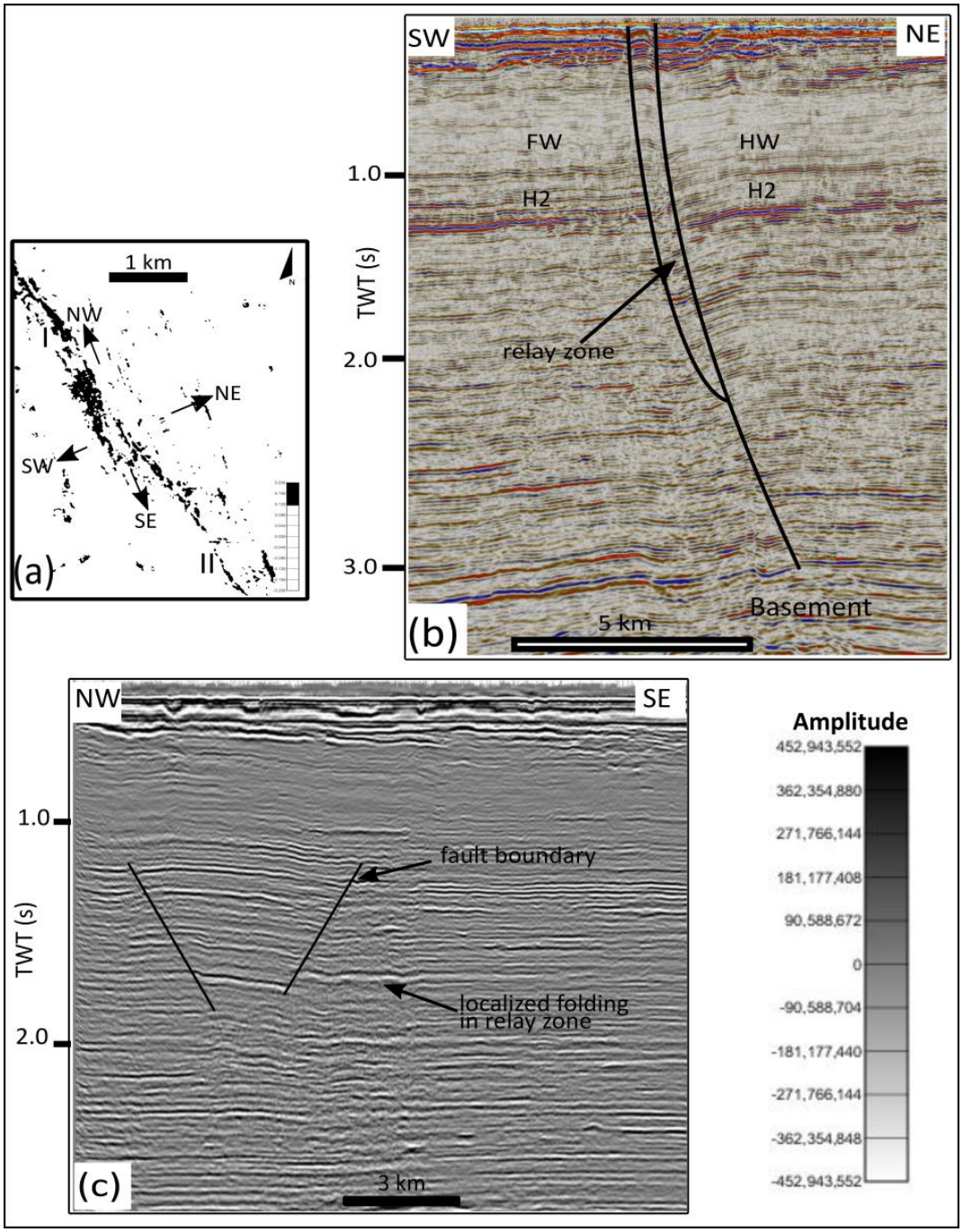



Figure 4.6: Interpreted perpendicular and parallel section across the relay zone between the two overlapping fault segments in the north. (a) Line of cross-sections across the overlapping zone. (b) Perpendicular section to the relay zone showing the linkage of the two overlapping faults at depth. (c) Parallel section with evidence of minor shear deformation revealed by localized folding of sedimentary layers in the relay zone. FW-footwall, HW- hanging wall

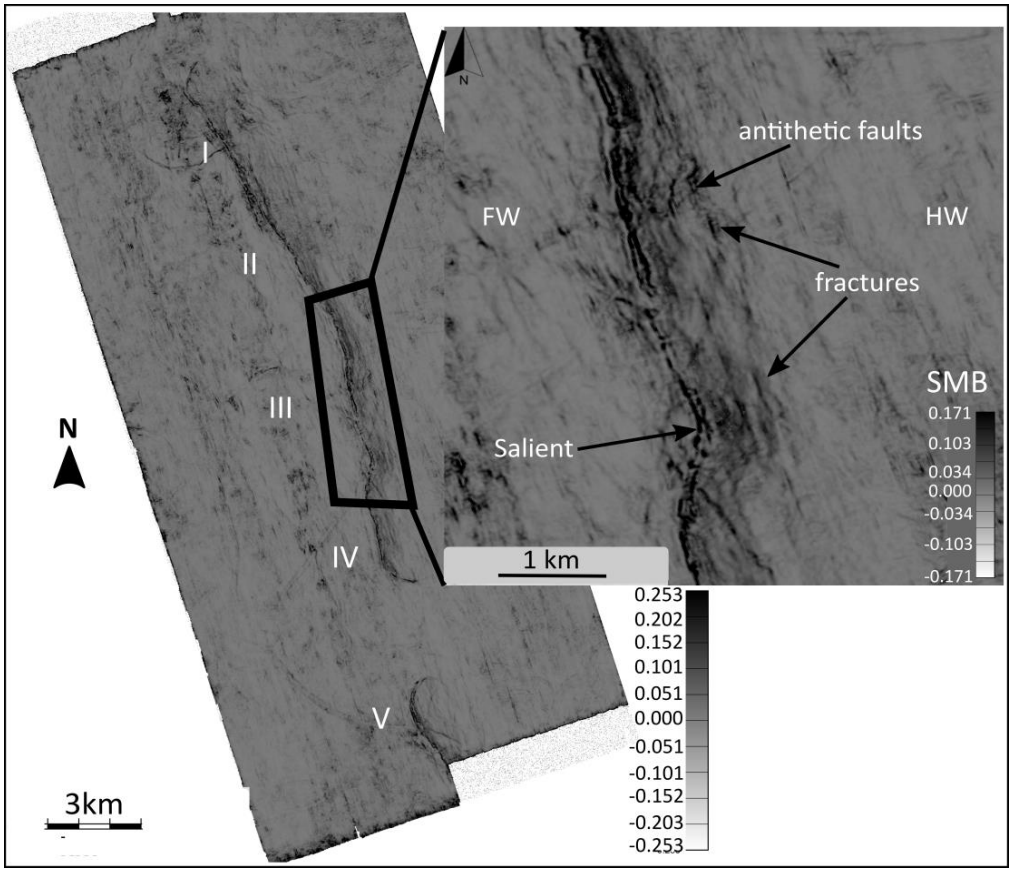



Figure 4.7: A detailed geometry of the fault zone in a semblance slice revealing a salient structure, where two previously isolated faults had linked together, as well as set of subsidiary antithetic faults and fault-parallel extensional fractures that have developed in the fault zone, especially in the hanging wall (HW) side. FW- footwall.

Instead, the coherent fault model favors the evolution of a fault as a product of the reactivation of an older fault in the underlying basement (e.g. Childs et al., 1995; Walsh et al., 2002, 2003; Giba et al., 2012; Fossen and Rotevatn, 2016). The model views the development of a segmented fault system from individual fault segments that appear in map-view as isolated segments, but are, from inception, components of the same structure, because they link to a single continuous fault surface at depth (e.g. Childs et al., 1995; Walsh et al., 2002, 2003; Giba et al., 2012). Meanwhile, unlike in the isolated fault model, the fault's growth or final length in the coherent model is rapidly established in the early stage of the fault

slip history, with no significant lateral fault tip propagation during subsequent displacement. Hence, the map-view dimension of a relay zone is also rapidly established and does not change significantly through fault's evolution (Giba et al., 2012).

The evolution of the northern segment of the AK Fault, based on the seismic analysis of the relay zone (Fig. 4.5(a), (b), (c)), favors the coherent model. Evidence derived from the analysis of the relay zone in the north shows the progressive development of the relay zone from an unbreached zone at shallower depth to a fully breached relay zone at deeper depth (Fig. 4.5(a), (b), (c)). In addition, a significant increase in the map-view dimension of the relay zone was also achieved in the early stage of development, but remains relatively unchanged in the subsequent evolutionary stage. This implies that the map-view dimension of the relay zone observed in the north of the AK Fault was rapidly established during transition from an unbreached to a partially breached relay zone. However, it remains relatively unchanged through the transition to a maturity stage of fully-breached relay zone, where the relay-bounding overlapping faults abandoned their respective fault tips to link together along a central basement fault (Fig. 4.5c).

The foregoing evidence derived from the analysis of the relay zone may therefore indicate that the two overlapping faults in the north were probably part of a single basement fault at inception. However, the two faults splayed out as the basement fault was reactivated along an oblique extension that was caused by changes in stress orientation (Fig. 4.3). This is also evident by linkage of the two relay bounding faults into a single fault at depth, as observed along the perpendicular section to the relay zone (Fig. 4.6b). Furthermore, the oblique reactivation of the

basement fault might have also culminated in minor shear deformation along fault tips, which is represented by the localized folding observed in the relay zone (Fig. 4.6c).

Meanwhile, the curved fault segments in the south of the AK Fault system were not reactivated by the basement fault. Instead, the oblique extension was initiated along a basal detachment above the underlying crystalline basement (Fig. 4.4(b), (c), (d)). This scenario resulted in the formation of several individual isolated listric dip-slip faults, which later linked together through vertical and lateral propagation during subsequent displacement (Fig. 4.7). Hence, the evolution and growth of the segmented AK Fault system may have resulted from the combination of both the coherent and the isolated fault model.

### 4.5.4 Implications for hydrocarbon leakage assessment

Relay zones in segmented fault systems are known to be effective conduits for vertical migration of hydrocarbon, because of the complex structural deformation that is associated with the damage zones that develop along these fault relays (e.g. Peacock and Perfitt, 2002; Kim et al., 2004; Rotevatn et al., 2007; Fachri et al., 2013; Fossen et al., 2005; Fossen and Rotevatn, 2016). In clastic sedimentary rocks, fractures formed within relay zones may cause fault seal failure, as well as increase in permeability and enhancement of fluid movement (e.g. Gartrell et al., 2004, Botter et al., 2016), while breached beds in relay zones have also been shown to enhance cross-fault permeability in most carbonate reservoir rocks (e.g. Manzocchi et al., 2008; Rotevatn et al., 2009).

Hydrocarbon leakage through vertical migration is a common geological event in the offshore marine environment of the Orange Basin, located in the west coast of South Africa. Several indicators of past and active hydrocarbon leakage processes, such as mud-volcanoes, pockmarks and gas chimneys, have been documented in this basin (e.g. Ben-Avraham et al. 2002; Viola et al., 2005; Paton et al., 2007; Boyd et al., 2011; Kuhlmann et al., 2010, 2011; Hartwig et al., 2012). The wide distribution of these gas leakage features in the Orange Basin and their origin have been attributed to the up-dip massive gas expulsion from the Cretaceous source rocks, through active faults that act as conduits (e.g. Ben-Avraham et al., 2002; Kuhlmann et al., 2010; Boyd et al., 2011; Hartwig et al., 2012). The structural association of these leakage features with faults (e.g. Boyd et al., 2011; Hartwig et al., 2012) also provides evidence that faults play an important role in the up-sequence migration of hydrocarbon in the Orange Basin. However, the processes responsible for the leakage along faults still remain a subject of debate among researchers.

In order to provide more insights into this geological phenomenon, the possible roles played by the relay zones observed in the AK Fault system in the vertical migration of hydrocarbon in the Orange Basin is examined. Several indirect and direct features have been proposed for identifying sub-surface fluid migration on reflection seismic data. These include gas chimneys, mud diapirs, bright spots, acoustic turbidity or chaotic reflection zone, as well as buried mud volcanoes and pockmarks (e.g. Hovland and Judd, 1988; Ligtenberg, 2005; Bradley et al., 2012). Gas chimneys, in particular, are commonly used to infer fault- and fracture-related hydrocarbon flow in reflection seismic data (e.g., Bradley et al., 2012; Ligtenberg,

2005), where they characteristically appear as zones of disrupted seismic reflection (e.g., Bradley et al., 2012).

Fluid mobilization and accumulation are enhanced in fractured zones, due to an increase in structural permeability. Therefore, detecting possible fractured zones may provide a means of assessing the sealing or leaking potential of the boundaries along fault segments. Chaotic reflection zones, suspected to be representative of fracture-related fluid accumulations, are observed on the inline sections that cut across the boundaries of some of the fault segments (Fig 4.8(a), 4.9(a)). These chaotic reflection zones are analyzed using edge attributes, with the purpose of detecting possible migration pathways along the fault segments. The result shows well-delineated fractured zones below the fault segments, where fluid will be expected to accumulate. Possible migration pathways, where fluid leakage or escape could occur, are also highlighted along the boundaries of the fault segments (Fig. 4.9b).

Similarly, fault-parallel extensional fractures observed in the fault zone may also be capable of enhancing upward migration of fluid along the fault slip surface. However, their ability to transmit fluid depends on relative orientation of the greatest horizontal compressive stress ($S_{Hmax}$). This factor has been proposed by several authors (e.g., Heffer and Lean, 1993; Sibson, 1996; Rogers and Evans, 2002; Tamagawa and Pollard, 2008) as a major determinant for faults and fractures at depth to remain open for fluid passage. A recent study in the vicinity of the AK Fault by Logue (2016), which utilized data from borehole breakouts, generally shows a NNW trend for the greatest horizontal compressive stress ($S_{Hmax}$) (Fig. 4.3). The parallel orientation of the $S_{Hmax}$ with the trend of the AK

Fault and the fractures may therefore suggest they are dilatational fractures capable of transmitting fluids.

Direct evidence of upward migration of fluid is also observed along the boundary of the isolated curved fault segment in the south (Fig. 4.8b). The feature shows an interior that is characterized by velocity pull-up and loss of reflections, and exhibits upward dipping of reflectors that suggests an upward flow of fluid materials against gravity. The structure measures about 250 m in width, and apparently has a base that is rooted in the H2 horizon (corresponding to the primary reservoir seal of the Cretaceous deposits). It has an elongated cylindrical shape that extends vertically upward to about 200 ms below the seabed, where it terminates with a collapse crater and a "bright spot" (due to a high amplitude anomaly) above it (Fig. 4.8c). This feature, which is also observed to have displaced the H1 horizon (corresponding to the primary reservoir seal of the Cenozoic deposits) is interpreted to be a buried mud volcano, while the "bright spot" observed above it may indicate active fluid expulsion along its vent (Fig. 4.8c).

Similarly, horizon tracking along the base of the H2 horizon also reveals an incipient mud diapir along the fault zone (Fig. 4.10a). The mud diapir is conical in shape with a basal width of approximately 500 m, and reaches a height of approximately 170 m. The base of the mud diapir is also observed to be aligned parallel to the AK Fault zone, which may suggest a tectonic origin. A detailed examination of the mud diapir also reveals the characteristic up-doming and faulting of overlying strata that is common to mud diapirism (Fig. 4.10b).

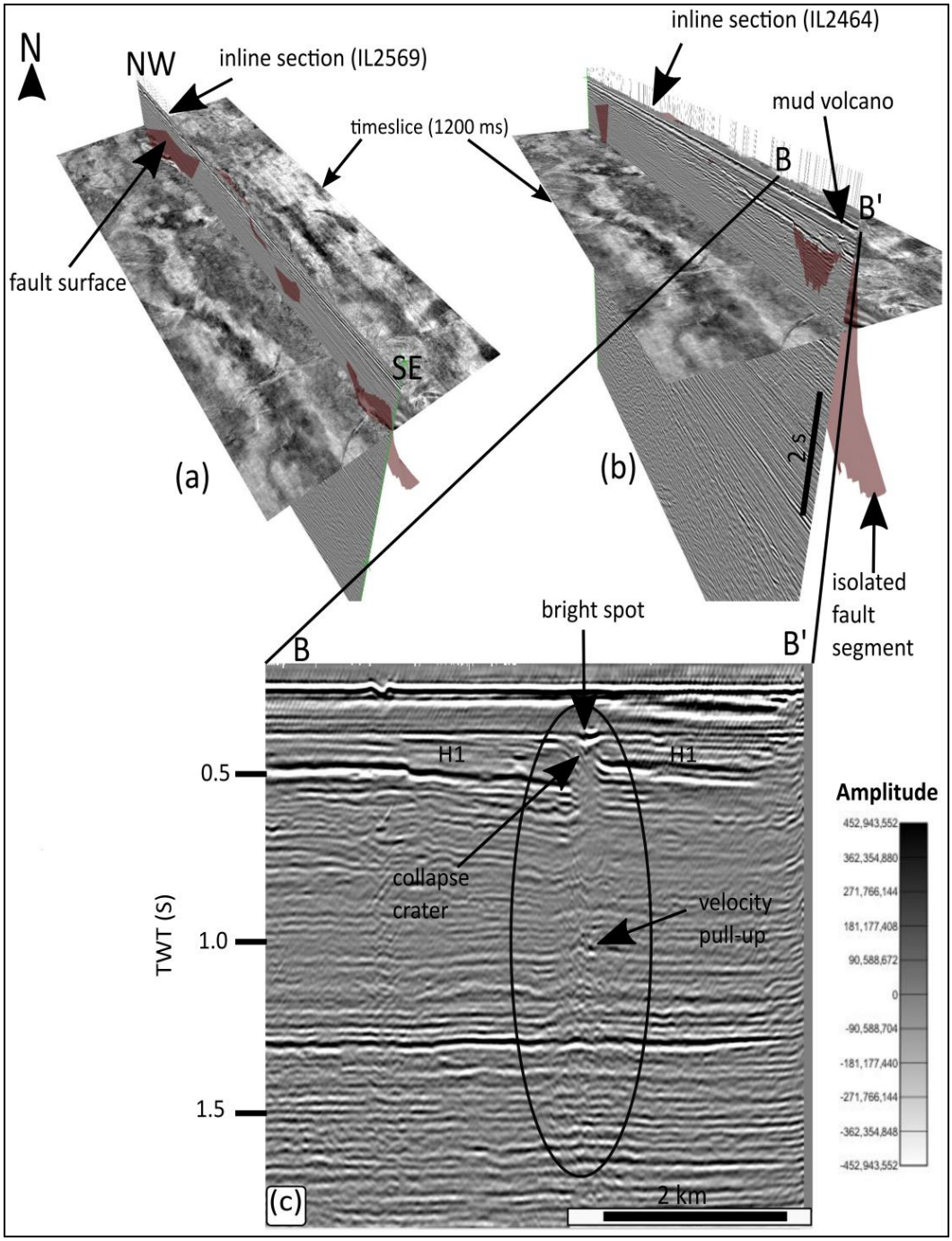



Figure 4.8: Vertical sections investigated for possible fluid leakage features. (a) Inline section along the fault surface and boundaries of the fault segments (see Fig. 9 for details). (b) Mud volcano along the boundary of the isolated curved fault segment in the south. (c) A detailed geometry of the buried mud volcano with associated collapse crater and bright spot above it. Note the displacement of the H1 horizon.

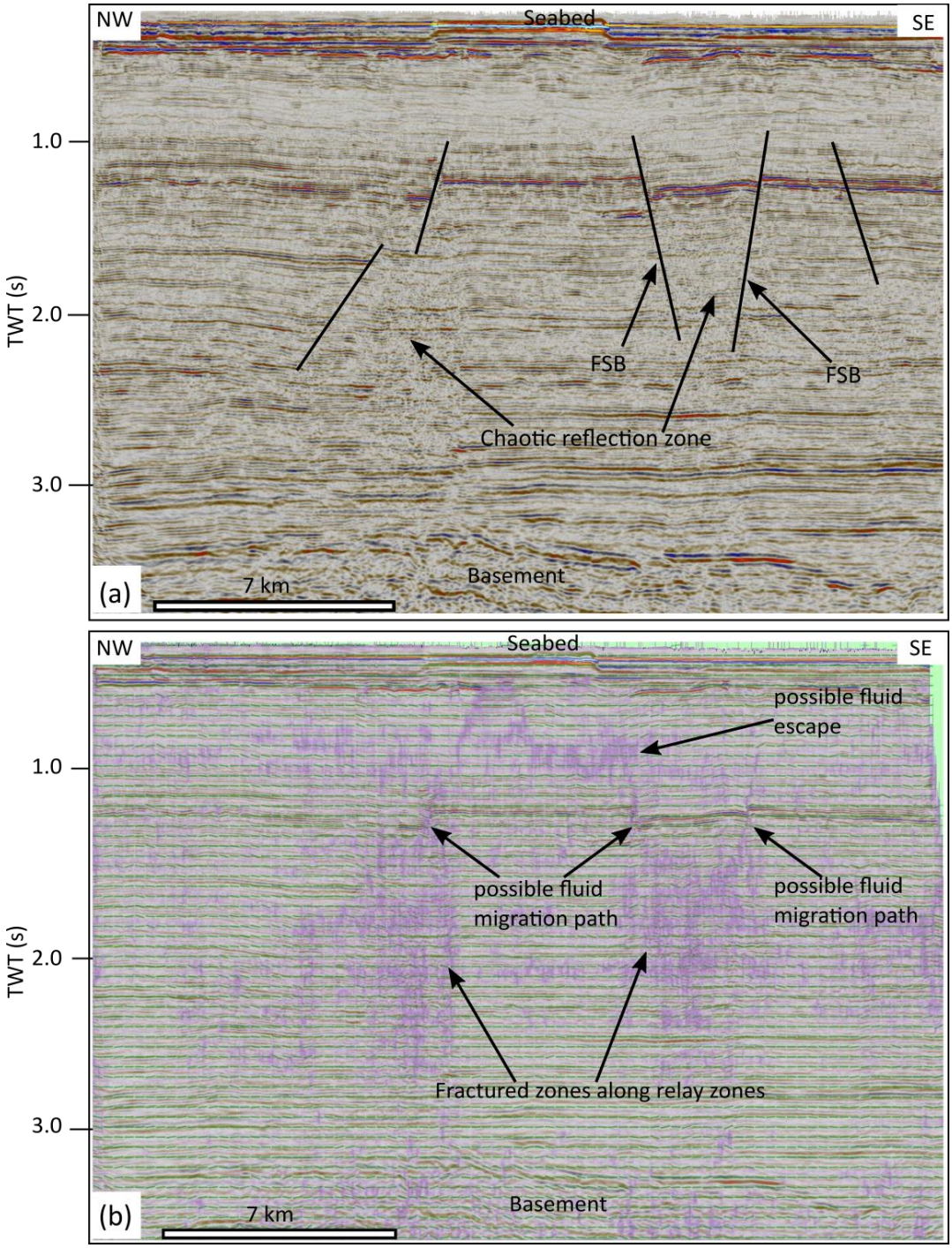



Figure 4.9: Edge attributes analysis to detect possible fluid migration pathways along the boundaries of the fault segments. (a) Interpreted inline section (see details in Fig. 8) showing the boundaries of the fault segments (FSB) and the chaotic reflection zones. (b) Edge attribute section revealing the fractured zones (in purple) where fluid may accumulate, and possible fluid migration paths through which fluid escape may occur.

In addition to the identified subsurface fluid migration along the AK Fault, evidence of surface expression of fluid seepage is also common along the seabed in the study area. Pockmarks are one of the direct indicators mostly used for identifying fluid expulsion features on the seafloor (e.g., Hartwig et al., 2012; Anka et al., 2014). Pockmarks are identified on seismic section by circular or near-circular depressions with continuous reflectors below them, which distinguish them from erosional channels that truncate reflectors (Anka et al., 2014). Pockmarks usually vary in size from 2 to 200 m in diameter (Hovland and Judd, 1988), although those with diameter of up to 1500 m have been reported along the continental margin of Gabon and Equatorial Guinea Basins of the West Africa (Pilcher and Argent, 2007). Pockmarks occur in the study area, either as a single isolated depression, or they may coalesce to form larger size or chains of elongated pockmarks (Fig. 4.11).

A tracked horizon, just below the base of the seabed (Fig. 4.11), reveals the occurrence of several chains of coalesced pockmarks that are aligned in a NW trend, which is parallel or sub-parallel to the strike of the AK Fault. This may therefore suggest a structural control on the alignment of the pockmarks that may be due to the channelized fluid expulsion along the fault zone.

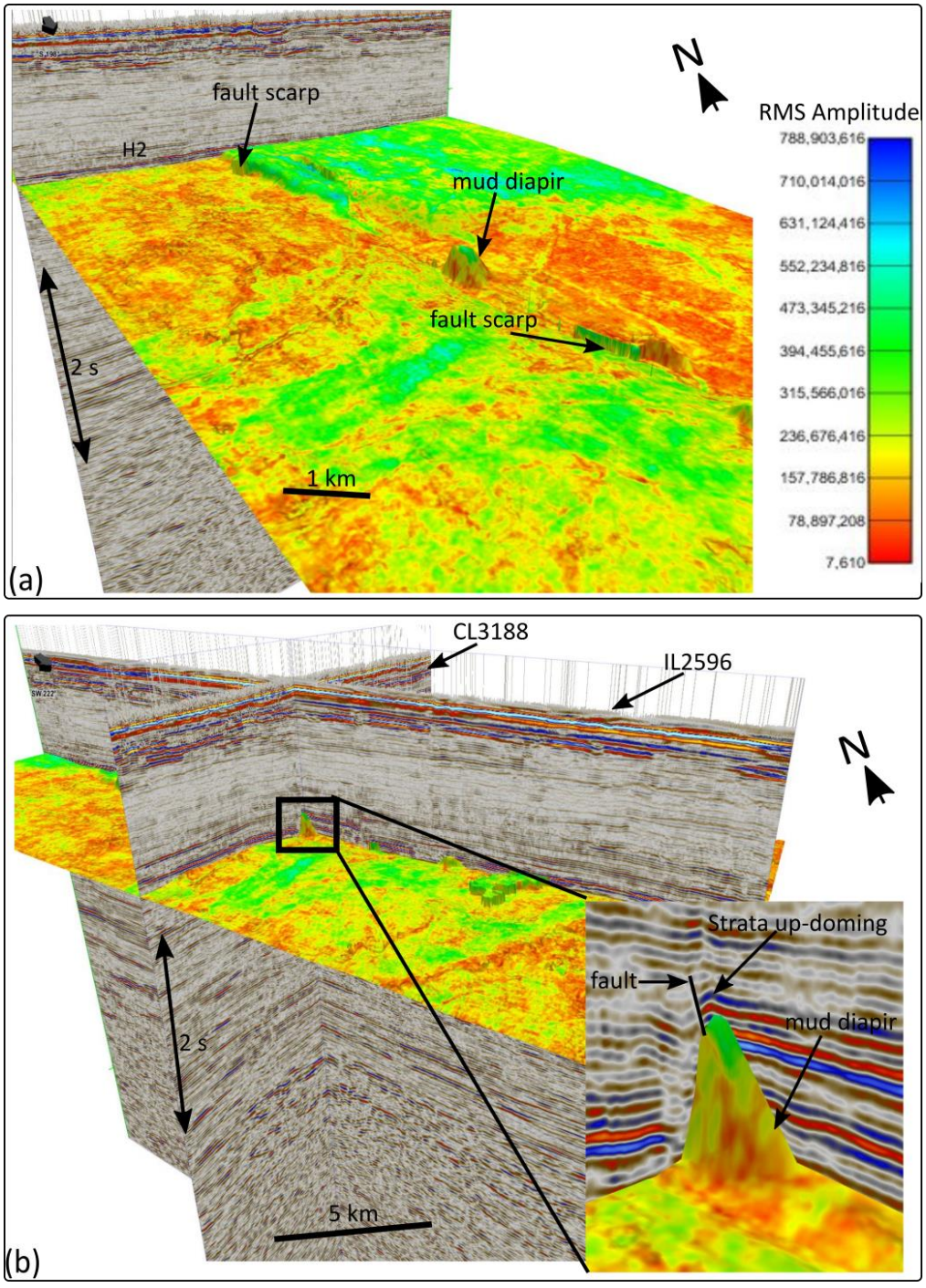



Figure 4.10: (a) A conically-shaped mud diapir at incipient stage along the AK Fault zone, with a base that is aligned parallel to the strike of the fault. (b) Structural deformation above the mud diapir is characterized by up-doming and faulting of the overlying strata.

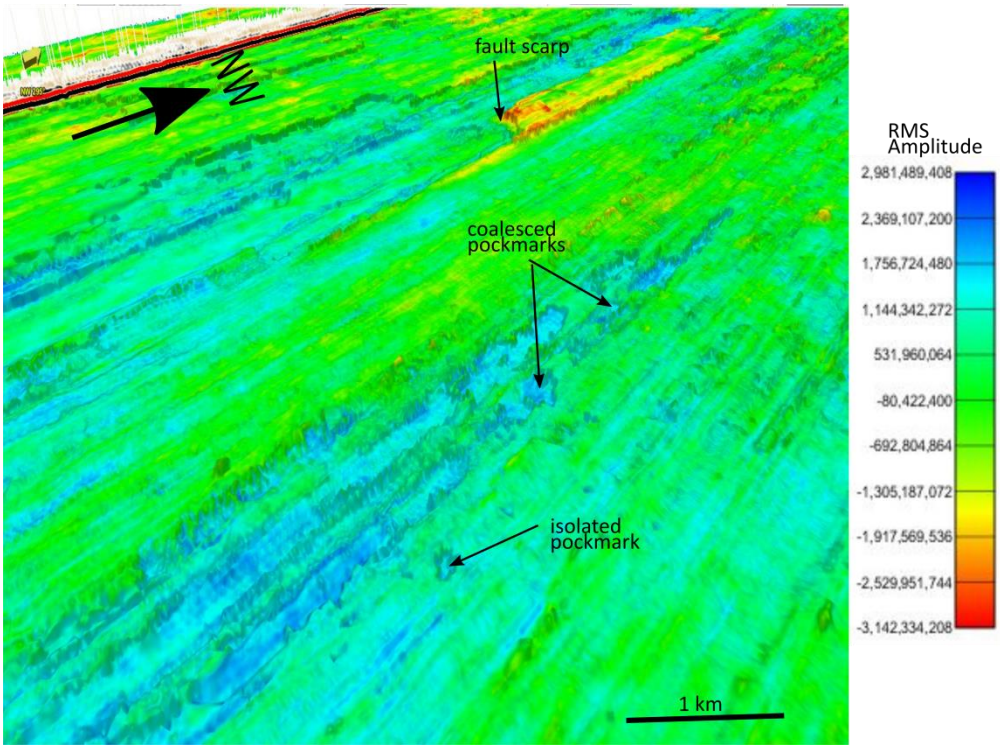



Figure 4.11: A horizon below the seabed showing both the isolated and the coalesced pockmarks. The coalesced pockmarks form elongations in a NW direction that are parallel to the direction of the AK Fault.

### 4.5.6 Implications for offshore neotectonics

The AK Fault has been active since its evolution in the Early Cretaceous up to present times, as seen by the penetration of the fault through the entire sedimentary column up to the seabed (Fig 4.2). Syn-depositional faulting, indicated by the development of rollover anticlinal structures on the hanging wall of the fault, and the observed active fluid leakage along the buried mud-volcano, also provide additional supporting evidence that the AK Fault might still be active. Evidence derived from the seismic analysis indicates that the AK Fault is extensional with predominant normal dip-slip faulting, but accommodates small components of lateral slip movement along fault tips. The fault has accrued a

maximum vertical displacement of 100 ms (~120 m) throughout its entire slip history from Cretaceous to the present day.

The recent reactivation of the fault has occurred in an oblique extension regime, caused by the clockwise re-orientation of the regional orthogonal extension direction through approximately 30°. Oblique extension involving the re-orientation of extension direction has been reported in most rift zones, including part of the East African Rift System (e,g. Ebinger et al., 1984; Strecker et al., 1990; Ring et al., 1992; Chorowicz et al., 1994; Bonini et al., 1997; Morley, 2010; Corti et al., 2013; Philippon et al., 2015). It has been attributed to the oblique orientation of pre-existing weak zone within the lower crust at rift margins to the direction of plate divergence. The fault styles that are formed in this stress regime are usually characterized by both dip-slip kinematics at the fault center and strike-slip components at fault tips (e.g., Corti et al., 2013; Philippon et al., 2015).

A recent study utilizing the data derived from borehole breakouts by Logue (2016) shows a general NNW orientation of the greatest horizontal compressive stress ($S_{Hmax}$) along the offshore Orange Basin, which is similar to the strike of the AK Fault (Fig. 4.3). These findings are also consistent with evidence of onshore neotectonic extensional reactivation of older faults along the Namaqualand coast, directly east of the study area (see Fig. 4.1: De Beer, 2012), as well as the computed model of the stress regime and orientation in the AK Fault area by Bird et al. (2006), that was based on a wide range of geophysical and geodynamic parameters. According to Bird et al. (2006), the most important driver of neotectonic stress in southern Africa, together with the gravitational instability along the continental margin, including lateral variations in lithospheric density, is

the resistance of the unbroken lithosphere to the southern propagation of the East African Rift. A similar model was also proposed for the dip-slip, extensional component of the Hebron fault in south-central Namibia by White et al. (2009). However, the Hebron and the AK Faults differ in the sense of movement, as the former displays a down-to-the-west displacement. Meanwhile, the stress regime demonstrated by the AK Fault is at odds with the strike-slip regime indicated by a ~100 km long fault of similar orientation, 200 km further to the west (cf. Fig. 4.1: Viola et al., 2005).

## 4.6 Conclusions

Seismic investigation utilizing 3D seismic data has provided a detailed description of an obliquely reactivated AK Fault, which is one of the major half-graben bounding faults in the offshore Orange Basin. The fault dips landwards in a NE direction and exhibits listric dip-slip geometry with dip magnitude that decreases with depth. Strike direction along the fault trace also varies, with two major segments that are obliquely oriented to each other in map-view, which suggests a possible low angle re-orientation of the orthogonal stress tensors during its evolution. Five seismically detectable fault segments, each with an individual strike length of approximately 3-6 km, were also identified along the strike of the fault in map-view, and are made up of two straight fault segments in the north and three curved fault segments in the south. Evolution of these segments, based on the seismic analysis, reflect characteristics of both the “isolated” and the “coherent” end-member models for the northern and the southern segments, respectively.

The role of the AK Fault system in the upward migration of hydrocarbon in the Orange Basin was also investigated. Potential migration pathways along fault segment boundaries were revealed by seismic attribute analysis. Diapiric structures that are direct evidence of vertical migration of fluid were also observed along the AK Fault systems. These include a buried mud volcano that shows evidence of active fluid leakage along its vent, and a conically-shaped mud diapir at the incipient stage. The AK Fault might still be active, as suggested by the penetration of the fault up to the seabed, and therefore offers an opportunity for neotectonic assessment along the offshore southwestern Africa.

Syn-depositional faulting, evident by the associated rollover anticline, prove that the fault has been active since its evolution in Late Jurassic to Early Cretaceous, and has accrued a maximum vertical displacement of approximately 100 ms (equivalent to about 120 m). It is proposed that the AK Fault system is being reactivated by normal faulting, with minor shear components along fault tips, and an extensional stress regime with $S_{Hmax}$ approximately parallel to its strike. Even though these findings differ from those reported for a similarly oriented fault ~200 km to the west (Viola et al., 2005), they agree with the regional stress regime of South Africa west coast (Bird et al. 2006; De Beer, 2012).

**References**

Andreoli, M. A. G., Doucoure, M., Van Bever Donker, M., Brandt, D. and Andersen, N. J. B., 1996. Neotectonics of southern Africa- a review, *Africa Geoscience Review*, **3**, 1-16.

Anka, Z., Loegering, M. J. Di Primio, R., Marchal, D., Rodriguez, J. F. and Vallejo, E., 2014. Distribution and origin of natural gas leakage in the Colorado Basin, offshore Argentina Margin, South America: seismic interpretation and 3D basin modeling, *Geologica Acta*, **12**, 269-285, doi:10.1344/GeologicaActa2014.12.4.1.

Ben-Avraham, Z., Hartnady, C. J. H. and le Roux, A. P., 1995. Neotectonic activity on continental fragments in the southwest Indian Ocean: Agulhas Plateau and Mozambique ridge, *Journal of Geophysical Research*, **100**, 6199-6211.

Ben-Avraham, Z., Smith, G., Reshef, M. and Jungslager, E., 2002. Gas hydrate and mud volcanoes on the southwest African continental margin off South Africa, *Geological Society of America*, **30**, 927-930.

Bird, P., Ben-Avraham, Z., Schubert, G., Andreoli, M. and Viola, G., 2006. Patterns of stress and strain in southern Africa, *Journal of Geophysical Research*, **111**, B08402. doi:10.1029/2005JB003882

Bonini, M., Souriot, T., Boccaletti., M. and Brun, P. J., 1997. Successive orthogonal and oblique extension episodes in a rift zone: Laboratory experiments with application to the Ethiopian Rift, *Tectonics*, **16**, 347-362.

Botter, C., Cardozo, N., Lecomte, I., Rotevatn, A. and Paton, G., 2016. The impact of faults and fluid flow on seismic images of a relay ramp over production time, *Petroleum Geoscience*, doi.org/10.1144/petgeo2016-027.

Bouvier, J. D., Kaars-Sijpesteijn, C. H., Kluesner, D. F., Onyejekwe, C. C. and van der Paul, R. C., 1989. Three-dimensional seismic interpretation and fault sealing investigations, Nun River field, Nigeria, *American Association Petroleum Geologists Bulletin*, **73**, 1397–1414.

Boyd, D., Anka, Z., di Primio, R., Kuhlmann, G. and de Wit, M. J., 2011. Passive margin evolution and controls on natural gas leakage in the Orange Basin, South Africa, *South African Journal of Geology*, **114**, 415–432.

Bradley, R. I., Samuel, H., Andrew, N., Jan, B., Miko, F., Rob, F. and Mike, M., 2012. Normal faults and gas migration in an active plate boundary, southern Taranaki Basin, offshore New Zealand, *American Association of Petroleum Geologists Bulletin*, **96**, 1733-1756, doi:10.1306/02011211088.

Brown, Jr., L.F., Benson, J. M., Brink, G. J., Doherty, S., Jollands, A., Jungslager, E. H., Keenen, A., Muntingh, A. and van Wyk, N. J. S., 1995. Sequence stratigraphy in offshore South African divergent basins. An atlas on exploration for Cretaceous lowstand traps by Soekor (Pty) Ltd., *American Association of Petroleum Geologists, Studies in Geology*, **41**, 184pp.

Burley, S.D., Mullis, J. and Matter, A., 1989. Timing diagenesis in the Tartan reservoir (UK North Sea): constraints from combined cathodoluminescence spectroscopy and fluid inclusion studies, *Marine and Petroleum Geology*, **6**, 98-120.

Cartwright, J.A., Trudgill, B.D. and Mansfield, C.S., 1995. Fault growth by segment linkage: an explanation for scatter in maximum displacement and trace length data from the Canyonlands Grabens of SE Utah, *Journal of Structural Geology*, **17**, 1319-1326.

Cartwright, J., Huuse, M. and Aplin, A., 2007. Seal bypass systems, *American Association of Petroleum Geologists Bulletin*, **91**, 1141-1166. doi:10.1306/04090705181

Childs, C., Watterson, J. and Walsh, J.J., 1995. Fault overlap zones within developing normal fault systems, *Journal of the Geological Society of London*, **152**, 535-549.

Chopra, S. and Marfurt, K. J., 2007. Seismic attributes for prospect identification and reservoir characterization, *Society of Exploration Geophysicists and European Association of Geoscientists and Engineers*.

Chorowicz, J., Collet, B., Bonavia, F. F. and Korme, T., 1994. Northwest to north-northwest extension direction in the Ethiopian rift deduced from the orientation of

extension structures and fault-slip analysis, *Geological Society of America Bulletin*, **105**, 1560-1570,

Corti, G., Philippon, M., Sani, F., Keir, D. and Kidane, T., 2013. Stress re-orientation and pure extensional faulting at oblique rift margins: Comparison between the Main Ethiopian Rift and laboratory experiments, *Terra Nova*, **25**, 396-404, doi:10.1111/ter.12049.

Cowie, P.A. and Scholz, C.H., 1992. Displacement-length scaling relationship for faults: data synthesis and discussion, *Journal of Structural Geology*, **14**, 1149-1156.

De Beer, C. H., 2012. Evidence of Neogene to Quaternary faulting and seismogenic deformation along the Namaqualand coast, South Africa, *South African Journal of Geology*, **115**, 117-136.

Ebinger. C. J., Crow, M. J., Rosendahl, B. R., Livingstonaen, D. L. and Le Fournier, J., 1984. Structural evolution of Lake Malawi, Africa, *Nature*, **308**, 627-629.

Fachri, M., Rotevatn, A. and Tveranger, J. 2013. Fluid flow in relay zones revisited: Towards an improved representation of small-scale structural heterogeneities in flow models, *Marine and Petroleum Geology*, **46**, 144–164.

Fossen, H. and Rotevatn, A., 2016. Fault linkage and relay structures in extensional settings-A review, *Earth Science Reviews*, **154**, 14-28

Fossen, H., Johansen, T. E. S., Hesthammer, J. and Rotevatn, A., 2005. Fault interaction in porous sandstone and implications for reservoir management: Examples from southern Utah, *American Association of Petroleum Geologists Bulletin*, **89**(12), 1593-1606.

Gartrell, A., Zhang, Y., Lisk, M. and Dewhurst, D., 2004. Fault intersections as critical hydrocarbon leakage zones: integrated field study and numerical modeling of an example from the Timor Sea, Australia, *Marine and Petroleum Geology*, **21**, 1165-1179.

Gawthorpe, R.L. and Hurst, J.M., 1993. Transfer zones in extensional basins: their structural style and influence on drainage development and stratigraphy, *Geological Society London*, **150**, 1137-1152.

Gerrard, T. and Smith, G. C., 1982. Post-Palaeozoic succession and structure of the south-western African continental margin, in: Watkins, J. S. and Drake, C. L. (eds.), Studies in Continental Margin Geology, *American Association of Petroleum Geologists Memoir*, **34**, 49–74.

Giba, M., Walsh, J. J. and Nicol, A., 2012. Segmentation and growth of an obliquely reactivated normal fault, *Journal of Structural Geology*, **39**, 253-267.

Gillespie, P.A., Walsh, J.J. and Watterson, J., 1992. Limitations of dimension and displacement data from single faults and the consequences for data analysis and interpretation, *Journal of Structural Geology*, **14**, 1157-1172.

Hardman, R. F. P. and Booth, J. E., 1991. The significance of normal faults in the exploration and production of North Sea hydrocarbons, in: Roberts, A. M. Yielding, G., Freeman, B. (eds.), The Geometry of Normal Faults, *Geological Society Special Publication*, **56**, 1-13.

Hartnady, C. J. H., 2002. Earthquake hazard in Africa: Perspectives on the Nubia-Somalia boundary, *South Africa Journal of Science*. **98**, 425-428.

Hartwig, A., Anka, Z. and di Primi, R., 2012. Evidence of a widespread paleo-pockmarked field in the Orange Basin: An indication of an Early Eocene massive fluid escape event offshore South Africa, *Marine Geology*, **332-334**, 222-234.

Heffer, K. and Lean, J., 1993. Earth stress orientation- a control on, and guide to, flooding directionality in a majority of reservoirs, in: Linville, W. (Ed.), Reservoir Characterization III. PennWell Books, Tulsa, Oklahoma, USA, 799-822.

Heidbach, O., Rajabi, M., Reister, K. and Ziegler, M., 2016. World stress map database release, GFZ Data Services, http://dx.doi.org/10.5880/WSM.2016.001.

Hickman, S., Sibson, R. and Bruhn, R., 1995. Introduction to special section: mechanical involvement of fluids in faulting, *Journal of Geophysical Research*, **100,** 12831-12840.

Hodge, M. S., 2013. Neotectonic deformation features in Plio-Pleistocene coastal aeolianites: Palaeoseismology and earthquake hazard implications for the Southern Cape, South Africa, Unpublished MSc. Thesis. University of Cape Town, South Africa.

Hovland, M. and Judd, J., 1988. Seabed pockmarks and seepages: Impact on Geology, Biology and Marine Environment, Graham and Trorman, London, 293pp.

Huggins, P., Watterson, J., Walsh, J. J. and Childs, C., 1995. Relay zone geometry and displacement transfer between normal faults recorded in coal-mine plans, *Journal of Structural Geology*, **17**, 1741-1755.

Hunt, J.M., 1990. Generation and migration of petroleum from abnormally pressured fluid compartments, *American Association of Petroleum Geologists Bulletin*, **74**, 1-12.

Iacopini, D., Butler, R. W. H., Purves, S., McArdle, N. and De Freslon, N., 2016. Exploring the seismic expression of fault zones in 3D seismic volumes, *Journal of Structural Geology*, **89**, 54-73.

International Seismological Centre, 2017. On-line Bulletin, http://www.isc.ac.uk Internatl. Seismol. Cent., Thatcham, United Kingdom.

Jungslager, E. H. A., 1999. Petroleum habitats of the Atlantic margin of South Africa, in: Cameron, N. R., Bate, R. H. and Clure, V. S., (Eds.), The Oil and Gas Habitats of the South Atlantic, *Geological Society London Special Publications*, **153**, 153-168.

Kim, Y.S., Peacock, D.C.P. and Sanderson, D.J., 2004. Fault damage zones, *Journal of Structural Geology*, **26**, 503-517.

Kristensen, M.B., Childs, C.J. and Korstgard, J.A., 2008. The 3D geometry of small-scale relay zones between normal faults in soft sediments, *Journal of Structural Geology*, **30**, 257-272.

Kuhlmann, G., Adams, S., Campher, C., van der Spuy, D., di Primio, R. and Horsfield, B., 2010. Passive margin evolution and its controls on natural gas leakage in the southern Orange Basin, blocks 3/4, offshore South Africa, *Marine and Petroleum Geology*, **27**, 973–992.

Kuhlmann, G., Adams, S., Anka, Z., Campher, C., di Primio, R. and Horsfield, B., 2011. 3D petroleum system modeling within a passive margin setting, Orange Basin, block 3/4, offshore South Africa- implications for gas generation migration and leakage, *South African Journal of Geology*, **114**, 387–414.

Ligtenberg, J. H., 2005. Detection of fluid migration pathways in seismic data: Implications for fault seal analysis, *Basin Research*, **17**, 141-153, doi:10.1111/j.1365-2117.2005.00258.x.

Logue, O., 2016. Orientation of the maximum horizontal stress ($S_{Hmax}$) in the Orange Basin and Outeniqua sub-basins of South Africa, Unpublished M.Sc. Thesis, University of Cape Town, South Africa.

Madi, K., 2016. Seismicity and neotectonic uplift in the Augrabies Falls National Park, Namaqualand, Northern Cape, South Africa, *Earthquake Science*, **29**, 281-289, doi10.1007/s11589-016-0166-z.

Manzocchi, T., Heath, A.E., Palananthakumar, B., Childs, C. and Walsh, J.J., 2008. Faults in conventional flow simulation models: a consideration of representational assumptions and geological uncertainties. *Petroleum Geosciences*, **14**, 91-110.

Miller, S.A., Nur, A. and Olgaard, D.L., 1996. Earthquakes as a coupled shear stress-high pore pressure dynamical system, *Geophysical Research Letter*, **23,** 197-200.

Morley, C.K., 2010. Stress re-orientation along zones of weak fabrics in rifts: an explanation for pure extension in 'oblique' rift segments? *Earth and Planetary Science Letters*, **297**, 667‑673.

Morley, C.K., Nelson, R.A., Patton, T.L. and Munn, S.G., 1990. Transfer zones in the East African rift system and their relevance to hydrocarbon exploration in rifts, *American Association of Petroleum Geologists Bulletin*, **74**, 1234-1253.

Muntingh, A., 1993, Geology, prospects in Orange Basin offshore western South Africa, *Oil and Gas Journal*, **91**, 105-109.

Muntingh, A. and Brown Jr., L.F., 1993. Sequence stratigraphy of petroleum plays, postrift Cretaceous rocks (Lower Aptian to Upper Maastrichtian), Orange Basin, western Offshore, South Africa, in: Weimar, P., Posamentier, H. (Eds.), Siliciclastic Sequence Stratigraphy, Recent Developments and Applications, *The American Association of Petroleum Geologists Memoir*, **58**, 71-98.

O'Brien, G. W., Lisk, M., Duddy, I. R., Hamilton, J., Woods, P. and Cowley, R., 1999. Plate convergence, foreland development and fault reactivation: Primary controls on brine migration, thermal histories and trap breach in the Timor Sea, Australia, *Marine and Petroleum Geology*, **16**, 533-560. doi:10.1016/S0264-8172(98)00070-1.

Paton, D.A., di Primio, R., Kuhlmann, G., van der Spuy, D. and Horsfield, B., 2007. Insights into the petroleum system evolution of the southern Orange Basin, South Africa, *South African Journal of Geology*, **110**, 261-274.

Paton, D.A., van der Spuy, D., di Primio, R. and Horsfield, B., 2008. Tectonically induced adjustment of passive-margin accommodation space: influence on the hydrocarbon potential of the Orange Basin, South Africa, *American Association of Petroleum Geologists Bulletin*, **92**, 589-609.

Peacock, D. C. P. and Parfitt, E. A., 2002. Active relay ramps and normal fault propagation on Kilauea Volcano, Hawaii, *Journal of Structural Geology*, **24**, 729-742.

Philippon, M., Willingshofer, E., Sokoutis, D., Corti, G., Sani, F., Bonini, M. and Cloetingh, S., 2015. Slip re-orientation in oblique rifts, *Geology*, **43**, 147-150; doi:10.1130/G36208.1

Pilcher, R. and Argent, J., 2007. Mega-pockmarks and linear pockmark trains on the West African continental margin, *Marine Geology*, **244**, 15-32.

Ring, U., Betzler, C. and Delvaux, D., 1992. Normal versus strike-slip faulting during rift development in East Africa: The Malawi rift, *Geology*, **20**, 1015-1018.

Rogers, S. F. and Evans, C. J., 2002. Stress-dependent flow in fractured rocks at Sellafield, United Kingdom, in: Lovell, M. and Parkinson, N. (eds.), Geological Applications of Well Logs Methods in Exploration, *The American Association of Petroleum Geologists*, Tulsa, Oklahoma, USA, **13**, 241-250

Rosendahl, B.R., Reynolds, D.J., Lorber Burgess, C.F., McGill, J., Scott, D., Lambiase, J.J. and Derksen, S.J., 1986. Structural expressions of rifting: lessons from Lake Tanganykia, Africa. *Geological Society London Special Publications*. **25**, 29–43.

Rotevatn, A., Fossen, H. and Hesthammer, J., 2007. Are relay ramps conduits for fluid flow? Structural analysis of a relay ramp in Arches National Park, Utah, *Geological Society London Special Publication*, **270**, 55-71.

Rotevatn, A., Tveranger, J. and Howell, J.A., 2009. Dynamic investigation of the effect of a relay ramp on simulated fluid flow: geocellular modelling of the Delicate Arch Ramp, Utah, *Petroleum Geoscience*, **15**, 45-58.

Rudnicki, J.W. and Chen, C.H., 1988. Stabilization of rapid frictional slip on a weakening fault by dilatant hardening, *Journal of Geophysical Research*, **93,** 4745–4757.

Sibson, R.H., 1992. Implications of fault-valve behavior for rupture nucleation and recurrence, *Tectonophysics*, **18**, 1031-1042.

Sibson, R.H., 1996. Structural permeability of fluid-driven fault-fracture meshes, *Journal of Structural Geology*, **18**, 1031-1042.

Sibson, R. H., 2000. Fluid involvement in normal faulting, *Journal of Geodynamics*, **29**, 469-499.

Singh, M., Kijko, A. and Durrheim, R., 2009. Seismotectonic models for South Africa: synthesis of geoscientific information, problems, and the way forward. *Seismology Research Letter*, **80**, 71-80. http://dx.doi.org/10.1785/gssrl.80.1.71.

Stolt, R. H. and Benson, A. K., 1986. Seismic migration- theory and practice, Geophysical Press, London-Amsterdam.

Strecker, M. R., Blisniuk, P. M. and Eisbacher, G. H., 1990. Rotation of extension direction in the central Kenya Rift, *Geology*, **18**, 299-302.

Tamagawa, T. and Pollard, D. D., 2008. Fracture permeability created by perturbed stress fields around active faults in a fractured basement reservoir, *American Association of Petroleum Geologists Bulletin*, **92**, 743-764. doi**:** 10.1306/02050807013

Trudgill, B. and Cartwright, J., 1994. Relay-ramp forms and normal-fault linkages, Canyonlands National Park, Utah, *Geological Society of America Bulletin*, **106**, 1143-1157.

van der Spuy, D., 2003. Aptian source rocks in some South African Cretaceous basins, *Geological Society London Special Publications*, **207**, 185-202.

Viola, G., Andreoli, M., Ben-Avraham, Z., Stengel, I. and Reshef, M., 2005. Offshore mud volcanoes and onland faulting in southwestern Africa: neotectonic implications and constraints on the regional stress field, *Earth and Planetry Science Letters*, 231, 147-160

Viola, G., Kounov, A., Andreoli, M. A. G. and Mattila, J., 2012. Brittle tectonic evolution along the western margin of South Africa: More than 500 Myr of continued reactivation. *Tectonophysics*, **514-517**, 93-114.

Walsh, J.J. and Watterson, J., 1998. Analysis of the relationship between displacements and dimensions of faults, *Journal of Structural Geology*, **10**, 239-247.

Walsh, J.J., Nicol, A. and Childs, C., 2002. An alternative model for the growth of faults, *Journal of Structural Geology*, **24**, 1669-1675.

Walsh, J.J., Bailey, W.R., Childs, C., Nicol, A. and Bonson, C.G., 2003. Formation of segmented normal faults: a 3-D perspective, *Journal of Structural Geology*, **25**, 1251-1262.

White, S., Stollhofen, H., Stanistreet, I. G. and Lorenz, V., 2009. Pleistocene to Recent rejuvenation of the Hebron Fault, SW Namibia, in: Reicherter, K., Michetti, A.M., and Silva, P. G. (Eds.), Palaeoseismology: Historical and Prehistorical Records of Earthquake Ground Effects for Seismic Hazard Assessment, *The Geological Society London Special Publications*, 316, 293-317. doi: 10.1144/SP316.18

Wiprut, D. and Zoback, M.D., 2000. Fault reactivation and fluid flow along a previously dormant normal fault in the northern North Sea, *Geology*, **28**, 595-598.

Yamashita, T., 1998. Simulation of seismicity due to fluid migration in a fault zone, *Geophysical Journal International*, **132**, 674-686.

# Chapter 5

# Volume Rendering of 3D Seismic Reflection Data Reveals a Possible Impact Structure in the Orange Basin, Offshore South Africa.


**Summary**

We have interpreted high-resolution 3D reflection seismic data from the exploration Block 2A of the Orange Basin, offshore South Africa, using the 3D volume rendering technique. The objective was to investigate an enigmatic circular structure observed on a time slice. The technique revealed the circular structure to be a crater of approximately 5-7 km in diameter, and shows morphological characteristics similar to those of complex impact structures. Evidence supporting the hypothesis that the feature is an impact crater includes the lack of fluid escape vent below it, the presence of annular rim faults, the presence of a central peak, and the presence of an approximately 400 m wide gully, which probably created the resurge of water back into the crater after the impact. The volume rendering of the 3D seismic data also revealed the association of the crater with sub-marine alluvial delta fans, suggesting that the rapid burial of the structure led to its eventual preservation. However, conclusive proof that this enigmatic circular feature is indeed an impact crater depends on geological evidence from borehole data.

## 5.1 Introduction

Conventional interpretation of 3D seismic data is usually based on the generation of time slices and cross-sections along in-lines and cross-lines, which often make the identification of structural and depositional relief features challenging. However, image enhancement techniques have improved tremendously with the introduction of seismic attribute methods. Since their first introduction in 1970s, seismic attributes have played an increasing important role in the interpretation of seismic reflection data. This development has significantly assisted in maximizing the information that can be derived from seismic data, thereby improving structural and stratigraphic interpretation, as well as reservoir characterization.

Recent advances in seismic interpretation technology include 3D visualization techniques. One such techniques is the 3D volume rendering, which is widely applied in the medical field, where it is used in the visualization of Computer Tomography (CT) scans and Magnetic Resonance Imaging (MRI) (Paul et al., 1999; Raskar and Cohen, 1999; Hauser et al., 2001). This technique has been modified and adopted for the visualization of 3D reflection seismic data (e.g., Gerhardt et al., 2001; Worrel, 2001; Silva et al., 2003; Laurent et al., 2005; Huw, 2009; Gerald, 2014), and is now available in most seismic interpretation software packages.

The volume rendering technique provides a quick way of scanning through a 3D seismic volume in order to gain an overview of the structural and stratigraphic features. During volume rendering, it is possible to manipulate the amplitude such that low, high or intermediate amplitude attributes representing different seismic

features in a seismic data can be enhanced or suppressed. This process, which is known as opacity removal (Yilmaz, 2001; Gerald, 2014), requires that parts of the volume are assigned different degrees of transparency. This process provides a quick and easy recognition of relief or topographic features, which, ordinarily, may not be visible on conventional time slices, and enhances the recognition of discontinuities such as faults.

We have interpreted a high-resolution 3D reflection seismic dataset from the offshore Orange Basin, southwest of South Africa, using the 3D volume rendering technique. The objective is to provide more insights into an enigmatic circular feature observed on a time slice.

## 5.2 Geological setting of the Orange Basin

The Orange Basin is located within the southern Atlantic passive margin that formed during the break-up of Gondwana in the Upper Jurassic. The basin has an approximate area of about 130 000 sq. km (Kuhlmann et al., 2010), extending offshore southern Namibia and South Africa (Fig. 5.1). Sedimentary deposits within the basin contain continental, paralic and marine sediments of Mesozoic to present day age that overlie the stretched African continental crust. Most published literature on the sedimentary succession and structural evolution of the basin were based on exploration seismic datasets and well reports (e.g. Gerrard and Smith, 1982).

The geological sequence within the basin is generally divided into two tectonostratigraphic regimes, syn-rift and post-rift, separated by the Hauterivian unconformity (Granado, 2006). The syn-rift sequence is characterized by Upper

Jurassic to Lower Cretaceous (~160-130 Ma) fault-controlled sediments deposited within a series of underlying grabens, which is typical of rift basins. The syn-rift deposits are predominantly siliciclastic, lacustrine sediments infills with volcanic intrusion (Paton et al., 2007; Kuhlmann et al., 2010). They are overlain by the transitional Upper Cretaceous siliciclastic deposits that show a deepening-upward sequence from fluvial red beds to deltaic deposits (Gerrard and Smith, 1982).

The post-rift sequence is made up of about 7 km thickness of siliciclastic sedimentary deposits in the north that thins out to about 3 km thickness in the south of the basin (e.g. Gerrard and Smith, 1982; Brown et al., 1995; Tinker et al., 2008),

## 5.3 3D Seismic data and methodology

### 5.3.1 Seismic data acquisition and processing

A high resolution, pre-stack, time-migrated, 3D seismic reflection cube from exploration Block 2A (AK99), offshore, south-west of South Africa (Fig. 5.1) was employed in this study. The seismic data was acquired in 1999 by Forest Oil International, covering an area of 380 sq. km. The main exploration objective of the seismic survey was to evaluate the hydrocarbon potential in the AK well surveys, with special attention to the structural and amplitude anomalies that exist between 2500-3000 ms. The data was acquired utilising a nominal fold of 40 and a bin size of 25 m, and a receiver group spacing of 12.5 m. The total recording length of 7.0 s was employed in the seismic survey, which provides the maximum coverage of the entire sedimentary sequence and part of the underlying crystalline

basement rocks within the exploration Block 2A. More details of the parameters employed in the seismic data acquisition have been presented in Table 4.1.

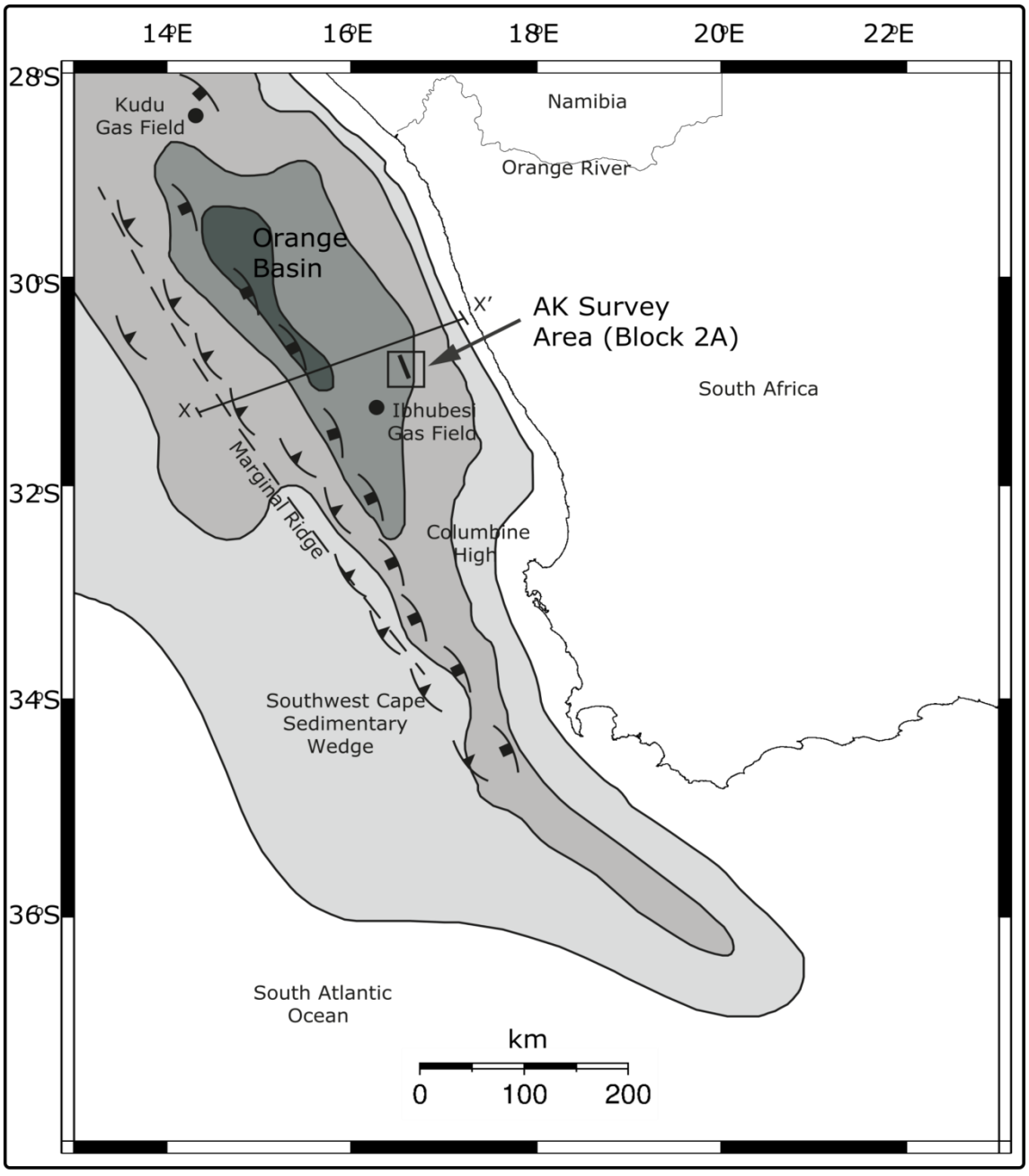



Figure 5.1: Map of the offshore southern Africa, showing the Orange Basin and the AK survey area of Block 2A in the Ibhubesi gas field (modified after Jungslager, 1999)

The seismic dataset was processed using the common procedures in marine seismic data processing. Gain, multiple suppressions (using the Radon Transform), normal move-out (NMO), dip move-out (DMO) and migration were applied to the data before stacking. The DMO, which was based on Kirchhoff migration, was conducted on 20 different offset groupings at a maximum dip of 40 ms/trace. This was followed by a finite difference migration, with migration frequencies of 6 to 70 Hz at a maximum dip of 60 degrees. Post-stack filtering, using FXY deconvolution, and 2000 ms AGC were also applied to the final stacked volume to further improve the quality of the datasets. Detailed processing of the 3D seismic data has already been presented in Chapter 4.

### 5.3.2 Methodology

The interpretation of the 3D seismic reflection cube was carried out using the 3D volume rendering technique. The principle of 3D volume rendering is based on defining transfer functions that will assign colour and opacity to each voxel value along a viewing direction. The contributions of each voxel value are then summed together along the direction of the virtual viewing ray to form the final image (Levoy, 1990; Meissner et al., 1999; Silva et al., 2003; Laurent et al., 2005). The volume rendering integral along this direction is given by Laurent et al. (2005) as:

$$I = \int_0^D c\big(x(\lambda)\big).\ exp\left(-\int_0^\lambda \zeta\big(x(\lambda)\big)d\lambda\right)d\lambda \qquad (5.1)$$

where I is the pixel's final colour intensity, D is the distance to the point where the viewing ray leaves the data set, λ is the wavelength of the viewing ray, and c(x)

and $\zeta(x)$ define the colour and extinction coefficients for any point x in space, respectively.

To carry out the volume rendering, a time interval of the slab containing the seismic image of interest is first identified and isolated from the seismic volume. This is then followed by the manipulation of the amplitudes within the slab by suppressing a range of positive and negative amplitudes below a specified threshold value. The regions corresponding to the suppressed amplitude range are rendered transparent, thereby enhancing depositional and structural features that are present within the slab.

## 5.4 Results and discussion

Definitive recognition of impact structures requires several criteria besides crater morphology, such as melt rocks, breccia, pseudotachylyte, and proven evidence that the structure was formed by shock metamorphism, such as presence of shatter cones, planar deformation features, coesite and stishovite (Chao, 1968; Dietz, 1968; Melosh, 1982). Other features that may also serve as important confirmation of impact craters includes presence of ejecta that are formed as a result of the excavation of sea bed by the impactor (Melosh, 1982; Ormö and Lindström, 2000), and presence of suevite and spherules (Grieve and Pilkington, 1996; Dypvik and Jansa, 2003).

Some of these criteria are common in terrestrial impact structures, and are easily investigated because of the accessibility of impact craters that are formed on land. However, the same cannot be said for craters in the marine environment, due to

their buried and eroded nature, as well as occasional absence of impact melt sheets (Grieve and Pilkington, 1996; Ormö and Lindström, 2000). The definitive confirmation, therefore, of most buried or marine impact craters depends on the analysis of core samples obtained from boreholes that penetrated the region where these craters occur.

It is often difficult to confirm possible impact craters discovered through geophysical methods (e.g., Cooper et al., 2010) due to the cost of drilling. However, where core or rock samples are not available, geometrical criteria derived from 3D seismic images such as crater shape (typical depth-to-diameter ratio), crater diameter, crater form, presence of central peak, and overturned peripheral strata may provide an alternative framework for identifying impact structures (Stewart, 1999; 2003).

The identification of impact craters buried within marine sedimentary sequence can be very challenging, owing to their morphological resemblance to other circular geological structures, such as diapirs, pockmarks and collapsed features that are common within the marine environment. However, these other circular structures are formed through the upward rise of fluids (e.g. gas) or viscous materials (usually mud or salt), and are usually associated with gas leakage features (such as gas chimneys), or salt-withdrawal synclinal structures that are expressed as chaotic reflections on seismic sections (e.g., Stewart, 2003)

A crater of about 7 km wide occurring within the post-rift sediments in the study area shows some differences from the seismic signatures of these other circular features mentioned above. The crater is buried below 550 ms (~ 700 m) thickness

of sediments, and occurs as a circular structure on a time-slice (Fig. 5.2). A careful analysis of the cross-sections across this circular structure shows no feeder channels (such as faults or gas chimneys) below it (Fig. 5.3). Hence, we believe that is best explained by an impact origin for the crater.

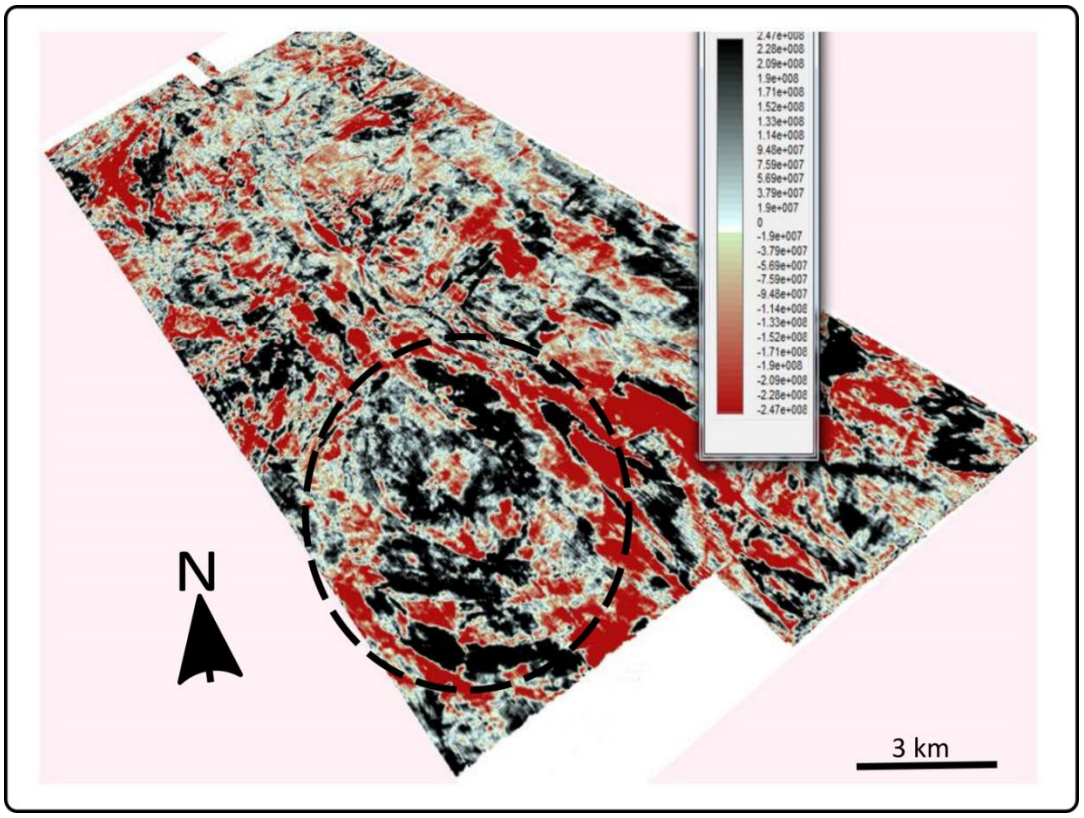



Figure 5.2: A time-slice at 550 ms showing the buried crater in the circled region

The crater appears on vertical section as a feature with concentric downward dipping coherent reflectors at the top, which grade into a zone of highly fractured, incoherent reflectors at the base (Fig. 5.3a). On a pseudo-relief section, the crater resembles a bowl (Fig. 5.3b), with the post-impact zone reflecting as a high relief zone, while the disturbed zone exhibits low relief. The crater measures about 5 km in diameter (measured from the outer rim) and has an elongated length of about 7

km, which suggests the impact probably occurred at a very low angle (e.g., Stewart, 1999). The base of the crater in cross-section (Fig. 5.3a) is observed to be characterized by stratigraphic uplifts, common to impact craters exceeding 4 km in diameter (e.g., Melosh, 1989; Ormö and Lindström, 2000).

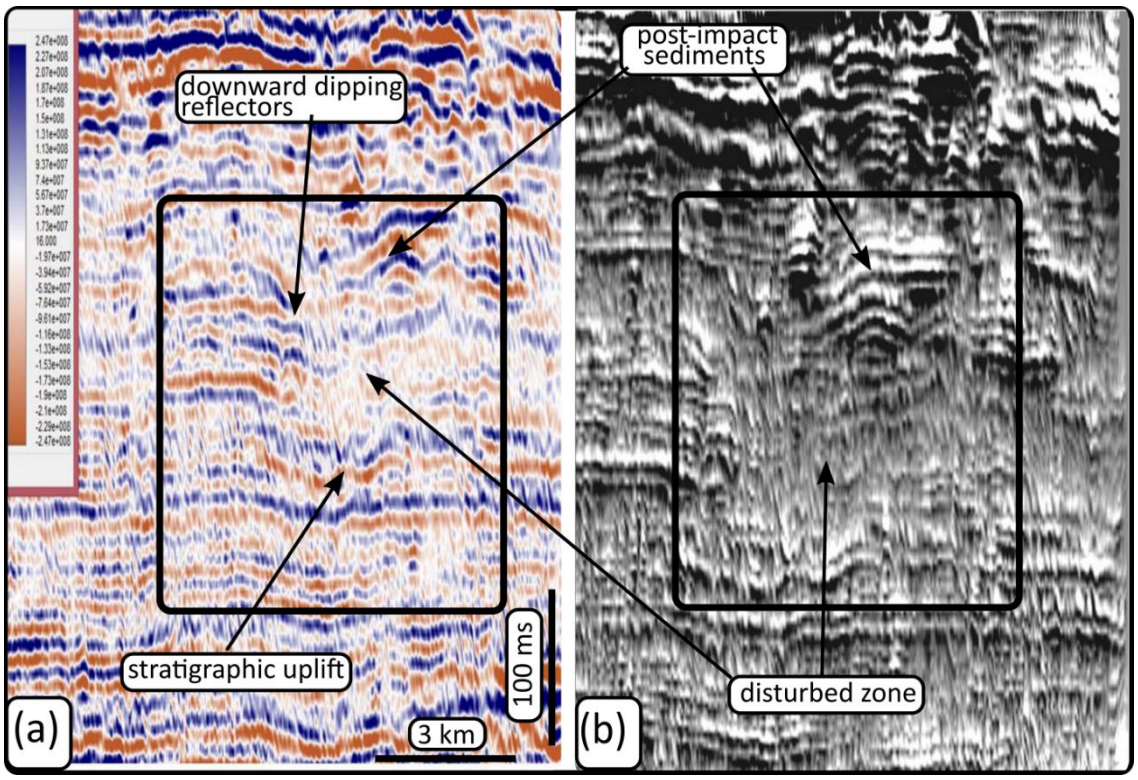



Figure 5.3: Cross-section across the crater with possible deformational features. (a) Amplitude section. (b) Shaded relief section with the crater appearing as low relief zone.

In 3D volume, rendered at an opacity range of 60-80%, more details of the crater's morphology and associated structural features can be seen. The crater exhibits similar morphological characteristics to complex impact craters (e.g., Melosh, 1989; Grieve and Pilkington, 1996), with a circular, elongated outline, a central peak (probably caused by central uplift and subsequent post-impact sediment infilled), and an elevated outer rim, probably due to overturned beds

(Fig. 5.4). Gravity or listric faults were also observed to have developed around the annular rim to the south of the crater.

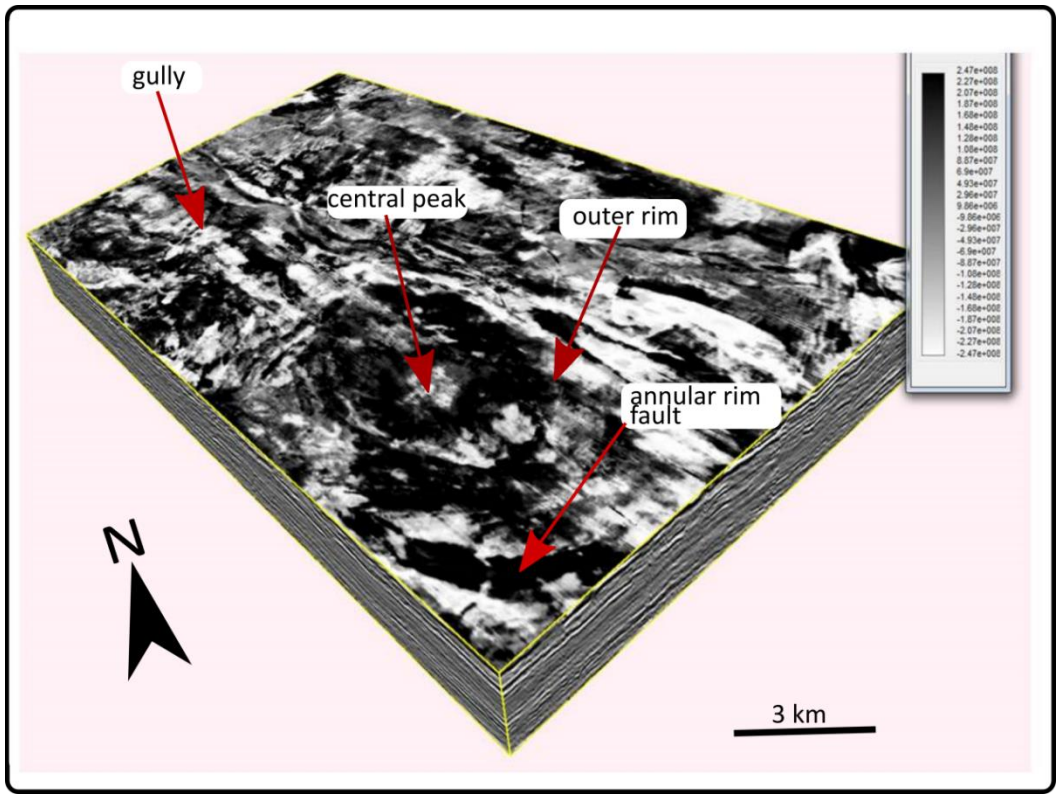



Figure 5.4: Volume rendering at 60-80% opacity showing the detailed geometry of the crater and the associated structures.

The development of radial gullies as a result of the resurge of water the craters after impact has been reported to be common in marine impact cratering processes (e.g., Therriault and Lindstrom, 1995; Lindström et al., 1996; Sturkell, 1998; Ormö and Lindström, 2000; Dalwigk and Ormö, 2001; Ormö and Miyamoto, 2002; Dypvik and Jansa, 2003; Ormö et al., 2002). An approximate 400 m wide N-S trending linear depression is observed to transect the outer rim of the crater (Fig. 5.4), which might have developed from the resurge of water after the impact.

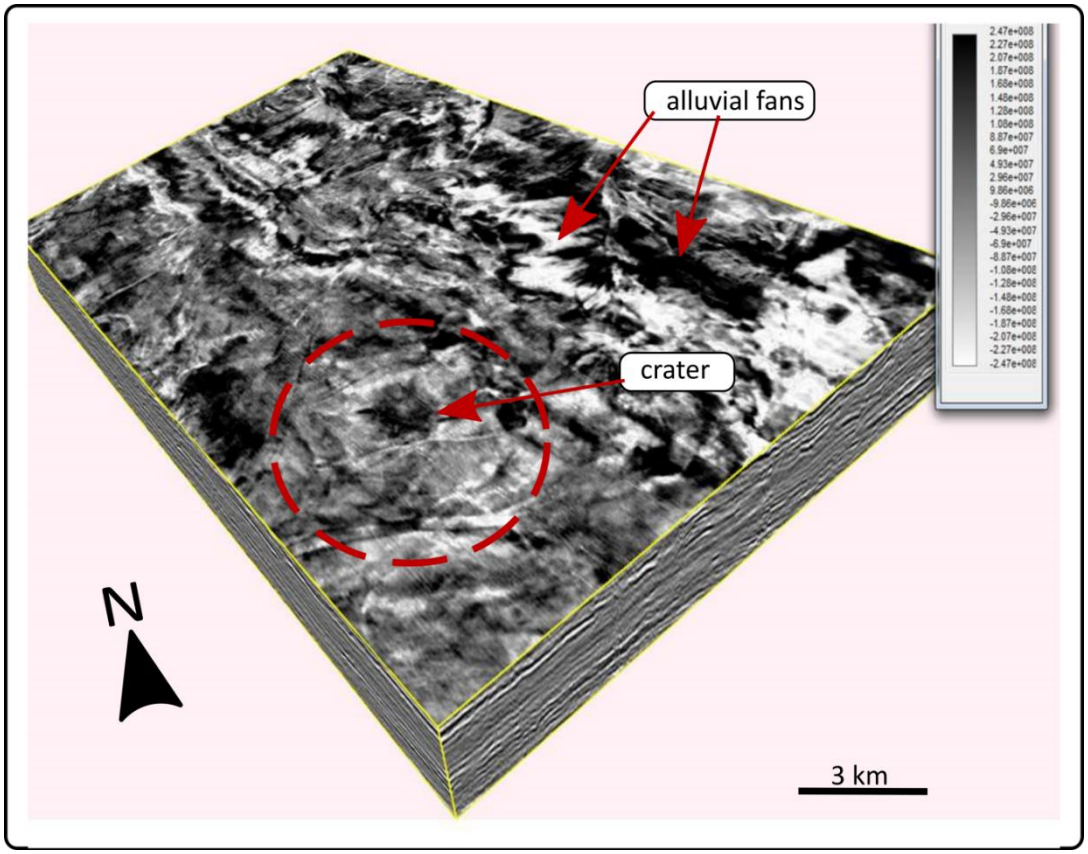



Figure 5.5: Volume rendering at 60-80% opacity showing the crater with the associated sub-marine alluvial fans, which probably suggests its quick burial and eventual preservation.

The estimated true depth of the crater is about 350 ms (~ 440 m), giving it an aspect ratio of approximately 0.09, which falls within the aspect ratio of 0.05-0.3 for common impact craters (e.g., Melosh, 1989; Stewart, 2003). The association of the crater with sub-marine alluvial depositional fans (Fig. 5.5) suggests a possible impact that occurred in a shallow marine, deltaic environment, where the rapid deposition of sediments within this environment probably led to its preservation.

## 5.5 Conclusions

Volume rendering provides a quick way of looking at the depositional and structural features within a 3D seismic volume through amplitude manipulation. In this study, volume rendering has assisted in providing the detailed description of the geometry of the crater observed on the time slice. Since there are many geological features that can give rise to a feature with a circular geometry on a time slice, we have restricted our comparison to key features that distinguish impact structures from other circular geological structures. These key morphological features include the absence or presence of feeder channels below the structure, the aspect ratio, the presence of a central rim, associated annular rim faults, stratigraphic uplift, as well as the presence of gully that may indicate the possible resurge of water back into the crater after impact.

However, it is important to mention that the ultimate confirmation of the structure is subject to the availability of core samples from the vicinity of the suspected impact structure. This will further assist in constraining the timing of the event and origin of the structure, through revelation of deformational features (if present) that are associated with impact cratering. Finally, the interpretation of this enigmatic circular structure, using 3D volume rendering technique, has revealed the detailed morphology of the features of the structures to be similar to that of complex impact craters. These features include the presence of a central peak, stratigraphic uplifts, as well as annular rim faults. The presence of gully erosion, common to most marine impact craters, was also observed around the crater, suggesting a resurge of water back into the crater after the impact.

## References


Brown, Jr., L.F., Benson, J.M., Brink, G.J., Doherty, S., Jollands, A., Jungslager, E.H., Keenen, A., Muntingh, A., and van Wyk, N.J.S. 1995. Sequence stratigraphy in offshore South African divergent basins. An atlas on exploration for Cretaceous lowstand traps by Soekor (Pty) Ltd, *American Association of Petroleum Geologists*, Studies in Geology, **41**, 184pp.

Chao, E.C.T., 1968. Pressure and temperature histories of impact metamorphosed rocks - based on petrographic observations, in: French, B.M. and Short, N.M. (editors), Shock metamorphism of natural materials. *Mono Book Corp*., Baltimore, 135-158.

Cooper G.R.J., Webb, S.J., Gibson, R.L., and Martinez, I., 2010. A possible new impact structure in the Okavango Delta, Botswana, *in* Gibson, R.L., and Reimold, W.U., (eds)., Large Meteorite Impacts and Planetary Evolution IV, *Geological Society of America Special Paper* **465**, 191-199, doi: 10.1130/2010.2465(13).

Dalwigk, I. von and Ormö, J., 2001. Formation of resurge gullies at impacts at sea: The Lockne crater, Sweden, *Meteoritics and Planetary Science,* **36**, 359-369.

Dietz, R.S., 1968. Shatter cones in cryptoexplosion structures, in: French, B.M.and Short, N.M. (eds), Shock metamorphism of natural materials, Mono Book Corp., *Baltimore*, 267-285.

Dypvik, H. and Jansa, L.F., 2003. Sedimentary signatures and processes during marine bolide impacts: A review, *Sedimentary Geology*, **161**, 309–337.

Gerald, D.K., 2014. Fundamentals of 3D seismic volume imaging, Extended Abstract, *American Association of Petroleum Geologists*, Hedberg Research Conference, Houston, Texas.

Gerhardt, A., Machado, M., Silva, P.M., and Gattass, M., 2001. Two-dimensional opacity functions for improved volume rendering of seismic data: 7th International Congress of the Brazilian Geophysical Society, Savador, Brazil.

Gerrard, T. and Smith, G.C., 1982. Post-Palaeozoic succession and structure of the south-western African continental margin, in: J.S. Watkins and C.L. Drake (eds.). Studies in Continental Margin Geology, *American Association of Petroleum Geologists Memoir*, **34**, 49-74.

Gradstein, F., Ogg, J. and Smith, J., 2004. A Geologic Time Scale, Cambridge University Press, United Kingdom, 589 pp.

Granado, P., 2006, Tectonostratigraphic evolution of the Orange Basin, SW Africa, Unpublished M.Sc. Thesis, University of London, 120 pp.

Grieve, R.A.F. and Pilkington, M., 1996. The signature of terrestrial impacts, *Journal of Australian Geology and Geophysics*, **16**, 399-420.

Hauser, H., Mroz, L., Bischi, G.I. and Groller, M.E., 2001. Two level volume rendering: *IEEE Transactions on Visualization and Computer Graphics*, **7**, 242-252.

Huw, J., 2009. Visualizing 3D features in 3D seismic data, *First Break*, EAGE, **27**, 57-62.

Jungslager, E. H. A., 1999. Petroleum habitats of the Atlantic margin of South Africa, in: Cameron, N. R., Bate, R. H., and Clure, V. S., (eds.), The Oil and Gas Habitats of the South Atlantic, *Geological Society London Special Publications*, **153**, 153-168.

Kuhlmann, G., Adams, S., Campher, C., van der Spuy, D., di Primio, R. and Horsfield, B., 2010. Passive margin evolution and its controls on natural gas leakage in the southern Orange Basin, blocks 3/4, offshore South Africa, *Marine and Petroleum Geology*, **27**, 973–992.

Lacroute P. and Levoy, M., 1995. Fast volume rendering using a shear warp factorization of the viewing transform, *Computer Graphics*, **28**, 451-458.

Laurent, C., Bosquet, F. and Levy, B., 2005. Advances in seismic interpretation using new volume visualization techniques: *First Break*, **23**, 69-72.

Levoy M., 1990. Efficient ray tracing of volume data, *ACM Transactions on Graphics*, **9**, 245-261

Lindström, M., Sturkell, E.F.F., Ormo, J. and Tornberg, R., 1996. The Lockne marine impact in the Ordovician of central Sweden, *Meteoritic and Planetary Science*, **31**, A80.

Meissner M., Hoffman, U. and Strasser, W., 1999. Enabling classification and shading for 3D texture mapping based volume rendering using OpenGL and Extensions. *IEEE Visualization*, 207-214.

Melosh, H.J. 1982. The mechanics of large meteoroid impacts in the Earth's oceans: In Geological implications of impacts of large asteroids and comets on the Earth, edited by Silver L. T. and Schultz P. H. (eds.), *Geological Society of America Special Paper* **190**, 121-127.

Melosh, H.J., 1989, Impact cratering: A geologic process, New York, Oxford University Press, 245 p.

Ormö, J. and Lindström, M., 2000. When a cosmic impact strikes the sea bed, *Geological Magazine*, **137** (1), 67–80, doi: 10.1017/S0016756800003538.

Ormö, J. and Miyamoto, H., 2002. Computer modelling of the water resurge at a marine impact: The Lockne crater, Sweden, *Deep-Sea Research* II, **49**, 983–994.

Ormö, J., Shuvalov, V. V. and Lindström, M., 2002. Numerical modeling for target water depth estimation of marine-target impact craters, *Journal of Geophysical Research*, **107**, 31-39.

Paton, D.A., di Primio, R., Kuhlmann, G., van der Spuy, D. and Horsfield, B., 2007. Insights into the petroleum system evolution of the southern Orange Basin, South Africa, *South African Journal of Geology*, **110**, 261-274.

Paul, S.C., Brian, S.K., David, G.H., Jenifer, C.C. and Elliot, K.F., 1999. Three-dimensional volume rendering of Spiral CT Data: Theory and Method, *RadioGraphics*, **19**, 745-764.

Raskar, R. and Cohen, M., 1999. Image Precision Silhouette Edges: ACM Symposium on Interactive 3D Graphics, 135-140.

Silva, P.M., Machado, M. and Gattass, M., 2003. 3D Seismic volume rendering, Eighth International Congress of The Brazilian Geophysical Society, Rio de Janeiro, Brazil.

Stewart, S.A., 1999. Seismic interpretation of circular geological structures, *Petroleum Geoscience*, **5**, 273–285.

Stewart, S.A., 2003. How we will recognize buried impact craters in terrestrial sedimentary basins? *Geology*, **31**, 929-932

Sturkell, E.F.F., 1998, Resurge morphology of the marine Lockne impact crater, Jamtland, central Sweden, *Geology Magazine*, **135**, 121–127.

Therriault, A.M. and Lindström, M., 1995. Planar deformation features in quartz grains from the resurge deposit of the Lockne structure, Sweden, *Meteoritics and Planetary Science*, **30**, 700-703.

Tinker, J., de Wit, M. and Brown, R., 2008. Linking source and sink: evaluating the balance between onshore erosion and offshore sediment accumulation since Gondwana break-up, South Africa, *Tectonophysics*, **455**, 94–103.

Weigelt, E. and Unzelmann-Neben, G., 2004. Sediment deposits in the Cape Basin: Indications for shifting ocean currents? *American Association of Petroleum Geologists Bulletin*, **88**, 765–780.

Worrel, A., 2001. Rapid and accurate 3D fault interpretation, using opacity and optical stacking to reveal geologic discontinuities, *The Leading Edge*, **20**, 1381-1385.

Yilmaz, O. Z., 2001, Seismic data analysis, *Society of Exploration Geophysicists*, Tulsa, OK.

# Chapter 6

# General Conclusions and Recommendations

## 6.1 High-resolution Seismic Reflection Investigation of Subsidence and Sinkholes at Abandoned Coal Mine Sites in South Africa (Chapter 3)

### 6.1.1 Summary

The occurrence of coal-mining-related near-surface subsidence and sinkholes at two coal mine sites located in Benoni area, near Johannesburg, and the Springlake mine in the town of Dundee was investigated using the high-resolution seismic reflection method. The results of the investigation have shown that:

- Near-surface subsidence due to the collapse of the overburden rocks into underlying subsurface voids or cavities occurs in the two study areas.
- The near-surface subsidence and sinkhole features commonly observed in the Benoni area is caused by the collapse of the overburden rocks into voids caused by coal-mining and dissolution cavities within the underlying dolomite.
- The suspected dolerite intrusion in the Benoni area exhibits complex geometry, having the characteristic of a sill and a dyke and could reach up to about 13 m in thickness.
- The near-surface subsidence at the Springlake mine is due to the failure of the supporting pillars.
- The mined-out zone was confirmed by the investigation to have extended beyond the area indicated in the Springlake Colliery mine plan.

- The 100 and the 48 Hz geophone types both have similar resolution as compared along the same profile and were able to resolve the dolerite layer that occurs below the profile.

### 6.1.2 Recommendations for future investigations

Based on the findings from this study, the followings are recommended for future infrastructural development and investigations of near-surface subsidence and sinkholes in the study areas using the high-resolution seismic reflection method.

1. In the Benoni area, it is recommended that the undermined area in the south of the study area is avoided for any future infrastructural development due to the vulnerability of this area to subsidence and sinkhole development. Instead, the northern part of the study area should be considered for future development because of its lower vulnerability to the development of subsidence and sinkholes due to the existence of a competent doleritic layer of about 13 m in thickness.
2. The investigation conducted at the Springlake Colliery mine also confirmed evidence of subsidence in the suspected mined-out zones; it is therefore recommended that this area is avoided for any future infrastructural development within the mine.
3. It is recommended that a high-resolution 3D reflection seismic is conducted in the two study areas, in order to adequately delineate the mined-out zones and accurately mapped the geometry of the dolerite layer.

## 6.2 3D Seismic Analysis of the AK Fault, Orange Basin: Implications for Hydrocarbon Leakage Assessment and Offshore Neotectonics (Chapter 4)

### 6.2.1 Summary

A detailed analysis of a half-graben bounding fault located within the exploration Block 2A, in the Ibhubesi gas field of the Orange Basin, was conducted using the high-resolution 3D seismic reflection datasets. The interpretation of the fault involved the combination of conventional 3D seismic interpretation and the use of seismic attributes. The role played by this fault in promoting the vertical migration of fluids in the Orange Basin, and the neotectonic activities along the fault were also investigated. The result of the analysis shows that:

- The AK Fault generally dips landwards in a NE direction and shows two strike direction that are obliquely oriented to each other.
- The fault was reactivated along an oblique extensional regime caused by the re-orientation of the regional orthogonal extension direction through approximately 30 degrees.
- The AK Fault has been active since its evolution in Late Jurassic to Early Cretaceous, and has accrued a maximum vertical displacement of approximately 120 m.
- The fault is being reactivated by normal faulting, with minor shear components along fault tips, and an extensional stress regime with the greatest horizontal compressional stress ($S_{Hmax}$) approximately parallel to its strike.

- The fault consists of five seismically detectable segments whose evolution reflects the characteristics of both the isolated and coherent end member models of segmented fault origin.
- The fluid migration along the fault is promoted by dilatational, fault-parallel fractures in the relay zones, which act as conduits for fluid movement.
- Evidence for notectonic activities along the fault include the seismic events that were observed within the vicinity of the fault as well as incipient diapir development along the fault.

These findings agree with the regional stress regime of west coast of South Africa proposed by Bird et al (2006) and De Beer (2012), but differ from those reported by Viola et al (2005) for a similarly oriented fault ~ 200 km to the west.

### 6.2.2 Recommendations for future investigations

The analysis based on this study proves that the AK Fault might still be active. Therefore, further investigation involving seismic hazard assessment around the vicinity of the fault is recommended.

## 6.3 Volume Rendering of 3D Seismic Reflection Data Reveals a Possible Impact Structure in the Orange Basin, Offshore South Africa (Chapter 5)

### 6.3.1 Summary

Seismic interpretation of an enigmatic circular geological anomaly within the Orange Basin was carried out using the 3D volume rendering technique. The

technique provides a quick visualization of 3D seismic reflection data and easy recognition of relief or topographic features that may not be visible on conventional time slice. The interpretation of this enigmatic circular feature using the volume rendering has shown that:

- The structure is approximately 5-7 km wide with an aspect ratio of approximately 0.09.
- The structure has morphological features that are common to complex impact craters, which include the presence of a central peak, an elevated outer rim, annular rim faults and stratigraphic uplift.
- The crater is transected by an approximately 400 m wide gully that suggests the resurge of water back into the crater after impact.
- The crater is buried within a shallow marine, deltaic environment below approximately 700 m thickness of sediment.

This enigmatic structure is suspected to be a possible impact crater. However, the ultimate confirmation is subject to the availability of core samples from around the vicinity of the structure that may provide evidence for impact catering.

### 6.3.2 Recommendations for future investigations

Further analysis of core samples from the boreholes within the vicinity of the structure is recommended, in order to search for conformational features, such as ejecta, that may provide evidence for impact cratering.

# Reference

Bird, P., Ben-Avraham, Z., Schubert, G., Andreoli, M., and Viola, G., 2006. Patterns of stress and strain in southern Africa, *Journal of Geophysical Research*, **111**, B08402, doi:10.1029/2005JB003882.

De Beer, C. H., 2012. Evidence of Neogene to Quaternary faulting and seismogenic deformation along the Namaqualand coast, South Africa, *South African Journal of Geology*, **115**, 117-136.

Viola, G., Andreoli, M., Ben-Avraham, Z., Stengel, I., and Reshef, M., 2005. Offshore mud volcanoes and onland faulting in southwestern Africa: neotectonic implications and constraints on the regional stress field, *Earth and Planetry Science Letters*, **231**, 147-160.

# APPENDIX